Passive and active cooling of cavity optomechanical torque sensors for magnetometry applications

by

Paul Ho-Choong Kim

A thesis submitted in partial fulfillment of the requirements for the degree of

Doctor of Philosophy

Department of Physics

University of Alberta

Abstract

Cavity optomechanics, the study of mechanical effects from resonant light, has recently shown remarkable sensitivities in displacements and forces (torques) — which opened up new avenues for scientific and technological developments. One of the interesting prospects of cavity optomechanics includes torque magnetometry, where mesoscopic effects of magnetism can be explored through sensitive nanomechanical detection. In this thesis, I drastically improved the sensitivity of optomechanical torque sensors for magnetometry applications. Hence, this work is divided into three phases: my achievement in approaching quantum-limited torque sensitivities at millikelvin temperatures, my recent work on mechanical mode-damping using ferromagnetic needles at room temperature, and my current progress on implementing torque-mixing magnetic resonance spectroscopy to optomechanics where spin modes of a permalloy disk are studied.

I begin the discussion by briefly introducing the field of cavity optomechanics, where I have combined cavity optomechanics and torsional mechanics for the first time with a thermally-resolved torque sensitivity of 0.8 zNm/$\sqrt{\text{Hz}}$. Then, I have optimized the on-chip design and improved nanofabrication techniques such that 0.5 zNm/$\sqrt{\text{Hz}}$ was reached. The "pluto" device, with a large optomechanical coupling, was placed in our unique dilution refrigerator to minimize the thermal noise at 25 mK. Looking through a cryogenic compatible microscope objective, a versatile dimpled microfibre can access any optical microdisk. Arriving at the optimized device, thermalized at the dilution stage, the torque sensitivity was 2.9 yNm/$\sqrt{\text{Hz}}$, just eleven times above the standard quantum limit.

Although the torque sensitivity alone is impressive, compatibility to magnetic systems needs to be verified, where I incorporated magnetic materials to demonstrate its adaptability to optomechanics. Here, I have tested both hard and soft magnets, namely iron needle and permalloy disk. Utilizing a device with 0.6 zNm/$\sqrt{\text{Hz}}$ sensitivity at room temperature, I have successfully driven torque using out-of-plane alternating magnetic fields, where I extracted bulk remanence of iron. I have also shown feedback cooling as well — highlighting mode-damping below 12 K.

I review my final experiment to implement torque-mixing magnetic resonance spectroscopy to study spin modes of a $\sim$1 μm diameter permalloy disk. Adding the in-plane magnetic fields to the previous experiment, I was able to detect spin modes and vortex pinning, which results in a high frequency shift ($>$ 1 GHz). This has one important consequence, where we can apply magneto-opto-mechanical coupling to convert microwave to telecom photons coherently. In summary, my project conveys that optomechanics and torque-mixing magnetic resonance spectroscopy are compliant, which may yield great results when equipped with cryogenic torque sensitivity. Ultimately, this platform of cryogenic optomechanical torque sensor can be a great candidate to study other exotic magnetic materials, to uncover unexplored physics in vortex-mechanics, phases of matter, and other mesoscopic properties of superconductivity.

Preface

The purpose of the present study was two-fold: to examine the impact of cavity optomechanics on torque sensors and to explore nano-magnetism through torque magnetometry. Torque magnetometry is a powerful method for studying intricate properties of magnetic materials. I am grateful to partake this exciting project, which stemmed from my supervisor's post-doctorate work from the Freeman group. I have gained valuable experiences working in collaboration with the Freeman group. It is truly a blessing to work on merging the best of two fields: optomechanics and nanomagnetism. At the end chapter of my master's thesis, I stated that we were building an optomechanical apparatus in a dilution refrigerator for the sole purpose of maximizing the torque sensitivity. Being fortunate to stay in the group and carry out this project through my Ph.D. studies, I have exactly done so by building our one-of-a-kind optomechanical dilution refrigerator apparatus. Initially I assisted Allison MacDonald in constructing this apparatus to mount tapered fibres and silica bottles, which resulted in two publications entitled "Optical microscope and tapered fiber coupling apparatus for a dilution refrigerator" in *Review Science Instruments,* 86, 013107, 2015 and "Optomechanics and thermometry of cryogenic silica microresonators" in *Physics Review A* 93, 013836, 2016.

After these experiments, I have taken full charge of the dilution refrigerator to modify and incorporate on-chip torque sensors — where I have machined various pieces to accommodate a dimpled microfibre and a device chip. As a result, I was able to cool the torque sensor down to 25 mK, which yielded remarkable torque sensitivity of 2.9 yNm/$\sqrt{\text{Hz}}$. This result was published with Bradley Hauer, as my co-author, who contributed most of the analytical

discussion, in *Nature Communications*, 7, 13165, 2016 entitled "Approaching the standard quantum limit of mechanical torque sensing". As the first author of this paper, I have taken full responsibility of optimizing cleanroom processes to create these intricate devices in place of commercial foundries. With the capability of optical microscope inside the fridge, I was able to characterize and analyze all the data and achieve torque sensitivity near the standard quantum limit. Contents of this thesis were taken from my published works.

After my lengthy usage of the dilution refrigerator, I was also instrumental in the next fridge project, lead by Bradley Hauer, for fabricating a new design of optomechanical coupling devices for studying the two-level systems in ordered-silicon in "Two-Level system damping in a quasi-one-dimensional optomechanical resonator," *Physics Review B* 98, 214303 (2018) and investigating photothermal effect in "Dueling dynamical backaction in a cryogenic optomechanical cavity," *accepted to Physical Review A* (2019). During this time when the fridge was occupied, I applied my optomechanical torque sensor to study hard and soft magnetic systems. With the aid of magnetic simulations by Fatemeh Fani Sani, I was able fabricate the chip, construct the apparatus, take the measurements, and analyze the data. We submitted two papers: the first paper was published, "Magnetic actuation and feedback cooling of a cavity optomechanical torque sensor," *Nature Communications* 8, 1355 (2017), for driving and damping the torsional mode using magnetic forces, and the second paper was published, "Broadband optomechanical transduction of nanomagnetic spin modes", *Applied Physics Letters* 113, 083104 (2018), for implementing torque-mixing magnetic resonance spectroscopy to cavity optomechanical systems for the first time.

I was active in my role as a cleanroom specialist in the group where I helped out other projects in regards to superfluid cavities. These devices were made from a quartz wafer, and I assisted in the fabrication process — which lead to a publication, "Ultralow-Dissipation superfluid micromechanical Resonator," *Physics Review Applied,* 7, 044008, 2017. Here, as a summary of my Ph.D. work, I have organized this thesis to provide some background of optomechanics and torque magnetometry (Chapter 2); explain experimental details of

nanofabrication techniques and the operations of a dilution refrigerator (Chapter 3); highlight torque sensitivities near the standard quantum limit (Chapter 4); demonstrate feedback cooling and magnetic actuation using a ferromagnetic needle (Chapter 5); and confirm the adaptability of torque-mixing magnetic resonance spectroscopy in cavity optomechanics (Chapter 6). Chapter 7 includes final thoughts and outlook on future projects with mesoscopic superconductivity and optomechanical torque-sensing platforms.

To my eternal companion,
Thank you Starlayne for your love and support.

Acknowledgements

I would like to take this opportunity to thank everyone who helped me during my twelve years of physics journey. It all started back at Grant MacEwan university, college at the time, with Dr. Evan Hackett. He taught the courses with energy, passion, and humour, where I began to understand and mesmerize the wonders of physics — which still continues to date. My decision to study physics while transferring to the university of Alberta was one of my best choices, where I had a lot of great instructors during my undergraduate studies. Special thanks to professor Frank Hegmann, who taught my favourite subjects in condensed matter physics and optics, where it was truly a feast to my mind.

In addition to the wonderful courses offered, my greatest gratitude goes to my supervisor professor John Davis. My associations with him during my undergraduate research project, MSc thesis, and Ph.D. project were excellent and I cannot thank him enough. I feel fortunate to have the honour of being in the lab's early roster. Knowing him for eight years, he has traits of a great advisor: strong managerial skills, inspiring vision, and unwaivering work principles. To my mind, he is one of the greatest experimentalists and I have no doubt that his lab will continue to flourish under his leadership. I would like to also thank the Quanta CREATE program, organized by my supervisor, which illuminated career paths outside the academic path of entrepreneurship and industry. I would also like to add my thanks to my supervisory committee for thoughtful comments and insights during the meetings.

My accomplishments during the graduate studies would not have been possible without my awesome team. The synergy and coherent vision amongst my colleagues were established early in our lab. I would like to first thank my optomechanics crew, namely Bradley Hauer, Callum Doolin, Allison MacDonald, and Hugh Ramp. Their strong work ethic, openness to new ideas, and positive attitude in the face of challenges have taught me greatly. I will remember Brad for his immense intellect and constructive skepticism; Callum for his thinking-outside-the-box mindset and problem solving skills; Allison MacDonald for her positive attitude and deep knowledge; and Hugh Ramp for his fountains of questions and

always being approachable. Despite the different projects we had in optomechanics, we all constructively worked together to maximize our productivity. Countless thanks goes to my other colleagues and friends, Tushar Biswas, Fabien Souris, Xavier Rojas, Tommy Clark, Fatemeh Fani Sani, Clinton Potts, Ruhul Amin, Junko Taniguchi, Kyle Reid, Joe Losby, and Yikai Yang. I cherish all the countless moments together during the experiments, group meetings, and conferences.

I acknowledge the Nanofab staff, who helped me patiently during numerous nanofabrication trainings and inquiries. Thank you Greg Popowich and James Chaulk for being the best technical staff. Thank you Clotilde for reminding me of Quanta events, and being so prompt to order materials and equipments. I also feel blessed to be part of a great company at Norcada for my next journey. I look forward to associate with the great minds in the nanofabrication business.

Lastly, I would like to thank my family. My dear wife, Starlayne, thank you for your positive attitude and encouragement during my struggles and darkest nights. It was not an easy path for me and I would not have done it without you. Thank you for your endless love, positive encouragement, and constant support during my studies. Hannah, Paul-Anthony, Malena, and Avery, I love you all. Thank you for loving me despite the long hours spent in the lab.

As a non-native speaker in English, one thing that I struggled the most was my writing. Thank you readers for being patient enough to read this through. I have invested long hours and hard work during my studies. I hope my work can be of use in anyway possible.

Contents

List of Tables

List of Figures

Nomenclature

Acronyms

BOE Buffered oxide etch . . . 26

CMOS Complimentary metal-oxide-semiconductor . . . 25

CPD Critical-point drier . . . 26

EBL Electron-beam lithography . . . 22

FEM Finite element method . . . 10

FPC Fibre polarization controller . . . 40

FWHM Full-width-half-maximum . . . 13

HiM Helium ion microscope . . . 29

HSQ Hydrogen silsesquioxane . . . 29

ICP-RIE Inductively coupled plasma reactive-ion etch . . . 33

IPA Isopropyl alcohol . . . 37

LIGO Laser interferometer gravitational-wave observatory . . . 14

MEMS Micro-electro-mechanical systems . . . 25

MRFM Magnetic resoanance force microscopy . . . 4

NMP N-Methyl-2-pyrrolidone . . . 68

NOMS Nanooptomechanical systems . . . 2

OBC Optomechanical back-action cooling . . . 55

OFHC Oxygen free high-purity copper . . . 71

PCB Printed-circuit-board . . . 88

PD Photodiode . . . 97

PECVD Plasma-enhanced chemical vapour deposition . . . 130

PID Proportional-integral-derivative . . . 74

PMMA Polymethylmethacrylate . . . 26

PSD Power spectral density . . . 12

Py Permalloy . . . 5

PZT Lead zirconate titanate . . . 130

RF Radio-frequency . . . 20

RIE Reactive-ion etch . . . 33

SEM Scanning electron microscope (micrograph) . . . 30

SOI Silicon-on-insulator . . . 1

SQL Standard quantum limit . . . 15

TMP Turbo-molecular pump . . . 71

TMRS Torque-mixing magnetic resonance spectroscopy . . . 5

UHF Ultra-high frequency . . . 97

UHV Ultra-high-vacuum . . . 97

VCVOA Voltage-controlled variable optical attenuator . . . 75

VHF Vapour hydrofluoric acid . . . 25

WGM Whispering-gallery-mode . . . 7

DI H_2O Deionized water . . . 63

Symbols

α Conversion factor from voltage to angular displacements . . . 12

$\bar{n}_{\mathrm{min}}$ Minimum attainable average phonon occupancy . . . 56

$\chi(\Omega)$ Generalized susceptibility . . . 12

χ_0, χ_m Relative and magnetic susceptibility . . . 19

$\dot{\theta}_n$ Measurement noise . . . 18

$\dot{N}$ ^{3}He circulation rate . . . 47

$\dot{Q}_{\mathrm{mc}}$ Cooling power from the mixing chamber . . . 47

η Optical efficiency . . . 56

Γ Mechanical dissipation rate . . . 11

κ Torsion elastic constant . . . 9

- Chapter 1 -

INTRODUCTION

Nothing happens until something moves.

-Albert Einstein

§ 1.1 Motivation

Nanomechanics, through calibrated measurements of torques and forces, is one of the ubiquitous tool that describes some of the fascinating physics around us. That is, most physical phenomena can be translated into a force or torque that deflect mechanical elements. Through careful measurement of the deflection — properties of light, magnetism, and phases of matter can be extracted [1]-[3]. Hence over the past 50 years, steady and rapid progress have been made to detect increasingly sensitive mechanical resonators for studying fundamental physics and applications [4]-[8]. The challenge, often, is to acquire high sensitivity to displacement while simultaneously miniaturizing the resonators through advanced fabrication techniques [9; 10]. While modern fabrication techniques allow pg to fg-scale mechanical devices on silicon-on-insulator (SOI) chips the sensing sometimes requires complex microelectronic architecture for capacitive measurements [11; 12] or creating a small beam spot size of $\sim$1 μm for interferometric detection [13].

It has been proposed, and exciting recent work has started to reveal, that extremely small strain sensitivities can be obtained through confinement of light inside two macroscopic Fabry-Pérot cavities and observing the interference of the two arms — where gravitational waves were first detected [14; 15]. Applying this principle to smaller on-chip devices, high mechanical sensitivities, with noise floors as low as few fm/$\sqrt{\text{Hz}}$, can be acquired with the use

of various kinds of optical resonators such as microdisks, photonic crystals, and Fabry-Pérot cavities [16]-[18]. A number of groups have quickly adapted on-chip nano-optomechanical systems (NOMS) to a wide range of sensing applications from mass sensors to atomic force microscopes [19; 20]. As measurements of forces and torques are no longer restrained by conventional size-limitations, fundamental studies of nanoscale magnetism, gravity, and quantum mechanics have begun using cavity optomechanics [21]-[25].

I too have grounded my research in the realm of cavity optomechanics to create a platform for torque magnetometry using NOMS. I have successfully built an optomechanical torque sensor with a near quantum-limited torque sensitivity at 25 mK, with torque sensitivities surpassing even optical and magnetic tweezers capable of measuring the torsional properties of single molecules [26]. I have also implemented hybrid systems with iron and permalloy to extract their magnetic properties. Future prospects of mesocopic superconductivity studies and persistent current measurements also seem very interesting inside a dilution refrigerator [27; 28]. Although I did not manage to complete all the experiments that I had hoped for, to detect superconducting vortices using optomechanical torque magnetometry — I am most satisfied that this work may serve as a platform for future meoscopic experiments of magnetism and superconductors at low temperatures. In short, the main objective of this thesis is to convey the influence of on-chip cavity optomechanics to torque magnetometry in terms of sensitivity and material adaptability.

§ 1.2 Developments of torque magnetometry

Magnetic properties of various materials have been an experimental playground for more than a century — still yielding excellent results and progress using torque magnetometry. The underlying principle behind torque magnetometry is the sensitive detection of torsional mechanics due to magnetic torques ($\boldsymbol{\tau}$) by,

$$\boldsymbol{\tau} = \boldsymbol{m} \times \mu_0 \boldsymbol{H}, \tag{1.1}$$

where $\boldsymbol{m}$ is the magentization of the sample, $\boldsymbol{H}$ is the driven magnetic field, and μ_0 is the permeability of free space. A torque is generated when a magnetized sample experiences an applied field as seen in Fig. 1.1a. The mechanical element acts as a harmonic oscillator, with natural frequency Ω_{m} and quality factor Q_{m}. The torque induces an angular deflection of rotation θ, which modulates the reflection in an interferometric scheme, as an example illustrated in Fig. 1.1b [29]. Hence, magnetic properties of the sample can be directly, and non-invasively, measured through torque, where the main objective is to improve the sen-

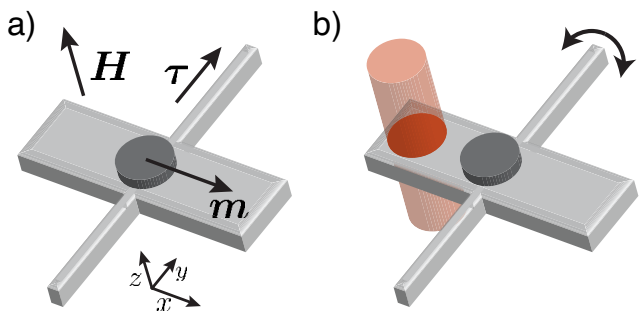

Figure 1.1: **Basic operation of torque magnetometry** (a) A sample of magnetic material (dark grey) is placed on a torsion paddle (light grey). A torque, τ, is applied when the sample is magnetized along x-axis, m, and driven with an out-of-plane H field. (b) The torque then is measured through a focused laser on the torsion paddle. The reflection from the paddle and the substrate creates an interference, where the torsional motion modulates the phase between the two reflected surfaces. The limitation, here, is the beam spot size of the laser, which should be smaller than the paddle, on the order of ~ 1 μm in diameter.

sitivity by means of nanofabrication and improved detection. For the remaining sections in this chapter, I will introduce some applications of magnetic materials in conjunction with modern detection schemes to effectively study these materials with torque magnetometry, even by cavity optomecahnics.

1.2.1 Uses of magnetic materials

Ever since a pointed piece of a mineral called magnetite was identified to turn north and south when supported on the surface of water, people have been drawn into this magnetic phenomena to attain its properties. To date, this phenomena still continues to fascinate us and we have learned how to creatively exploit magnetic properties. Since then, magnetism has become a highly diversified discipline that has opened up new possibilities for scientific and technological developments [30]. Novel magnetic applications emerge, roughly every year, in their scientific advancements. Here, I will list some examples of magnetic materials that I also incorporated in my research: iron, permalloy, and superconductors.

1.2.1.1 Permanent magnets

Permanent magnets remain magnetized despite the withdrawal of magnetizing field. Because of this property of retained magnetization after repeated use, they are widely used in commercial goods, electric generators, and magnetic recording equipments [31]. One distinguishing feature of permanent magnets is in the so-called hysteresis loop, as seen in Fig. 1.2,

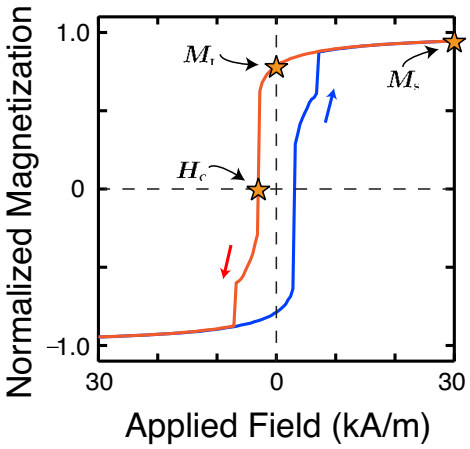

Figure 1.2: **Magnetic hysteresis loop** A simulation of magnetic hysteresis loop is shown for a ferromagnetic material. Remenant magnetization (M_r) is indicated by a star at zero field, coercivity (H_c) is shown where the magnetizaton goes to zero, and saturation magnetization (M_s) is indicated at high field.

where the demagnetization curve reveals the magnetic history of a ferromagnetic material. It is, therefore, useful to characterize quantities such as remanent magnetization (M_r), the magnetization after removal of applied field, and coercivity (H_c), the field necessary to bring magnetization to zero.

Historically, carbon steel magnets were primarily used to make compass needles after the discovery of ancient "magical" lodestone (Fe_3O_4). Steel magnets were soon improved by Co-Pt-Fe alloys, where magnetic recording flourished, given their excellent remanence value and low coercivity [32]. New developments in rare earth metal alloys such as $SmCo_5$, have allowed their use in speakers, electric meters, microwave devices, and linear accelerators, to name a few [33]. In research, they were widely used in nuclear magnetic resonance experiments [34], and magnetic resonance force microscopy (MRFM) [11].

Material	Fe	Co	Ni	Py	Fe_3O_4	$Nd_2Fe_{14}B$
M_s (kA/m)	1710	1440	488	840	480	1280

Table 1.1: Bulk saturation magnetization of some ferromagnetic materials [31].

Hard magnets generally have high remanence and coercivity, which ranges anywhere from 10 kA/m to 1 MA/m subject to its geometry and the quality of the material [35]. For example, a remanent magnetization (M_r) can approach to its saturation magnetization

(M_s), as summarized in Table 1.1, by large shape anisotropy and grain structure. In chapter 5, we will see that a nanoscale iron-needle was used to extract remnant magnetization with excellent agreement to saturation magnetization supported by a simulation shown in Fig. 1.2.

1.2.1.2 Silicon-iron alloys

Silicon-iron alloys are employed in motors, generators, and power transformers. Silicon steel is made by a rigid control of furnace condition to anneal 3∼5% of silicon into steel. These materials possess low coercivity, H_c, or display low hysteresis losses [36]. Improvements in high permeability, or low H_c, were made by making these materials thinner [37]. Since the inclusion of silicon into iron makes the magnet softer, it is possible to study the effects of coercivity as a function of alloy thickness, annealing temperature, and silicon content to improve efficiency.

1.2.1.3 Permalloy

Permalloy (Py), a nickel-iron alloy, has low coercivity and lower remanence being a soft magnet (change in magnetization with small fields). The "traditional" Py, consisting of 20% Fe and 80% Ni, has near-zero magnetostriction (minimal deformities in the process of magnetization) and high corrosion resistance [35]. The compounds of Fe and Ni were varied for improving selective features where $Ni_{45}Fe_{55}$ became the new standard in thin film recording industry [32]. In chapter 6, I use the traditional permalloy $Ni_{80}Fe_{20}$ to access high permeability for torque-mixing magnetic resonance spectroscopy (TMRS) , where I studied spin modes of ∼1 μm diameter Py disk.

1.2.2 Historical examples of torsional mechanics

Measurements of mechanical torques played an important role in both fundamental and experimental physics throughout history. Coulomb and Cavendish, in the 18th century, both used a torsion balance to measure electrostatic force and gravity, respectively [38; 39]. As modern physics flourished in the 20th century, the relationship between magnetism and angular momentum was explored, which lead to the discoveries in 1915 of Barnett and Einstein de-Haas effect, where changes in the magnetization induced mechanical rotation and *vice versa* [40; 41]. The field of magnetism has progressed immensely, where exploring fundamental interactions in magnetism lead to practical applications. For example, giant magnetoresistance effect, which studies nanoscale effects of ferromagnetic multilayers, resulted in wide applications such as hard disks, magnetic memories, and sensors [42; 43].

As current research interests are pushing the limits to make smaller, faster, and more efficient devices — studies of magnetism are now geared toward micrometre and nanometre scale systems [44]. This rapid growth was possible through modern fabrication techniques, measurement schemes, and powerful simulations. As an example, a nanomechanical electrometer was studied using a double torsional oscillator that can be driven and detected using a magnetomotive technique [45]. A small change in the charge alter the magnetomotive force around the loop on the torsion paddle, inducing a change in resonant frequency by the change in effective torsional spring constant. A thermally-limited charge sensitivity, $\sqrt{S_Q} = 0.1\ e/\sqrt{\text{Hz}}$, was achieved above 500 Hz allowing a detection of single electron charge using this device. Another visionary example was the MRFM, where a magnetic tip of a cantilever was scanned across the sample to detect unpaired electron spin in a silicon dioxide sample with spatial resolution of 25 nm [11].

One system in particular, torque magnetometry is especially persuasive for fundamental studies of magnetism in the fact that mechanical resonators can directly measure torque via the net magnetization of individual magnetic elements. Historically torsional oscillators were measured through the naked eye and a ruler, as in the Coulomb and Cavendish experiments, but modern techniques allowed sensitive detection on smaller displacements using lasers (e.g., interferometer) [29]. These microscale sensitive torsional oscillators have opened the door for non-invasive studies of dynamical effects, such as AC susceptibility [46], magnetic resonance [2], and Barkhausen steps in magnetic hysteresis [47].

However, laser interferometry as a readout technique reported torque sensitivities of 10^{-19} $\text{Nm}/\sqrt{\text{Hz}}$ [29]. The low-finesse Fabry-Pérot cavity formed between the nanomechanical resonator and the substrate underneath provide only a weak enhancement. The limitation also occurs from beam spot size, where the mechanical device has to be comparable or larger to the laser focus diameter. In addition, laser drift and heating limits the torque sensitivity. Hence, a migration to a more sensitive readout scheme is essential.

A recent implementation of an integrated optical cavity to localize light to sub-wavelength volume in optomechanical devices has enhanced the coupling between optics (photons) and mechanics (phonons) to exceptional levels [48]. Harnessing this optomechanical interaction has practical advantages over free-space interferometry techniques: first, the size of the resonator is not limited by the beam-spot size of the focused laser, and second the photons in an optical cavity can be made efficient by the use of dimpled microfibres where the interaction of the optical and mechanical componenents can be made large. As a consequence, cavity optomechanics opens up new avenues to explore interesting mesoscopic magnetism [22; 21].

1.2.3 Recent examples of cavity optomechanics and magnetism

The earliest implementation of on-chip cavity optomechanics and magnetism commenced with a magnetometer built with Terfenol-D placed in the middle of a micro-toroid resonator [49]. While the light is confined in a whispering-gallery-mode (WGM), an optical pathlength changes as the magnetostrictive material expands and contracts due to an external field. As a high performance magnetometer, this cavity optomechanical system reported a peak magnetic field sensitivity of 400 nT/$\sqrt{\text{Hz}}$ [49].

Instead of a breathing mode from a toroid resonator, a torsional resonator might be more advantageous for dynamical magnetism studies if the torque from an applied field can be measured sensitively. For the first time, using an on-chip optomechanical torque sensor, I reported a torque sensitivity of 40 zNm/$\sqrt{\text{Hz}}$ off-mechanical resonance (0.8 zNm/$\sqrt{\text{Hz}}$ at the mechanical resonance) [48]. Since then, other experiments were proposed to improve the torque sensitivity. For example, a levitated torsional oscillator shows a 10^{-22} Nm/$\sqrt{\text{Hz}}$ torque sensitivity for the purpose of studying gravity, modelled after the Cavendish experiment [23]. An interesting hybrid system of birefringent material with photonic crystal measured angular momentum of light [1]. Our collaborators have also pursued hybrid systems of permalloy and photonic crystals to study Barkhausen noise at ambient pressures [22].

Since my initial results of 0.8 zNm/$\sqrt{\text{Hz}}$ torque sensitivity, I have used our optomechanics-compatible dilution refrigerator to further minimize the thermal noise in the system, which directly improved our on-chip torque sensitivity down to 2.9 yNm/$\sqrt{\text{Hz}}$ at 25 mK. In addition, I have implemented magnetic materials to test its platform as a torque magnetometer to detect magnetic fields and study magnetic properties of the sample at room temperature. The magnetic materials chosen for this study follows the historical development of hard and soft magnets.

§ 1.3 Thesis outline

This thesis is organized in chronological order. Chapter 2 lays down the foundation of optomechanical torque sensing and magnetism. We will then move on to the design, fabrication, and apparatus common to all three experiments in chapter 3. Chapters 4, 5 and 6 goes in depth on each experiment. The first discusses all the work pertaining to achieving the record-breaking torque sensitivity of 2.9 yNm/$\sqrt{\text{Hz}}$. The second discusses the first implementation of torque magnetometry to iron-needles, where we extracted some magnetic

properties and demonstrated feedback damping. We verified experimentally that only passive cooling enhances the torque sensitivity. Lastly, we have demonstrated TMRS using a soft magnet, Py, for the first time using optomechanics. Following the theme of this project, I include prospects of other materials that can be used with cavity optomechanical torque sensors using a dilution refrigerator, specifically superconductors.

- Chapter 2 -

BACKGROUND

If you want to find the secrets of the universe, think in terms of energy, frequency and vibration.

- Nikolai Tesla

This chapter is designed to provide general background and analytical tools of optomechanical torque sensors. It will cover basics of thermomechanical calibration leading up to torque sensitivity, followed by the transduction scheme of optomechanics, and some concepts of magnetism. Most of the discussions will remain in the classical regime, except at low temperatures — where the uncertainty principle and zero-point motion plays an important role to describe the standard quantum limit of torque sensing.

§ 2.1 Ideal torsional harmonic oscillator

Consider a simple torsion paddle as laid out in Fig 2.1a; the restoring torque (τ) when the paddle is twisted by an angle θ is,

$$\tau = -\kappa\theta, \tag{2.1}$$

where κ is the torsion elastic constant in units of N·m and θ is the angular displacement in radians. If the moment of inertia around the rotation axis is I (kg·m^2), Newton's second law gives the angular vibration as,

$$I\ddot{\theta} + \kappa\theta = 0. \tag{2.2}$$

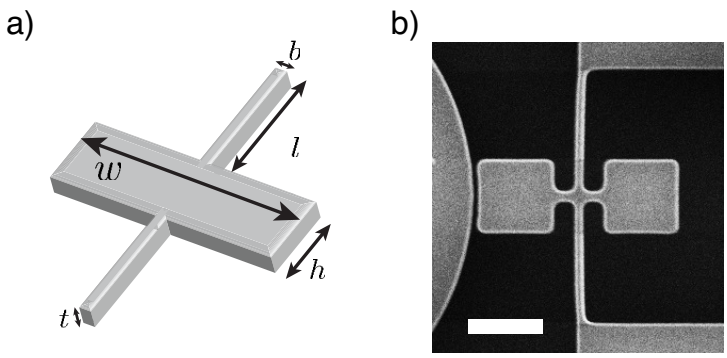

Figure 2.1: **Model of a simple paddle** (a) A torsion paddle with width, w, height, h, length, l, and thickness t. (b) An example scanning electron microscope (SEM) shows of optomechanically transduced torsion paddle used in Ref. [48]. The scale bar is 1.5 μm

Note that this is an ideal case without any dissipation, where the solution to the differential equation gives the natural radial frequency of the torsional mode as

$$\Omega_{\mathrm{m}} = 2\pi f_{\mathrm{m}} = \sqrt{\frac{\kappa}{I}}. \tag{2.3}$$

Here, the moment of inertia, I, is defined as

$$I = \int \rho(\boldsymbol{r})\boldsymbol{r}^2 dV, \tag{2.4}$$

where $\boldsymbol{r}$ is the displacement vector perpendicular to the rotation axis and $\rho(\boldsymbol{r})$ is the material density. For a simple geometry shown in Fig. 2.1a, the moment of inertia is $I = \frac{1}{12}mw^2$ and the analytical expression of a torsion spring constant is approximated by [50],

$$\kappa = \frac{2Sbt^3}{l}\left(\frac{1}{3}(1-0.63)\frac{b}{w}\right), \tag{2.5}$$

where S is the shear modulus (Pa). Using the geometry in Fig. 2.1b, and the properties of silicon [51], $S = 80$ GPa and $\rho = 2330$ kg/m^3, the natural radial frequency is $f_{\mathrm{m}} \sim 8$ MHz which is on the order of the experiment ($f_{\mathrm{m}} = 9.0$ MHz) [48]. A mild difference in frequency comes from the shape and asymmetry of the torsion paddle designed by the curvature of the microdisk as seen in Fig. 2.1b [48]. For more complex oscillator shapes, which we will see in later sections, the analytical expression of the torsion spring constant and the moment of inertia can be difficult to obtain; however, a numerical finite element method (FEM) using COMSOL can acquire natural frequencies of any torsional structure at ease.

Now, we take the dissipation (Γ) into an account in Eqn. 2.2 such that,

$$I\ddot{\theta} + I\Gamma\dot{\theta} + \kappa\theta = 0. \tag{2.6}$$

Solving this differential equation results in a lower resonant frequency (Ω_{d}) scaled by the quality factor defined by $Q_{\mathrm{m}} = \Omega_{\mathrm{m}}/\Gamma$,

$$\Omega_{\mathrm{d}} = \Omega_{\mathrm{m}}\sqrt{1 - \frac{1}{Q_{\mathrm{m}}^2}}. \tag{2.7}$$

However, we will consider high Q_{m} systems (or low dissipation) such that, $\Omega_{\mathrm{d}} \sim \Omega_{\mathrm{m}}$.

§ 2.2 Thermomechanical calibration

Regardless of the origin of the dissipation, fluctuation-dissipation theorem states that it acts to thermalize the motion of the resonator [52]. In the presence of finite dissipation, without any driving force, the mean total energy $\langle\varepsilon_n\rangle$ for each mode n of the resonator is given by

$$\langle\varepsilon_n\rangle = k_B T, \tag{2.8}$$

where T is the physical temperature of the resonator. More precisely, the two degrees of freedom of the mode displacement, amplitude (potential) and velocity (kinetic), have energies of $\frac{1}{2}k_B T$ each by the equipartition theorem. This is the working principle behind a thermomechanical calibration, where a certain mechanical amplitude corresponds to its environment temperature.

First, we characterize the mean-square angular displacement ($\langle\theta_{\mathrm{th}}^2\rangle$) due to thermal excitation by the spectral noise density, S_θ,

$$\langle\theta_{\mathrm{th}}^2\rangle = \frac{1}{2\pi}\int_0^\infty S_\theta(\Omega)d\Omega. \tag{2.9}$$

The thermal density term can be further described by,

$$S_\theta(\Omega) = |\chi(\Omega)|^2 S_\tau(\Omega), \tag{2.10}$$

where $\chi(\Omega)$ is the generalized susceptibility, or the response function, of the torsional oscillator. To find $\chi(\Omega)$, we add a thermal noise term to the damped harmonic oscillator equation

(Eqn. 2.6) such that,

$$\ddot{\theta}(t) + \frac{\Omega_{\rm m}}{Q_{\rm m}}\dot{\theta}(t) + \Omega_{\rm m}^2\theta(t) = \frac{\tau_{\rm th}(t)}{I}. \tag{2.11}$$

This equation is also known as the Langevin equation, where it was originally used to describe the Brownian motion (random motion) of a particle in a viscous fluid [53]. This equation is also valid for a single mechanical resonance interacting with the thermal environment. Applying a Fourier transform to Eqn. 2.11, we obtain the generalized susceptibility,

$$\chi(\Omega) = \frac{1}{I(\Omega_{\rm m}^2 - \Omega^2 - i\Omega\Omega_{\rm m}/Q_{\rm m})}. \tag{2.12}$$

Solving the integration in Eqn. 2.9, assuming that $S_\tau(\Omega) = S_\tau^{\rm th}$ is a thermal white noise, gives

$$\langle\theta_{\rm th}^2(t)\rangle = S_\tau^{\rm th} Q_{\rm m}/4\Omega_{\rm m}^3 I^2. \tag{2.13}$$

The equipartition theorem, in Eqn. 2.8, relates the equilibrium potential energy $\langle U\rangle$ to $1/2k_BT$,

$$\langle U\rangle = \frac{1}{2}I\Omega_{\rm m}^2\langle\theta_{\rm th}^2(t)\rangle = \frac{1}{2}k_BT. \tag{2.14}$$

Substituting the results from Eqn. 2.13 to 2.14 gives the thermal white noise as $S_\tau = 4k_{\rm B}T\Omega_{\rm m}I/Q_{\rm m}$, which allows the expression for the torsional angular displacement power spectral density (PSD) as

$$S_\theta(\Omega) = \frac{4k_BT\Omega_{\rm m}}{IQ_{\rm m}[(\Omega^2 - \Omega_0^2) + (\Omega\Omega_{\rm m}/Q_{\rm m})^2]}. \tag{2.15}$$

However, in addition to thermal vibrations of the torsional oscillator, there is also noise added to the measurement apparatus. This is generally treated as white imprecision noise, $S_V^{\rm imp}$, where a typical measurement takes on the form,

$$S_V^{\rm exp}(\Omega) = S_V^{\rm imp} + \alpha S_\theta(\Omega), \tag{2.16}$$

where S_V is the voltage PSD from measurements, and α is the conversion factor from voltage to angular displacement in units of V^2/θ^2. After obtaining the experimental PSD, we fit to the function,

$$S_V^{\rm exp}(f) = S_V^{\rm imp} + \frac{Bf_{\rm m}^3}{Q_{\rm m}[(f^2 - f_{\rm m}^2)^2 + (ff_{\rm m}/Q_{\rm m})^2]}, \tag{2.17}$$

where $S^{\rm imp}$, $f_{\rm m}$, $Q_{\rm m}$, and B are the four fit-parameters. Note that the frequency is expressed in $f = \Omega/2\pi$ for convenience. From the fit parameters, we can acquire two important

quantities, angular displacement noise-floor,

$$\sqrt{S_\theta^{\mathrm{nf}}} = \sqrt{S_V^{\mathrm{imp}}/\alpha} = \sqrt{S_V^{\mathrm{imp}} \frac{k_B T}{2\pi^3 I B}}, \tag{2.18}$$

and torque sensitivity,

$$\sqrt{S_\tau(\Omega)} = \sqrt{4k_B T \Gamma I + \frac{S_\theta^{\mathrm{nf}}}{|\chi(\Omega)|^2}}. \tag{2.19}$$

For a thermally resolved amplitude, which is generally true for a cavity optomechanical detection, Eqn. 2.19 can be reduced to,

$$\sqrt{S_\tau(\Omega_{\mathrm{m}})} \simeq \sqrt{4k_B T \Gamma I}, \tag{2.20}$$

at mechanical resonance. Note that the decay rate, Γ, is defined as the full-width-half-maximum (FWHM) of the mechanical resonance .

To compare sensitivities with other literature values, it is often convenient to use displacements in meters and forces in Newtons. By the small angle approximation, $\theta \sim z/(w/2)$, the following expressions are valid as a conversion between linear and angular terms,

$$S_z(f) = \frac{w^2}{4} S_\theta(f), \tag{2.21}$$

and

$$S_F(f) = \frac{4}{w^2} S_\tau(f), \tag{2.22}$$

where w is the width of the torsion paddle.

In addition to torque sensitivity, a thermal root-mean-square torque ($|\tau_{\mathrm{rms}}(\Omega_{\mathrm{m}})|$) can also be found at the mechanical resonance by

$$|\tau_{\mathrm{rms}}(\Omega_{\mathrm{m}})| = \left| \frac{\theta_{\mathrm{rms}}(\Omega_{\mathrm{m}})}{\chi(\Omega_{\mathrm{m}})} \right|, \tag{2.23}$$

where a root-mean-square angular displacement is

$$|\theta_{\mathrm{rms}}(\Omega_{\mathrm{m}})| = \sqrt{\frac{k_B T}{I \Omega_{\mathrm{m}}^2}}, \tag{2.24}$$

obtained from Eqn. 2.14. Further substitution of $|\chi(\Omega_{\mathrm{m}})| = \frac{1}{I \Omega_{\mathrm{m}} \Gamma}$ gives the thermal torque acting on the oscillator,

$$|\tau_{\mathrm{rms}}| = \Gamma \sqrt{k_B T I}. \tag{2.25}$$

§ 2.3 Concept of optomechanical transduction

It is often customary to begin the discussion of optomechanics with a Fabry-Pérot cavity where tiny vibrations of the mirror are magnified by the quality factor, or the finesse, of the optical resonator. The monumental example of interferometry at laser interferometer gravitational-wave observatory (LIGO) has 4 km long Fabry-Pérot cavities on both arms to extend the optical path length to 280 times, or 1120 km long, before they are merged together again. This is particularly important to conceive vibrations on the order of 10^{-20} m/$\sqrt{\text{Hz}}$, thousands of times smaller than a size of a proton [14]. The cavity-enhanced detection of this interferometer has lead to the experimental discovery of gravitational waves of two merging black holes [15], where more gravitational wave detectors are now being built around the world for astronomy applications. In improving the sensitivity, both the quality factor (Q_c) of the mirror and the input laser power (P_{opt}) played an important role. This platform, called cavity optomechanics, comes in all shapes and sizes depending on the application.

The principle of cavity optomechanics, as the name suggests, is a general system comprised of an optical cavity dispersively coupled to a mechanical oscillator. Here, I used optical disks, where the light is confined along the perimeter in WGM by total internal reflection, coupled to torsional resonators. While tuned-to-slope, indicated by the wavelength at the dashed line in Fig. 2.2c, the vibrations of the paddle shifts the resonance by,

$$\omega_{cav}(z_0 + z) = \omega_{cav}(z_0) + Gz \tag{2.26}$$

$$G = \frac{\partial \omega_{cav}(z_0)}{\partial z}, \tag{2.27}$$

where $\omega_{cav}(z_0)$ is the optical cavity resonance, z_0 is the equilibrium cavity length, z is the displacement of the mirror, and G is the optomechanical coupling coefficient, defined as the optical resonance frequency shift per unit displacement. Hence, the dynamics of the paddle (Ω_m, Γ) is encoded in the oscillating AC part of the optical transmission, enhanced by G and optical quality factor Q_{cav}. It is important to note that I used a dimpled microfibre that supports low-loss telecom wavelengths (1550 nm), as illustrated in Fig. 2.2a, and is evanescently coupled to a particular mode of the disk, shown in Fig. 2.2b. The fibre coupling apparatus is more efficient than the Bragg-gratings couplers typically used for on-chip photonic devices [17]. The procedure for making such a fibre is highlighted in the next chapter.

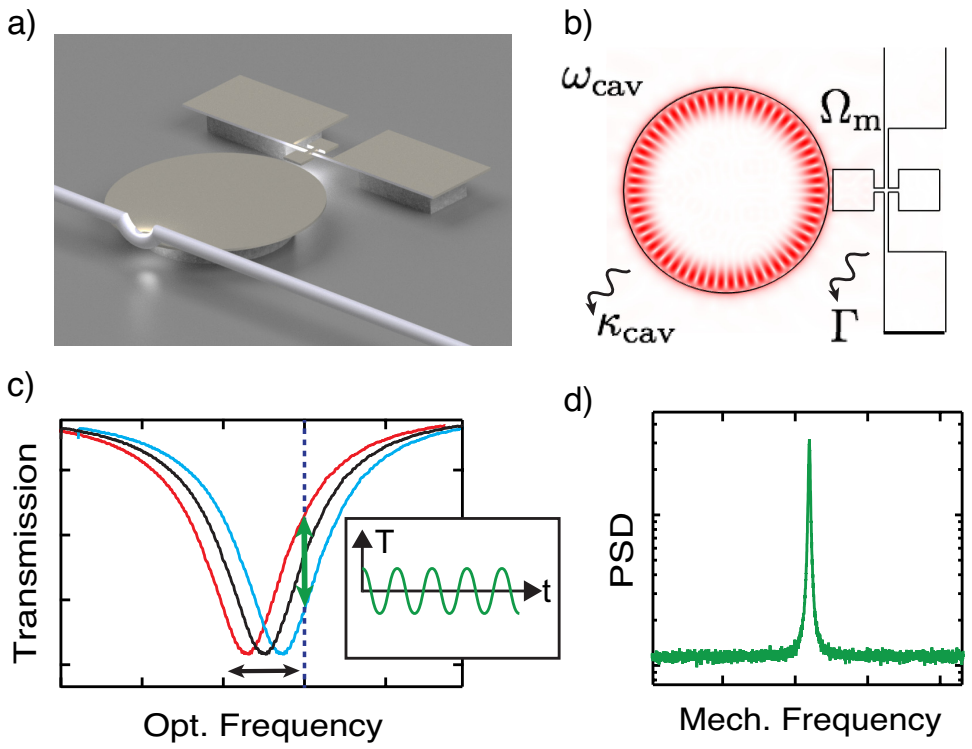

Figure 2.2: **Optomechanical transduction** (a) A rendition of a microdisk optomechanical system, where the torsion paddle is evanescently coupled to a microdisk by a small gap — allowing transduction of the mechanical motion through changes to a coupled optical resonance. Here, an optical dimpled tapered microfibre is used to inject photons to the microdisk, creating an optical mode shown in a (b) A FEM simulation of the optical mode with frequency ($\omega_{\rm cav}$) and optical loss ($\kappa_{\rm cav}$). Coupled to the microdisk is the mechanical frequency ($\Omega_{\rm m}$) and the mechanical dissipation (Γ). (c) As the laser is tuned-to-slope (dashed line) the time oscillating signal follows the mechanical motion as the optical resonance detunes to red and blue. (d) Analyzing the Fourier components to the time-oscillating signal, we can decompose the mechanical modes in a power spectral density.

§ 2.4 Optomechanics at cryogenic temperatures

Until now, we have discussed the thermal limit in mechanical sensors, where the thermomechanical calibration was possible through the equipartition theorem. Although the calibration method still holds true for all finite temperatures, we have to account for a new limit called, the standard quantum limit (SQL) at very low temperatures ($k_B T \sim \hbar\Omega_{\rm m}$). Here the SQL is based on the Heisenberg limit, where a precise measurement of a harmonic

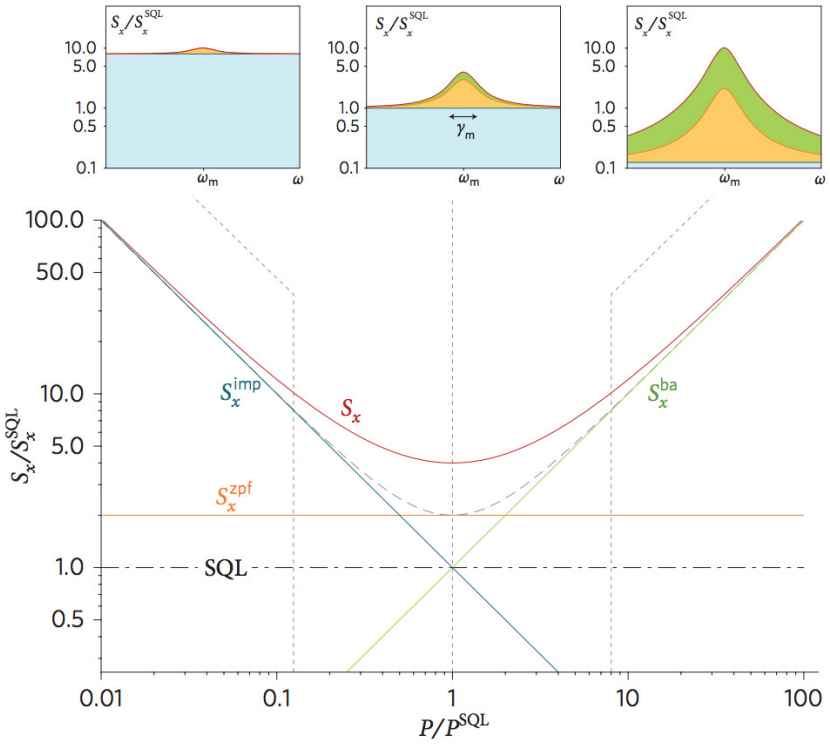

Figure 2.3: **Ideal displacement spectral density** The total displacement spectral density for $T = 0$ temperature (red) has three contributions: the zero-point fluctuation of the oscillator ($S_x^{\rm zpf}$), the imprecision given by the shot-noise limit ($S_x^{\rm imp}$), and the back action due to quantum fluctuation of the measurement signal acting back on the oscillator ($S_x^{\rm ba}$). At very low temperature there is also a thermal contribution. The SQL is at the crossover of $S_{\rm imp}$ and $S_{\rm ba}$, where $P_{\rm SQL}$ is minmimum. The main graph shows the contribution to S_x as a function of power and the sub-figures show the spectrum at three different locations of $P/P^{\rm SQL} < 1$, $P/P^{\rm SQL} = 1$, $P/P^{\rm SQL} > 1$ (image taken from Ref. [54]).

oscillator and the back-action (measurement signal acting on the mechanics) are complimented by $\hbar\Omega_{\rm m}/2$ [55]. The technical details of cryogenic operations and further discussions of quantum-limited sensing will be reserved for chapters 3 and 4.

2.4.1 Displacement spectral density

We first dissect the mechanical spectrum in three parts, as seen in Fig. 2.3 (note that S_x and S_θ are used interchangebly): the imprecision spectral density, $S_\theta^{\rm imp}$, the thermal noise, $S_\theta^{\rm th}$, and the back-action, $S_\theta^{\rm ba}$. The first part is typically a white noise from the detector, whereas the latter two parts are lorentzian peaks around the mechanical frequency. Nanomechanical

resonators typically operate in a regime where the thermal noise dominates, where the imprecision noise and back-action are negligible. At $T = 0$, the imprecision background and back-action can be expressed as a function of input power by [56],

$$S_\theta^{\mathrm{imp}} + S_\theta^{\mathrm{ba}} = \frac{S_\theta^{\mathrm{zpf}}}{2}\left(\frac{P_{\mathrm{SQL}}}{P} + \frac{P}{P_{\mathrm{SQL}}}\right), \tag{2.28}$$

where P_{SQL} is the power to reach the SQL for ideal lossless cavity optomechanical system. As we see in Fig. 2.3, the total added noise has a minimum at the crossover $P = P_{\mathrm{SQL}}$, where the standard quantum limit is defined. At this crossover, the mechanical spectrum has the zero-point fluctuations (S_θ^{zpf}) [57] and Heisenberg-limited quantum noises (back-action and imprecision).

2.4.2 Standard quantum limit of torque sensing

The quantum-limited expression for torque, is similar to the displacement case where each quanta of imprecision and back-action adds up to the minimum resolved torque ($n_{\mathrm{imp}} = n_{\mathrm{ba}} = 1/4$):

$$S_\tau = 4\hbar\Omega\Gamma I(\langle n\rangle + 1), \tag{2.29}$$

where $\langle n\rangle$ is the phonon occupation number. In the ideal case of $T = \langle n\rangle = 0$, the standard quantum limit is defined as $S_\tau = 4\hbar\Omega\Gamma I$. Further discussion about quantum-limited torque sensitivity will be explained in section 4.1.1.

2.4.3 Optomechanics at low temperatures

Fortunately, optomechanical devices are adaptable in cryogenic temperatures, where thermal vibrations, even at mK temperatures, can be transduced without an external drive. Consequently many efforts in the optomechanics community have been driven around investigating quantum mechanical behaviour of mesoscopic mechanical objects. Many sensitive, and interesting systems have been prepared in, or very close to, its mechanical ground state by active and passive cooling [58; 59]. These are promising platforms to study the crossover from classical to quantum systems [24]. In this thesis, an alternative effort to study other quantum systems are reported using our best on-chip torque sensor to-date.

§ 2.5 Torque actuation and feedback damping

The first example of a parametric amplifier was developed by an electrostatic force applied through a pair of capacitor plates between a silicon cantilever and the substrate [60]. A similar system of torsional oscillators used capacitor plates to drive a flexural force, but small asymmetries in the paddle permitted torque as well, yielding good sensitivity [61]. These torsional devices were carefully engineered by two interdigitated capacitors, where the torque was applied by applying an out-of-plane force at some distance about the rod and a downward force to the opposite side [62]. The purpose of the complex design was to supply a pure torque and not a net force upwards.

Another method for applying torque to torsional resonators is using magnetized magnetic materials under a alternating field. Utilizing this torque in a feedback loop, an active cooling can occur — where the output signal is fed directly to the drive field to actuate or damp the torsional mode depending on its phase. Here we include a feedback term in the Langevin equation (Eqn. 2.11) in addition to the thermal force ($\tau_{\rm th}$),

$$\ddot{\theta} + \Gamma\dot{\theta} + \Omega^2\theta = \frac{\tau_{\rm th}}{I} - g_{\rm fb}\Gamma e^{i(\phi+\pi/2)}(\dot{\theta} + \dot{\theta_n}), \tag{2.30}$$

where $g_{\rm fb}$ is the feedback gain, $\dot{\theta}_n$ is the measurement noise, and ϕ is the phase difference between the drive and the displacement. Details on further analysis is done in section 5.4.2, where we actively damped the torsional mode down to a cryogenic level. Unfortunately active cooling does not help in reducing the torque sensitivity, as the dissipation rate increases by the same rate as temperature decreases.

§ 2.6 Torque mixing magnetic resonance spectroscopy

A hybrid system, where a magnetic material is embedded on a torque sensor, not only manipulates the motion of the oscillator but also can be used to extract the magnetic properties. More specifically we can infer saturation magnetization of the material or study magnetic spin modes.

2.6.1 Types of magnetism

The origin of magnetism comes from electrons in a material having magnetic moment due to their orbital and spin angular momentum. Most materials, however, are nonmagnetic

because individual magnetic moments are oriented randomly. In contrast, there are materials with magnetic dipoles aligned in such a way that the net magnetic moment is non-zero, which can be classified in two large categories: ferromagnetism and paramagnetism. Many branches exists under these types [31], however we restrict our discussion in two extreme cases of diamagnetism and ferromagnetism.

To determine whether a material is magnetic or not, we need at least one quantity that can describe the material's magnetic behaviour under an applied field. The quantity, termed magnetic susceptibility χ_m characterizes the magnetic response of a material through the relationship,

$$\boldsymbol{M} = \chi_m \boldsymbol{H}, \tag{2.31}$$

where $\boldsymbol{M}$ is the magnetization, also known as magnetic moment per unit volume and $\boldsymbol{H}$ is the applied magnetic field. Depending on the values of susceptibilities and the relationship of $\boldsymbol{M}$ and $\boldsymbol{H}$, classification of magnetic materials can be established such as diamagentism, paramagnetism, antiferromagentism, ferrimagnetism, and ferromagnetism in increasing magnitude. As an example of diamagnetism, values of relative susceptibility is $\chi_0 = \chi_m/\mu_0 \sim -10$ in contrast to $\chi_0 \sim 10^6$ for ferromagnetism.

2.6.1.1 Diamagnetism

Most nonmetals and many metals are diamagnetic, which is a weak form of magnetism — attributed from the orbital motion of electrons that create magnetic moments. However, an induced flux from an applied magnetic field opposes the change in the external field so that diamagnetic materials show an antiparallel magnetization, according to Lenz's law. Although diamagnetism may seem dull to study, two interesting points may be investigated. If only a few magnetic atoms exist in the material, their influence may be enough to overshadow its diamagnetism, so that nonmagnetic atoms become spin-polarized by neighbouring magnetic atoms. This is explored nowadays in spintronic devices [63]. Another example is superconducting materials, where they become a perfect diamagnet below the transition temperature. I am particularly interested in superconductors to study the dynamics of vortices created from high magnetic fields and mesoscopic properties [64; 65].

2.6.1.2 Ferromagnetism

Historically, ferromagnetic materials were the ones considered 'magnetic' from their early discovery. Ferromagnetic materials are highly permeable, depending on the field strength and on the previous magnetic history, or hysteresis loop, mentioned previously. Ferromagnets

contain spontaneously magnetized magnetic domains, whose magnetized small region of atoms with magnetic moments will tend to align parallel to each other. The domains exists because the domain structure will strive to remain stable, or minimize energy, therefore, molding until it finds this stability point. Typically the exchange interaction between the domains are strong for ferromagnets, and remains magnetized against thermal agitations. However at high temperatures the spontaneous magnetization disappears above a certain temperature called the Curie temperature, when they become paramagnetic. In this thesis, all experiments were performed below the Curie temperature.

2.6.2 Torque mixing magnetic resonance spectroscopy

Torque mixing magnetic resonance spectroscopy (TMRS) is a new technique, using torque magnetometry, to probe spin modes of magnetic materials. Rather than direct observation of spin resonance using radio-frequency (RF) absorption, a torque-mixing of two frequencies are used to torque at the mechanical frequency of the oscillator [66]. Starting from the torque expression from magnetization and applied field, as in Eqn. 1.1, an explicit torque can be written as,

$$\tau_y = V\chi_m H_x(f_x) \times \mu_0 H_z(f_z), \tag{2.32}$$

where V is the volume of the material. The two fields, transverse (H_x) and out-of-plane (H_z), are chosen such that the difference in frequency is the mechanical frequency of the oscillator ($f_x - f_z = f_\mathrm{m}$). Hence the torque mixing occurs when the magnetic spin-modes are down-mixed to the actuated mechanical resonance of the torsional oscillator in a simplified form,

$$\tau_y(f_\mathrm{m}) = \frac{\mu_0 V H_x H_z}{2}\chi_m. \tag{2.33}$$

The motivation behind obtaining the best possible torque sensitivity is to use the TMRS to study various materials, even superconductors. This method is simple, non-invasive, and elegant such that fundamental studies of physics and applications can happen.

2.6.3 Microwave to optical frequency converter

One of the many application of quantum computation is to transmit microwave signals converted to long-ranged telecom signals through optical fibres. One approach built an optomechanical bi-directional converter using a flexible silicon nitride membrane coupled to both a microwave circuit and a Fabry-Pérot optical cavity [67]. Rather than using microwave circuits, spin-modes of a soft magnet in GHz range may be used for such coherent conversion since a hybrid system links optical frequencies to microwave frequencies by its mechanical frequency.

- Chapter 3 -

DEVICE DESIGN, NANOFABRICATION, AND CHARACTERIZATION

God is in the details.

- Ludwig Mies van der Rohe

In this chapter we turn from a theoretical summary of mechanics to a description of detailed experimental procedures, to expound on nanofabrication techniques and the operating principles behind a dilution refrigerator that produced the best NOMS torque sensor to date [68].

§ 3.1 Device design

To strike a balance between the optomechanical coupling coefficient and the moment-of-inertia, a singly clamped torsional geometry, labelled "pluto" devices, have been thoroughly investigated — where the Q_{m}, I, and G were superior over the initial structure in Ref. [48]. This chapter contains my early work, where emphasis will be given to design principles of minimizing torque sensitivity using cavity optomechanics. I will also include other examples of cavity-optomechanical torque sensors to directly compare with my design, to highlight some advantages and disadvantages of each system.

3.1.1 Design principles

A prerequisite to torque sensitivity expression in Eqn. 2.20 is a thermally resolved signal, which requires high optomechanical coupling coefficient (G), or a large optical resonance shift

per mechanical displacement. From the first report on cavity optomechanical torque sensor in Ref. [48], I have demonstrated $G = 82$ MHz/nm for the best device, out of nine geometries tested. To have a large G, the overlap between the optical fields and the displacement fields have to be large, *i.e.* small gaps between the two resonators and smaller optical mode volume. Utilizing a powerful fabrication tool called electron-beam lithography (EBL), we can obtain smaller and smoother features than the foundry-based fabrication.

Revisiting the simplified expression in Eqn. 2.20, the torque sensitivity does not improve based on its transduction scheme as long as the thermomechanical signal is sufficiently large. Hence, only marginal improvements were made to torque sensitivity from 0.8 zNm/$\sqrt{\text{Hz}}$ to 0.5 zNm/$\sqrt{\text{Hz}}$ based on the trimmed torsional arm to reduce the moment of inertia. Although it may seem that the improved optomechanical coupling would provide no advantage to torque sensitivity at the mechanical resonance, the frequency band increases over the maximum sensitivity proportional to a large G. Hence a cavity optomecahcnial sensor with high bandwidth and high force sensitivity have been demonstrated [69]. To improve my torsion design, a large G is achieved by extending its arc along the microdisk's perimeter while having a small I. The final design, named "pluto", will be shown in Sec. 3.1.3. In addition to the large bandwidth measurement, a large signal-to-noise ratio helps sensing at low temperatures as the amplitude scales down linearly with temperature. Further results and discussion will follow in in chapter 4.

3.1.2 Other examples

Substantial efforts have been made over many years in the nano- and micro-electromechanics communities to improve the measurement precision and thereby reach the thermomechanical noise dominated regime, and to reduce the noise floor in this regime by decreasing Γ and I [71]. Harnessing the power of optomechanics to miniaturized on-chip devices, there are a host of other systems, ranging from optical toroids to photonic crystals and from cantilever motion to high-frequency breathing modes that are coupled in the $G \sim$ GHz/nm range [57]-[74]. Narrowing the subject to magnetometry, the first demonstration of an optomechanical magnetometer showed 400 nT/$\sqrt{\text{Hz}}$ field sensitivity [49], where the field sensitivity improved to 0.2 nT/$\sqrt{\text{Hz}}$ [75]. Other examples of optomechanical torque sensors were employed to study angular momentum of light, micro-gravity, and magnetism [1; 23; 49]. For the first example in Fig. 3.1a, a racetrack resonator was used where the torsion paddle is inserted along the path. Birefringent material is deposited along the torsion paddle where the angular momentum of photons apply torque in the paddle, modelled after the original experiment in Ref. [76]. The second example is the extreme case of paired levitated spheres to study the torque along the polarized direction. This system is a modern example of torsion pendulum

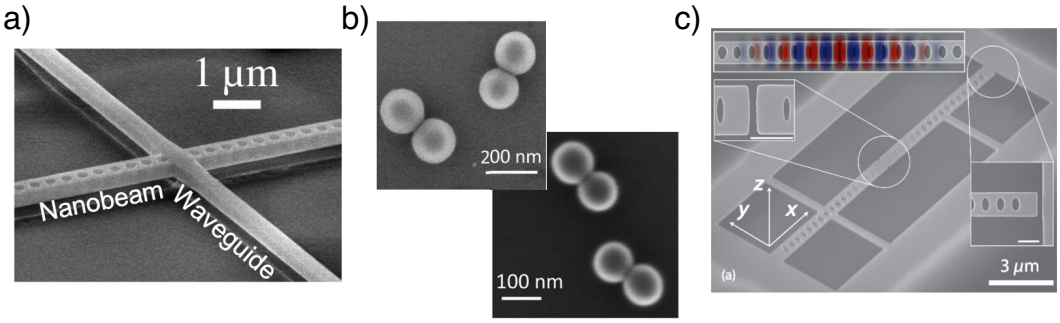

Figure 3.1: **Other examples of optomechanical torque sensors** (a) A racetrack resonator optomechanically detects torque on the nanobeam such that the photon spin angular momentum can be studied (taken from Ref. [1]). (b) A set of paired silica nanodumbells is levitated optically to minimize the moment of inertia to the extreme, where the reported torque sensitivity is on the order of 10^{-22} Nm/$\sqrt{\text{Hz}}$. Optimizing the parameters of the nanodumbells and the optical trap, the proposed torque sensitivity can be enhanced down to 10^{-27} Nm/$\sqrt{\text{Hz}}$ (taken from Ref. [23]). (c) A work from our collaborator demonstrates a comparable torque sensitivity near 0.8 zNm/$\sqrt{\text{Hz}}$ at ambient pressure, where the device is based on a photonic crystal design (taken from Ref. [70]).

designed to study the gravity between two objects. This system, when 10^{-27} Nm/$\sqrt{\text{Hz}}$ sensitivity is accessible, could study gravity in mesoscale [23]. The last example in Fig. 3.1c is similar to the device I integrated but using photonic crystals instead of microdisks. A complete overlap of optical and mechanical resonators allow a very sensitive detection, even at ambient pressures and room temperatures. However, my design may be advantageous for low temperature applications, where the two entities are separated by a small gap that aids in thermalization without much optical heating.

3.1.3 Evolution of designs

Since the first demonstration of an optomechanical torque sensor [48], which took root from the design in Fig. 3.2a, I immediately worked on the next generation of optomechanical torque sensors using e-beam lithography. The e-beam lithography allows smaller gaps to be formed between the optical and the mechanical resonators on the order of ∼50 nm. Examples of bow-tie, hatchet, ring-resonator, and pluto devices gave improvements of torque sensitivity while increasing the optomechanical coupling coefficient (G), summarized in table 3.1. While working on the low temperature apparatus to minimize the temperature, the optimization process of nanofabrication continued. In the next few sections, I will highlight some nanofabrication techniques developed during this period.

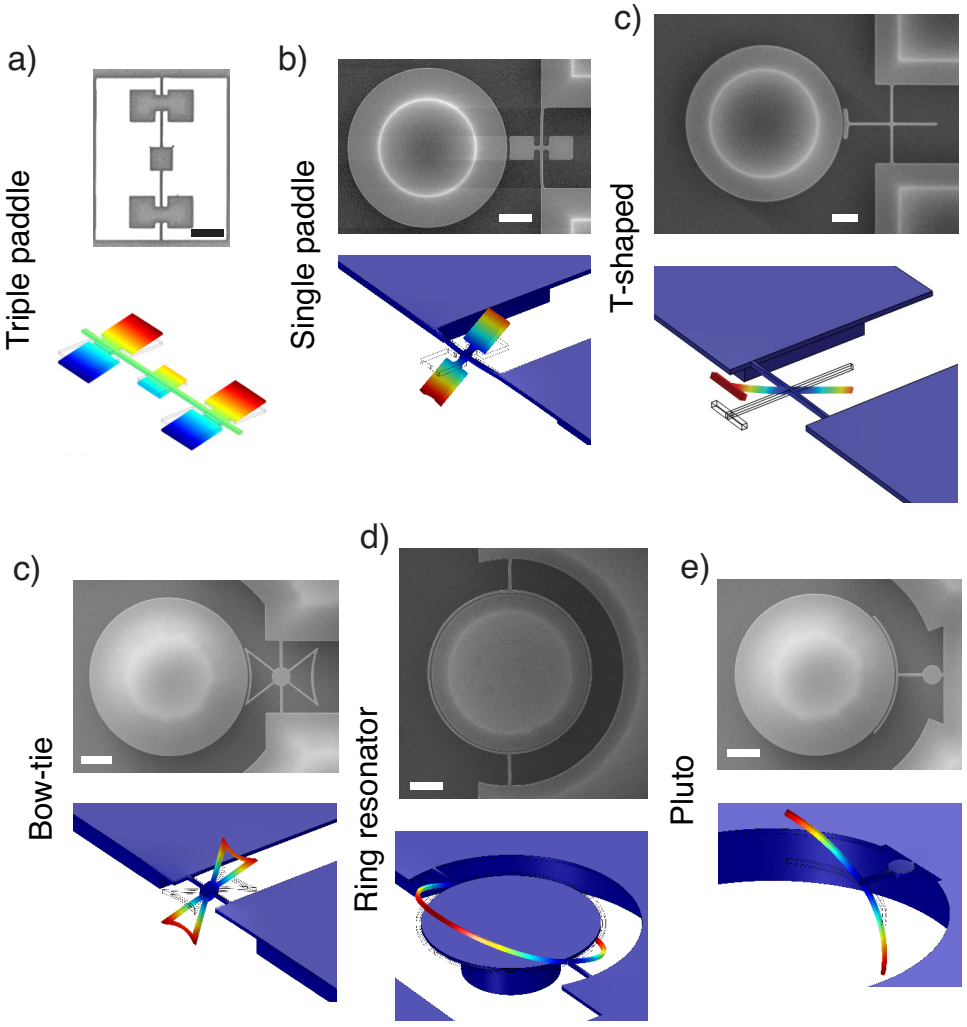

Figure 3.2: **Family of on-chip optomechanical torque sensors** (a) An SEM of the root experiment with a triple paddle simulation on the bottom. Torque magnetometry on a Py disk in the middle was studied using an interferometric detection. (b) My first inception of a cavity optomechanical structure, demonstrating 0.8 zNm/$\sqrt{\text{Hz}}$ at the torsional resonance. (c) The next attempt, named "bow-tie" involved in trimming the mass on a paddle to reduce the moment of inertia, while keeping the coupling arc increased. (d) Another variation named "hatchet" device, is designed to reduce the width in half of the bow-tie design. (e) The ring resonator is an extreme case, where the torsion ring is coupling around the perimeter. Consequently a thermomechanical signal is large, but the torque sensitivity suffers due to a larger moment of inertia. (f) The pluto device, a singly clamped torsional device that has both high G and low I, was my final design for a cryogenic optomechancial torque sensor. All the scale bars are 2 μm.

Device	I (g·pm^2)	$\Omega_m/2\pi$ (MHz)	Q_m	$\sqrt{S_z}$ (fm/$\sqrt{\text{Hz}}$)	$\sqrt{S_\tau}$ (zNm/$\sqrt{\text{Hz}}$)
Paddle:	2.8	9.0	3800	7	0.8
Bow-tie:	3.0	10.9	8100	49	0.7
Hatchet:	1.6	14.5	8000	121	0.6
Ring:	39	5.1	13000	338	1.3
Pluto:	0.9	11.1	8200	24	0.5

Table 3.1: Summarized results of various optomechanical torque sensors. Evolution of different geometries allow improvements in the torque sensitivity at room temperature. Key results are shown with corresponding device names, after the model in Fig. 3.2.

§ 3.2 Nanofabrication

A general fabrication process is well-known for micro-electro-mechanical systems (MEMS), where specific details regarding the maximum capabilities of each equipment have to be carefully optimized and characterized. In the subject of nanofabrication, I have divided this discussion into multiple chapters. In this section I will describe a conventional method of torsional optomechanical fabrication, followed by detailed adjustments to the recipe tailored to each project in the next few chapters. These include thin-film technologies of metal deposition, a lift-off process of aligned structures, and the use of vapour hydrofluoric acid (VHF) to preserve magnetic properties while creating suspended torsional structures. The techniques for nanoscale fabrication is continually evolving, and any development-orientated processes will be described in the appendix.

3.2.1 Background

The materials used for nanofabrication include insulators, semiconductors and metals that are primarily a planar structure. In particular, semiconductor complimentary metal-oxide-semiconductor (CMOS) industry used doped-silicon, where the conventional nanofabrication techniques were developed. The availability of single-crystal silicon, together with low-stress polycrystalline silicon and silicon nitride films, drove much of the MEMS research and applications, where photoresist-patterning and wet-etching was primarily used to make delicate structures [77]. Here, I use the same process-flow to create optomechanical structures on SOI platforms having great mechanical properties from crystalline structure and optical properties having high index of refraction of 3.486 (at $\lambda = 1.45$ μm) [78]. In preview, the top Si layer was first patterned, with exposed areas into the underlying oxide layer etched,

and the suspension occurs using a selective hydrofluoric acid (HF) etch to remove the oxide while leaving the top structural layer intact [79].

Metal electrodes have been routinely used for driving and detecting its mechanical motion, which requires an additional lithography step — a polymethylmethacrylate (PMMA) film can be used for liftoff mask for electrode metalization. For my project, I have used the bi-layer lift-off recipe to pattern magnetic films for torque magnetometry. The chips used in the next few chapters were all made from the Nanofab facility, where sub-micron features were especially challenging to fabricate. Here I include both the limitation and the possibility of the advanced equipments I used.

3.2.2 General process flow

Nanostructures are created in a sequence of fabrication steps, where each step involves with a definition of a pattern in a temporary polymer known as resist. The patterning of the resist is followed by either removal of underlying material or addition of new material on top of the resist. Much effort, therefore, is devoted to develop a process that might offer efficient execution speed, repeatability, and resolution, with the hope of demonstrating a level of control at the molecular level. The fabrication sequence for a complete NOMS torque sensor, with the end result, is illustrated in Fig. 3.3a. This chip has a 250 nm thick single-crystal $\langle 100 \rangle$ boron-doped silicon layer (p-type) as the active layer bonded to an oxide-grown (3 μm) silicon substrate (500 μm) via a smart-cut process [80]. The fabrication begins with a deposition of an electron beam resist (ZEP-520a), on a clean surface of the Si layer. The resist is then selectively exposed to electrons controlled by a pattern generator (RAITH-150Two). The exposed area can then be dissolved away when the chip is placed in a developer (ZED-N50), generating openings in the resist layer. The opened areas are then dry-etched chemically with reactive charged ions (Oxford ICP-RIE). After cleaning the e-beam resist with PG-remover followed by Caro's acid (or piranha solution, a 3:1 mixture of H_2SO_4 and H_2O_2), a timed wet-etch of the sacrificial layer is performed using a buffered-oxide etch (BOE) solution — resulting a suspended torsional oscillator as seen in Fig. 3.3b. One important final step to note is the critical-point drier (CPD) to avoid any closing of small gaps due to surface tension of water. The CPD utilizes elevation and reduction of pressure and temperature to avoid the direct phase change of LCO_2. In the next few sections, I will go through some of the fabrication steps in detail with some principles from start to finish.

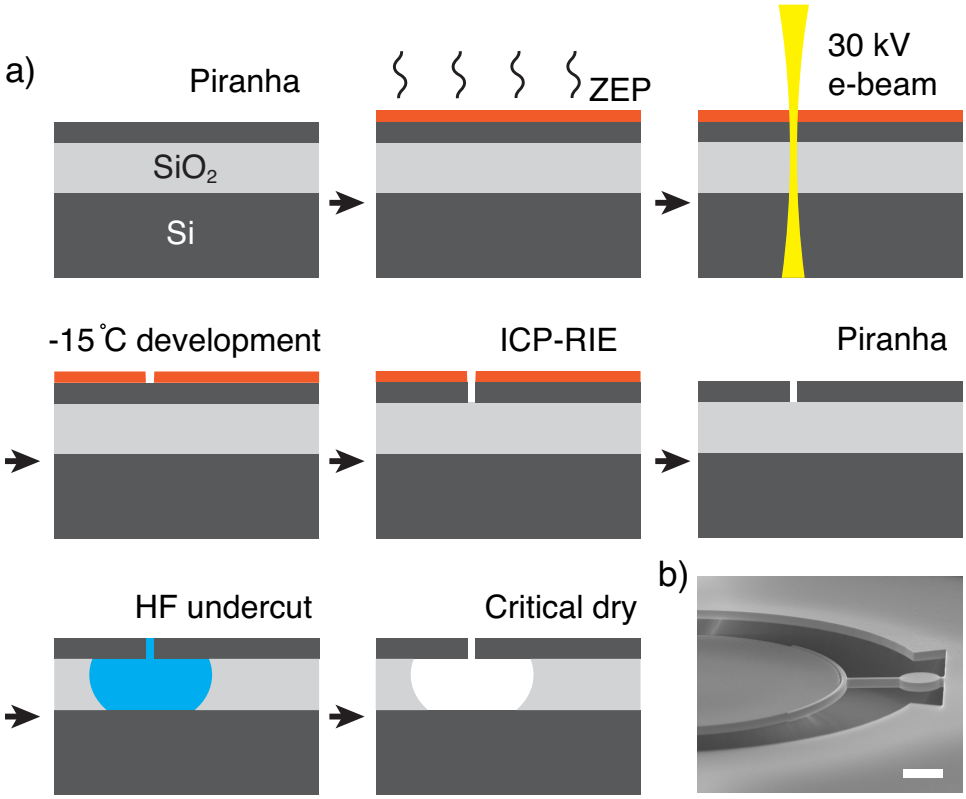

Figure 3.3: **General process flow for NOMS torque sensor fabrication** (a) Starting at the top left, the cross section of the heterostructure is shown, which consists of a bulk substrate, a sacrificial layer, and a top active layer. Moving to the right the sequence of fabrication is shown across the figure. The electron-beam resist is coated on the substrate, and patterned using a cold development, after which reactive-ion etch is used on the exposed area to pattern the torsional oscillator. After the resist is cleaned with a piranha solution, a final step of a timed BOE etch is used to remove the sacrificial layer, followed by a critical-point dry method to avoid stiction in small gaps. (b) A SEM of the end result is shown where a singly-clamped torsional oscillator is suspended and separated to the optical microdisk. The scale bar is 1 μm.

3.2.2.1 Chip design

Nanoscale devices made from the above fabrication sequence, namely e-beam lithography, allow multitude of devices to be patterned on a small chip of 5 mm $\times$ 10 mm. For example, all the geometries viewed in Fig. 3.2c-e, including variations of design parameters, can be patterned in a small window size of 1 mm $\times$ 1 mm with hundreds of devices. Once the desired geometry is confirmed, a separate GDS layout-tool is used to create a CSF file for pattern generation. Here I have not used the built-in design tool in RAITH-150Two software;

instead, I have used the MATLAB GDS library to create a script with parameters inputs such as optical disk diameter, gap length between the resonators, and the parameters for torsional geometry [81].

3.2.2.2 Methods of cleaning

Maintaining a clean chip throughout the fabrication steps is the first and foremost priority. Hence, a chip is handled in a class 100 cleanroom at the University of Alberta nanoFAB, which measures particle (>0.3 μm) counts of about nine per cubic meter volume daily. A chip is routinely cleaned by solvents, such as acetone and isopropyl alcohol (IPA) and deionized water (DH_2O). Sometimes ultrasonic bath may be required after an inspection through a microscope. If residues are still found, oxygen plasma is used to descum any residues left on a chip. Ultimately the best cleaning solution is using an aggressive piranha bath, typically in the very beginning and in the final step, to remove any organic materials on a chip. Piranha is a three-to-one mixture of H_2SO_4 and H_2O_2 and boils to $\sim$ 120°C immediately upon mixing. For larger volume of the mixture, the temperature stays hot for longer periods, where I typically use 1200 mL of sulfuric acid and 400 mL of hydrogen peroxide to clean a small chip for 30 minutes. There is also a temperature gradient from the top at 120°C to the bottom at 40°C, where the chip is immersed near the meniscus. Although omitted in Fig. 3.3a, a quick dip in a diluted HF (H_2O:HF = 10:1) is followed after piranha cleaning to remove excess oxide formed on silicon surfaces.

3.2.2.3 e-beam resist

Resists are used in two main applications: as etch masks and as lift-off masks. In the former case, the resist is patterned via e-beam lithography and the active layer is selectively etched through the openings in the resist using dry-etch. Since the resist must withstand an aggressive plasma dry-etch, an important criterion for choosing a resist must show good selectivity against the active layer. For example, a ZEP520a resist has a high selectivity of $\sim$ 1.2 to Si whereas PMMA has $\sim$ 0.3 for a certain dry-etch condition. Both ZEP520a resist and PMMA are capable of creating sub-micron features. Hence, ZEP520a is primarily used for patterning the optomechanical geometry and PMMA is spun as a lift-off resist of magnetic materials. In a lift-off mechanism, material is deposited, by evaporation or sputtering process, on top of the patterned resist. Openings in the resist allows the material to attach itself to the substrate, while elsewhere it remains on the resist surface. Removal of the resist then takes the deposited material on its surface with it — leaving the material where the openings in the resist were. To yield a good lift-off geometry, the deposited material must be disconnected from resist surface. This is achieved in a method called the bi-layer

process, with an underlying layer of lower molecular weight resist, which requires a lower electron dosage for dissolution. As we will see in Chapter 5 and 6, this method produces a well-defined shape in hybrid structures. Note that resists are generally classified as positive or negative resists: a positive resist is one whose solubility in the developer increases when it is exposed to electron-beam, while the solubility of a negative resist decreases. I have mainly used positive tone resist (ZEP520a) for most of my chips, where a negative tone resist of hydrogen silsesquioxane (HSQ) was highly sensitive and inconsistent upon each usage.

3.2.2.4 Principles of electron-beam lithography

Electron-beam lithography is not that different from photolithography, except that the UV source used to expose a photosensitive resist is replaced by an electron source with electron-sensitive resist. For a number of commercial systems, including the EBL station at nanoFAB, these can demonstrate linewidths below 10 nm. Electron-beam lithography remains primarily a research and development tool rather than a production tool because it is a serial-write process rather than a parallel process, and the electron beam directly exposes only a single focused spot at a time rather than exposing an area. This significantly reduces the throughput in comparison to optically-based approaches, and therefore increases the cost of use in a production setting [82]. For example, a design with ~ 50 torsional devices took about five hours to write.

In terms of feature limitation, an electron source is desired over the UV source based on the diffraction limit. Looking at the de Broglie relation,

$$\lambda = \frac{h}{p}, \tag{3.1}$$

the wavelength (λ) of an electron is determined by Planck's constant, h, and its momentum, p. If an electron is in an electric potential, the momentum, $p = \sqrt{2meV}$, gives the wavelength as,

$$\lambda = \frac{h}{\sqrt{2meV}}. \tag{3.2}$$

As an example, the wavelength of electrons in a 30 kV accelerating voltage is 7 pm, much smaller than UV wavelengths used in photolithography. To achieve smaller wavelengths, higher accelerating voltages or different ions can be used for modern techniques. As an example for a helium ion microscope (HiM) at the nanoFAB, the de Broglie wavelength is much smaller due to the heavy mass of helium ions ($m = 6.7 \times 10^{-27}$ kg) over the mass of electrons ($m = 9.1 \times 10^{-31}$ kg) where we may be able to use ion-milling to create small gaps between the optical and the mechanical design as a prospect.

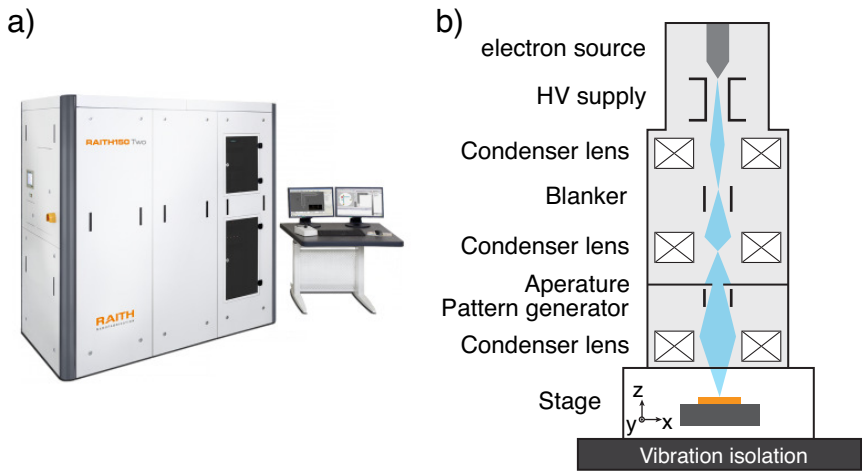

Figure 3.4: **Principle of electron-beam lithography** (a) A commercial picture of the RAITH-150Two EBL system is shown, placed inside the lithography room at the nanoFAB cleanroom. (b) Inside the sophisticated equipment, a simplified schematic shows the operating principle of a EBL system. From a field-emitted e-beam source, the electron beam is accelerated by a high voltage potential, which undergoes a series of beam-blanker, aperature, and pattern generator, with magnetic coils in between for focusing. A beam-blanker is required to avoid continuous exposures between structures. An micron-size aperature is needed to shape the e-beam profile at the surface of the chip. A pattern generator is what distinguishes an e-beam system from a scanning electron microscope, where the pattern generator directly exposes the resist on a chip. The stage has a separate vacuum system where it can move from one write-field to another. The whole apparatus is placed on a vibration isolation platform to minimize mechanical vibration during the long writing process.

The operation of an e-beam lithography system (RAITH-150Two) is based on a scanning electron microscope (SEM) platform, equipped with a computer controlled pattern-generator and stitching capability for each write-field, allowing full lithographic patterning over large areas. As illustrated in Fig. 3.4, a beam of electrons are emitted by a highly sharpened tungsten (W) tip, where the field-emission generate a very narrow range of electron velocities. This allows very precise focus and control over the electron beam, and yields extremely high resolution even when a field-emitter is operated at low voltages.

Once the electrons are extracted from the source, they are accelerated by electric fields, ranging from a few kV up to 30 kV in EHT (accelerating voltage), and a system of magnetic lenses, beam stop, and apertures is used to focus and narrow the beam (see Fig. 3.4). Magnetic coils are used to direct the beam to different points inside a write-field. At the end of the column, a chip resides in a vacuum chamber of $\sim 1 \times 10^{-6}$ Torr on a computer-controlled motorized stages. The electron beam passes through the top surface and then

scatters within the volume of the sample. Radiation in the form of secondary electrons are emitted from the sample, where this is the primary imaging mechanism for SEM.

When making a small gap in an optomechanical design, an intrinsic limit to resolution comes from the electrons scattering within the resist and backscattering into the resist after passing through the device layer. At low energies (< 10 kV) electrons scatter readily, which exposes the e-beam resist more than its design area. At high accelerating voltages (> 30 kV), the scattering inside the resist is minimal and the backscattering occurs deep inside the substrate. With a small aperature of 10 μm, small features on the order of 10 nm can be patterned on the resist. In order to improve the minimum feature size as well as improving writing speeds, a higher energy system (100 kV) is desirable.

The lateral scattering of electrons also affects patterns that include a large number of closely-spaced fine structures, or small features designed near large ones, causing over-exposures to adjacent features. This is known as the proximity effect, where the corners of the structures are rounded-off and the hole sizes of an array may vary. In photonic crystals, for example, the hole size and the hole spacing are crucial design parameters, where proximity effect must be considered carefully. Fortunately, this effect is compensated by a tool-kit in the Raith-150Two software where the dose is adjusted around fine features. For my designs, in particular, the proximity effect has little contribution, where a slightly larger dose was needed to reveal a small gap.

Another issue to address is the stitching error, where the device might not be aligned to its adjacent write-fields. Typically the stitching error is small (< 30 nm after 150 write-fields) but it is destructive to photonic structures if designed poorly. Since my apparatus uses an efficient dimpled tapered fibre for coupling, long waveguides are omitted. Hence, my design is completely stitch-free, where two devices are centered in each 100 μm $\times$ 100 μm write-field.

3.2.2.5 Resist development

The final step in the lithography process is the resist development, where the exposed positive-tone resist is removed by submerging the chip in a wet solvent. Rather than diluting the solvent to control the dissolution rate, a cold-development is used to slower the development process as well as straightening the e-beam side-walls such that smaller gaps can be achieved. Using a Stir-Kool SK-12D system, as seen in Fig. 3.5, it takes about thirty minutes to cool the ZED-N50 developer to -15°C, after which the chip is developed for 20 s

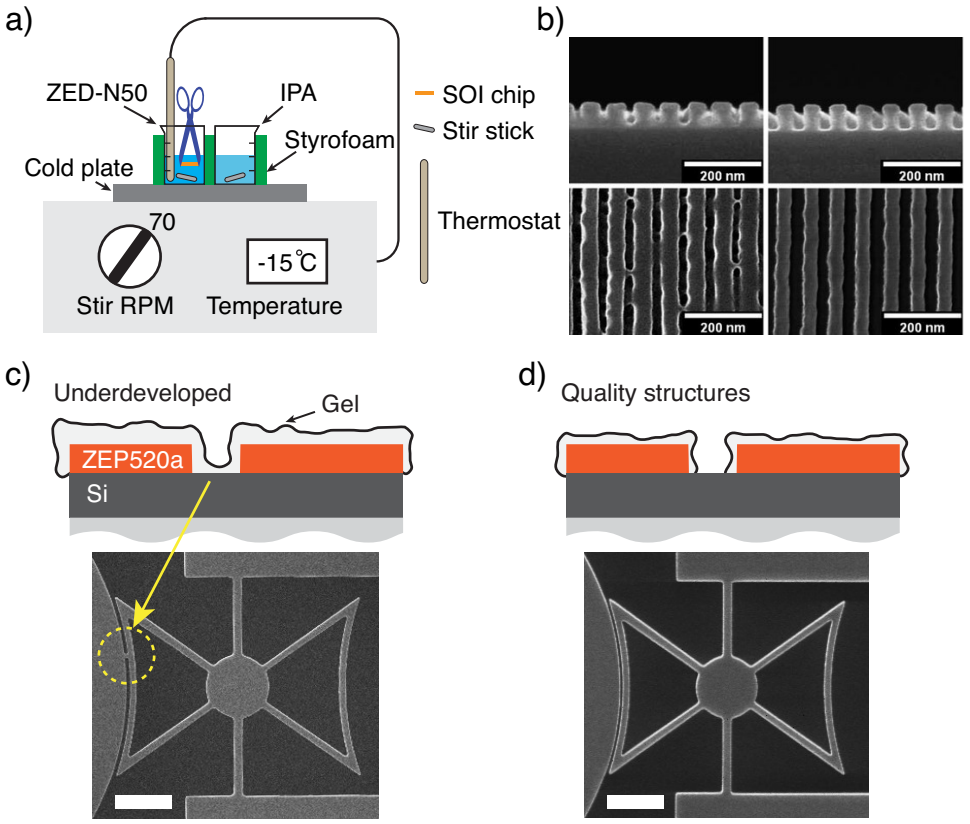

Figure 3.5: **Cold development and small gaps** (a) To create small gaps and straight side-walls in resists, cold-development is required. Two beakers are prepared on a cold-plate: a ZED-N50 developer and an IPA solution. The beakers are sanded on the bottom, where silicon grease droplets are applied to have a better thermal contact to the cold plate. With a Styrofoam thermal isolation and a small stir-stick, it takes about 30 minutes to reach -15 C. The development is done by 20 s stirring in ZED-N50 developer and 20 s rinsing in IPA, followed by a N_2 dry. (b) For small-aspect-ratio designs, a gel, formed on the surface of the e-beam resist, can link the features due to underdevelopment — as seen by the cross-links on the left column. The SEM on the right column shows the fully developed process where the gaps are visually seen (from [83]). For (c) and (d), I have shown my examples of underdeveloped and fully developed structures, respectively, for a 60 nm gap. The interplay between the exposure dose, development, and the cold-plate temperature plays an important role in attaining the smallest gap possible in my optomechanical design. The scale bar is 1 μm

followed by a 20 s IPA quench. Note that the developing process creates a small gel film on the surface [83]. When the gap is too small, or the dose is slightly low for its development, sometimes a bridge is formed in the gap. Hence a thorough dose-testing and a consistent development is required for the best-achievable gap between the optical and the mechanical

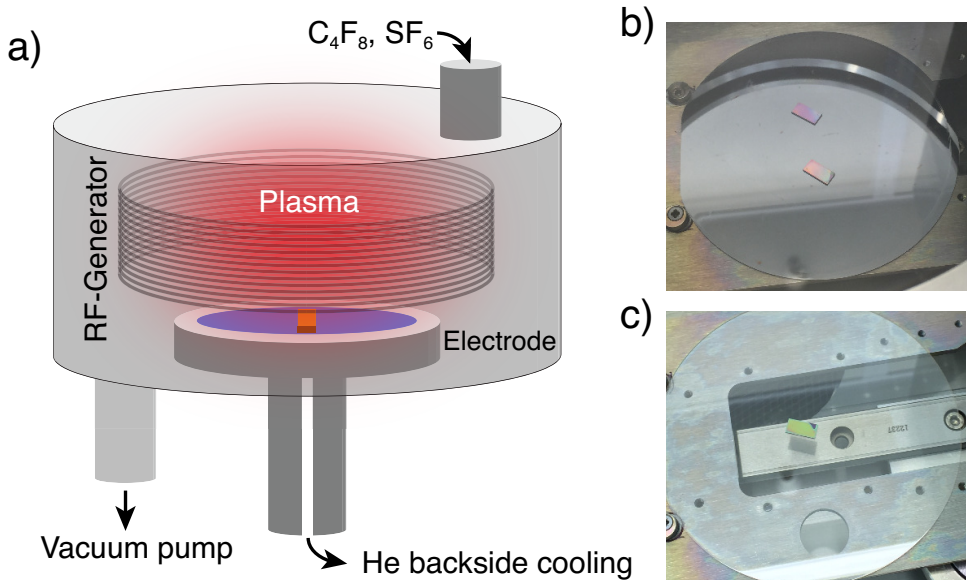

Figure 3.6: **Mechanism of plasma etch** (a) A schematic of an inductively coupled plasma reactive ion etching is displayed. After generating a plasma with reactive gases (C_4F_8 and SF_6) using an inductive coil, a bias created from the coil and the electrode bombards the chip with ions to etch away any exposed silicon materials on a chip. A recipe used for plasma etching is unique to each Inductively coupled plasma reactive-ion etch (ICP-RIE) system, where this recipe was fully optimized at NRC-NANO cleanroom. (b) Initially I have used a default silicon handler wafer to mount the chip with a dab of silicone grease, however, after repeated use of silicon, there is a risk of wafer breaking inside the chamber while loading and unloading mechanically. (c) Soon I have replaced the silicon-handle to a sapphire wafer to avoid repeated etches on a silicon wafer. The sapphire wafer is chemically resilient against silicon-etch and increases the etch-rate.

resonators, as shown in Fig. 3.5cd. After drying the chip with dry nitrogen, the lithography step is complete.

3.2.2.6 Plasma etch

We now turn from a discussion of lithographic techniques to a description of dry-etch processes, which is a crucial step to transfer the pattern from e-beam resist to the device layer. Reactive ion etching (RIE) is the most common form of plasma etching, allowing the use of both reactive (chlorine-based or fluorine-based) and non-reacitve gases (Ar or He). A plasma is formed when a sufficiently large DC or RF voltage is applied to electrodes, which energize electrons that ionize gas molecules at low-pressure. Through inductive coupling between the RF antenna and the plasma; the chip is placed on one electrode, connected to a separate RF

power source, creates a DC bias and attracts ions to the exposed chip. Both reactive and non-reactive gas cause sputter damage, ablating material from the sample. At low pressures, this can yield highly anisotropic results with very vertical sidewalls due to a higher rate of ion impact on exposed surfaces than the vertical walls.

The chemical process that occurs in reactive ion etching is quite complex, with a diverse short-lived intermediate species created when the process gas reacts with the substrate [84]. A full dedicated research of the various reaction sequences are needed; however, a selective number of gas chemistries have been developed due to the advancement in semiconductor industry. As mentioned previously, reactive gas is alkaline-based (fluorine, chlorine, and bromine); where a fluorine-based etch were optimized for Si-etch. An example of fluorinated gases are SF_6 and C_4F_8, where free fluorine ions are generated in the plasma through the reduction process in the plasma. The free fluorine ions then react with the silicon in the active layer, forming a volatile compound SiF_4,

$$\mathrm{Si} + 4\mathrm{F} \rightarrow \mathrm{SiF}_4. \tag{3.3}$$

Many dry etch recipes are based on C_4F_8 and SF_6, however etch rates and specific recipes are highly dependent on each system. To name a few parameters for dry-etch, there are operating power, pressure, temperature, bias voltage, gas flow-rate, and the choice of material for mounting the chip. These are inter-related parameters from one system to another and is a matter of trial and error. In general, lower pressures and higher plasma voltages yield more anisotropic results. Some gas mixtures, such as the carbon-based C_4F_8, deposit thin inert films on the structure sidewall such that the protection yields more anisotropic results. Oxygen may also be added to increase the etch rate, but for a thin layer of single-crystal silicon, it is not generally needed. Specific parameters used for the etching process at NRC-NANO Oxford Instruments PlasmaLab System 100 are shown in table 3.2.

Initially, I have used blank silicon wafers to condition the chamber and to process the chip, where the wafer was thinning down significantly on repeated operations. I have replaced the handle wafer to a sapphire wafer to be resistant against silicon plasma, where the full etch time changed from 42 seconds to 30 seconds by changing the mounted substrate. Note that a small amount of silicone grease was used to mount the SOI chips to the sapphire wafer. A ZEP520a e-beam resist is robust against the RIE recipe with good etch-selectivity of $\sim$1.2 as mentioned previously.

Process	O_2 cleaning	Si mixed etch (conditioning)
Forward ICP power (W)	2000	3500
RF power (W)	100	25
DC Bias (V)	450	100
Pressure (mTorr)	7	10
C_4F_8 flow rate (sccm)	—	12
SF_6 flow rate (sccm)	—	16
O_2 flow rate (sccm)	100	—
Substrate temperature (°C)	20	15
Processing time (min:sec)	20:00	00:30 (10:00)

Table 3.2: A table showing the parameters of silicon etch for SOI devices. Prior to Si-etch, an O_2 plasma is required to ensure a clean chamber. A conditioning step of a blank wafer is required for a reproducible etch, where the DC-bias is recorded in a log-book. Although the DC-bias stays near 100 V, it fluctuates over time depending on the chamber conditions — which affects the etch-rate. For a near 100 V bias, mounted on a silicon wafer, 30 seconds was enough for a complete etch of silicon using a sapphire substrate.

3.2.2.7 Post-release

Once the device is fabricated including a small gap between the resonators, a common problem in suspending the structure via a wet etch, HF or BOE, is the stiction in the drying step. When the sample is removed from the BOE solution, the drying process can destroy delicate mechanical structures due to large surface tension exerted on the structure. One technique that is popular in MEMS community, is the use of liquid carbon dioxide (LCO_2), which is a good solvent for IPA. Furthermore, it can be easily pressurized and heated to evade the critical point of liquid-vapour phase. This allows drying a sample without exposing the delicate structures to the direct transition from liquid-vapour interface — at which the surface tension is ignored. There are number of commercial systems built for critical-point drying, where I used three purging cycles to replace IPA to LCO_2. Another issue with wet-etch using HF and BOE is that these solutions also etch many metals, including most magnetic materials. There exist an alternative method to circumvent the metal-etch by etching the buried oxide layer followed by an e-beam lithography to a lift-off process without drying [85]; however, this method did not yield many devices per chip due to small gaps. A more practical approach is to use VHF to suspend structures. A final step of vapour etch can be done to bypass the stiction while the magnetic material is retained. Details on the VHF process will be included in Chapter 5 and 6. For the device in Chapter 4, the VHF

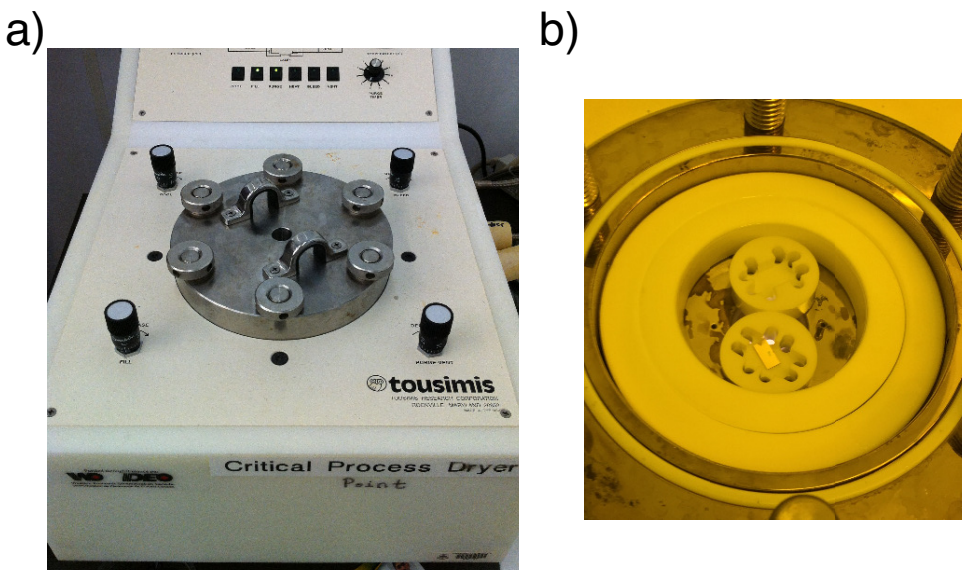

Figure 3.7: **Critical point drier** (a) A picture of the critical-point drier, used to avoid the stiction problem from surface tension of liquids. It replaces the solvent to liquid CO_2 where heat and pressure is applied to bypass the phase transition from liquid to vapour. (b) Inside the equipment, pieces of teflon rings are added to minimize the volume for the purging process from IPA to LCO_2. When the chip holder was placed in the middle, the chip would sometimes flip over due to currents in the fluid during multiple purging process.Having two chip holders rigidly placed, I can avoid the issue of the chip flipping over completely. However, there are sometimes contaminations after the CPD process.

equipment was not available at the time of fabrication, so I used the critical-point drier after the wet-etch, as seen in Fig. 3.7, which sometimes introduced contaminants after the process. Between the two methods, I prefer the VHF method over the critical point drier, but note that polymer resist is transparent to VHF, and therefore masking is not possible.

3.2.2.8 Fabrication summary

So far, I have covered the core fabrication process from the individual chip to post-released optomechanical structures. Further fabrication details tailored to each project will be addressed in respective chapters of 4, 5, and 6. These mainly include the use of lift-off process of magnetic materials and the implementation of VHF to etch the buried oxide layer while safeguarding deposited materials. Other non-thesis-related fabrication is mentioned in the appendix.

§ 3.3 Characterization

After a successful microscope inspection of the finished device, the chip is rushed into the vacuum chamber to minimize contamination and oxidation. Inside the chamber, optomechanical properties can be characterized in both optical and mechanical spectrum. Here experimental details regarding the dimpled microfibres fabrication, custom-made vacuum chamber, and examples of the optical and mechanical properties will be demonstrated at room temperature.

3.3.1 Dimpled microfibre

Tapered fibres are efficient, and require less on-chip space, than grating couplers or end-coupling, while free-space coupling is inconsistent with on-chip devices [87; 88]. Moulding a dimple on the tapered fibre can provide a maneuverable probe, allowing selective coupling to on-chip optomechanical devices [89] while having excellent efficiency ($\sim$ 80%), or minimum insertion loss, due to direct coupling of evanescent fields to optical resonators. The fabrication of tapered fibre is similar to a commercial one, where a commercial optical fibre (125 μm in diameter) is tapered adiabatically under heat until a single mode is supported for telecom wavelengths ($\sim$ 1 μm).

In detail, the first step is to prepare a optical fibre (SMF-28) of one meter in length, where both ends are stripped and cleaved for mechanical splices. The middle region is also stripped for tapering process ($\sim$ 1 cm). All cladding-stripped regions must be cleaned thoroughly using acetone, isopropyl alcohol (IPA), and methanol prior to mechanical spicing and clamping. The index-matching gel aids the mechanical splicing process until a good transmission is obtained through the fibre. The efficiency in tapering process is highly dependant on the straightness during the pull, hence any torque applied from misaligned setup will spoil the end result. This crucial alignment is done using a microscope viewing the top and the front ensuring a straight profile. A quick test can be done when the fibre softens (glowing white) by touching the side of the fibre with the hydrogen flame. If any bending occurs, while heated, careful alignment must be done on the clamp height and the clamp position to ensure levelling. Also, pre-heating for 10 seconds without pulling is a great way to confirm cleanliness prior to pulling. A hydrogen-fueled torch should have a pressure of $\sim$ 5 psi and the flame height should be about $\sim$1 cm. Adjusting the height of the torch such that the stripped region is centred vertically allows side-touching, confirmed by a small glow in a dark room, and the fibre is ready for pulling. The pull speed is typically $\sim$40 μm/s while the torch was periodically approached towards the fibre-taper in a small 10 μm

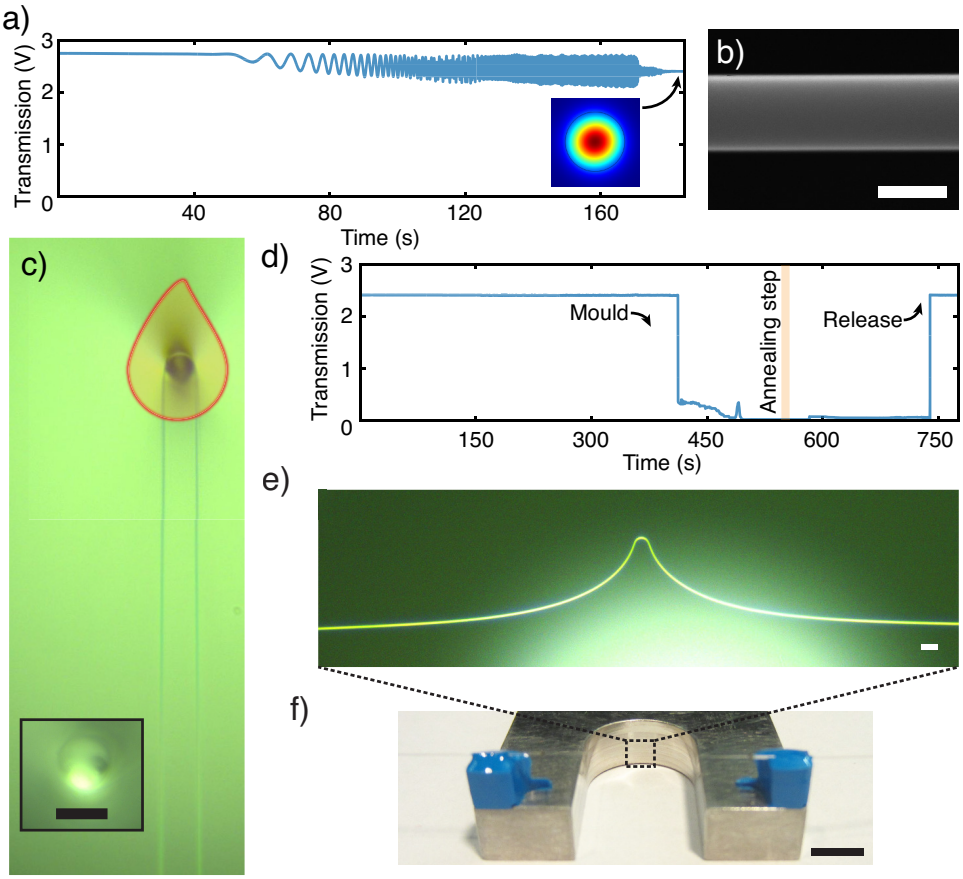

Figure 3.8: **Dimpled microfibre fabrication** (a) When a 125 μm diameter optical fibre is heated and stretched simultaneously, the optical transmission oscillates until it reaches a single mode at end, where the optical simulation profile shown on the inset [86]. (b) A SEM of the diameter in the tapered region, where the smallest diameter shows 1 μm, same as the scalebar. (c) After obtaining a nice tapered fibre, the $\sim$1 μm diameter fibre is wrapped around another fibre-mould (diameter of $\sim$ 65 μm) by manipulating the translation stages, as seen in the picture. Then a quick annealing step in the red region using a hydrogen torch shapes the dimple in the tapered region. The inset scale bar is 125 μm (d) Upon release of the tapered fibre waveguide to the mould, the optical transmission during the dimpled process, including the mould, annealing, and release step, shows negligible optical transmission loss: the fibre is clean and the curvature still holds the total internal reflection in the fibre core. (e) An optical image of the dimpled microfibre is shown with a scale bar of 5 mm. Using a low-temperature compatible epoxy, the dimpled tapered fibre is mounted on a fibre-holder as shown in photograph (f).

increments ($\sim$ 50 μm in total distance), to compensate the thinning. An optical profile, similar to Fig. 3.8a, should be seen where the tapering process stops when the oscillation

ceases. Here an efficiency of 83% was achieved for a $\sim$ 2 cm tapered region (Fig. 3.8). A general pull time is between 120 s to 150 s and if the final transmission is less than 50%, which is often due to the misalignment, the tapering process starts over.

After acquiring a tapered microfibre, the stage is in a microscope mode, mounted perpendicular to the microfibre, to view both the mould, a circular image with 125 μm in diameter, and a tapered fibre. Here the mould is cleaned thoroughly with acetone, IPA, and methanol before mounting it with a tape. An additional step is to apply a thin layer of graphite (Tube-O-Lube, SLIP plate) on the mould to prevent sticking with the tapered fibre. The graphite generally burns off with the hydrogen flame but excess of graphite should be avoided because particles may still remain in the tapered fibre which deteriorates optical transmission. After applying the graphite use the kim-wipe, or air gun, to gently brush off the excess graphite.

The fibre-clamps are retracted about 10 μm to pinpoint the thinnest region of the tapered fibre, which bends upwards, and the mould is centred to this location. While raising the mould to touch the tapered fibre, the clamps are retracted simultaneously to maintain tension of the fibre at all times to wrap the tapered fibre tightly around the mould. After a mould configuration, as seen in Fig. 3.8c, the torch stub is changed to create a small flame. Handling the torch upside down, a gentle heat is applied to the mould (for one second). A reverse process of lowering the mould, while tensioned, was performed until the mould is ready for release. Using a hydrogen torch, without ignition, a gentle flow of hydrogen breeze can release the tapered fibre from the mould. This part holds the key to a successful dimpled microfibre, where patience is often required during this step. With practice, the use of graphite can be omitted and full transmission was recovered (Fig. 3.8d).

After the dimple is made, as shown in Fig. 3.8e, a custom machined fibre fork is held upside down for the gluing procedure. Here Kapton tape is often used to provide additional levelling such that the glue on each side touches the fibre simultaneously. If the glue is applied on one side first, an uneven contact destroys the dimple by undesired one-sided tensioning. A wooden applicator is used to mix the two components of a 5-minute epoxy (Devcon 5 Minute® epoxy gel) and to apply it on the mount. At first, a small droplet of epoxy was added in the inner corners of the fork to hold the dimple in place with desired tension. After waiting about 20 minutes, until fully hardened, a new mixture of the epoxy can be fully applied to the rest of the area to hold the fibre securely. One important restriction is the epoxy height, which must not be higher than the dimple itself. Otherwise, the glue often touches the chip rather than the dimple itself and therefore the epoxy should be flattened using

the wooden applicator. Note that for low-temperature applications, a cryogenic-compatible epoxy (Loctite bipax 2151) must be used as seen in Fig. 3.8f.

3.3.2 Room temperature fiber-coupling chamber

Both the dimpled microfibre and the fabricated sample were installed in a custom-made coupling chamber. The vacuum chamber, illustrated in Fig. 3.9a, is capable of reaching down to 10^{-5} Torr and has a glass window on the top to allow imaging of the chip through a microscope. The vacuum is important to torque sensing, as the air damping is significant to mechanical quality factor at MHz frequencies. There are a total of six ports at the base of the vacuum chamber: two ports for pumping and venting, two ports for electrical leads to control nano-positioning stages underneath the chip, one electrical port for applying ac magnetic fields, and one port for fibre-optic feedthroughs for input/output. All electrical feedthroughs are hermetically sealed and the fibre feedthroughs are sealed by a vacuum compatible epoxy (Torr Seal®). Every time a new dimpled microfibre is fabricated, and mounted on a stationary aluminium holder, the ends of the fibre are fusion spliced to the fibres inside the chamber with little loss (0.01 dB). The excess of fibres are fixed with vacuum-compatible Kapton tape.

The vacuum chamber is mounted on a floating optical table to minimize all mechanical vibrations as the optomechanical detection is sensitive. The apparatus outside the chamber is shown in Fig. 3.9 where the laser goes through a series of attenuator, fibre polarization controller (FPC), and finally to the photodetector. While tuned-to-slope, the mechanics modulates the transmission where I can obtain the mechanical spectrum as seen in Fig. 3.9b. Here a thermomechanical calibration is applied to obtain displacement (7 fm/$\sqrt{\text{Hz}}$) and torque sensitivity (0.8 zNm/$\sqrt{\text{Hz}}$).

3.3.3 Low temperature apparatus

A large portion of my Ph.D. work dealt with cooling a torque sensor down to mK temperatures, which came with its unique challenges and difficulties. It may seem straight-forward to take the room temperature apparatus and place them on a base-plate of a dilution refrigerator; however thermal conduction, imaging system, and thermal contraction have to be considered and re-engineered for successful torque measurements at low temperatures. Here I acknowledge early team efforts of measuring silica bottle resonators with tapered fibre [90; 91]. From this foundation of microscope capability at low temperatures, I have extended this apparatus to adapt on-chip devices where the best torque sensitivity was

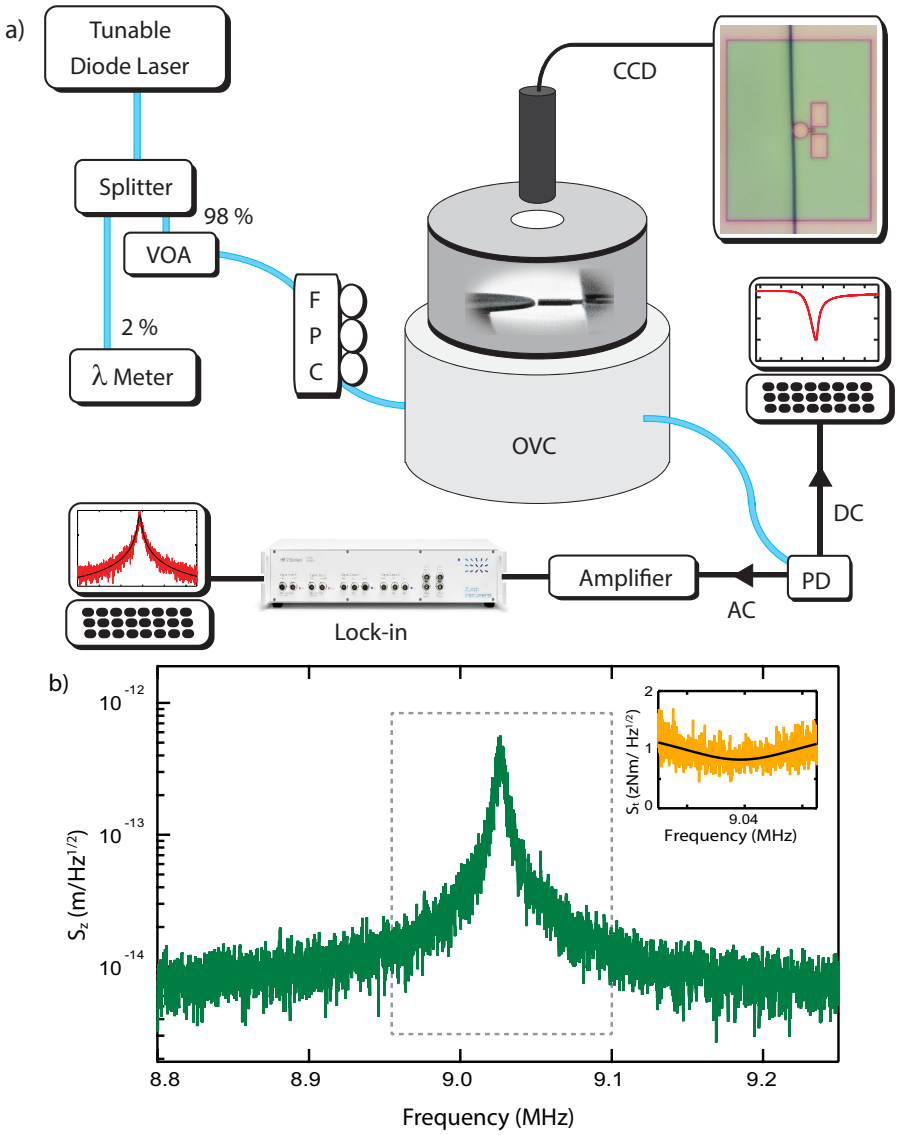

Figure 3.9: **Dimpled microfibre coupling apparatus** (a) The nanofabricated optomechanical chip is placed on the three-axes of nano-positioners and highly-efficient dimpled tapered fibre are housed in a moderate vacuum chamber, capable of reaching $\sim 10^{-5}$ Torr. The apparatus shows the transduction of a mechanical spectrum when the wavelength is tuned-to-slope (the laser goes through splitter, variable optical attenuator (VOA), fibre polarization controller (FPC), and photodiode (PD). (b) The displacement power spectral density (S_z) of the torsional optomechanical device in Ref. [48] shows a noise-floor, or minimum detectable signal, of 7 fm/$\sqrt{\text{Hz}}$. The inset shows the optimal torque sensitivity of 0.8 zNm/$\sqrt{\text{Hz}}$ at the mechanical resonance frequency.

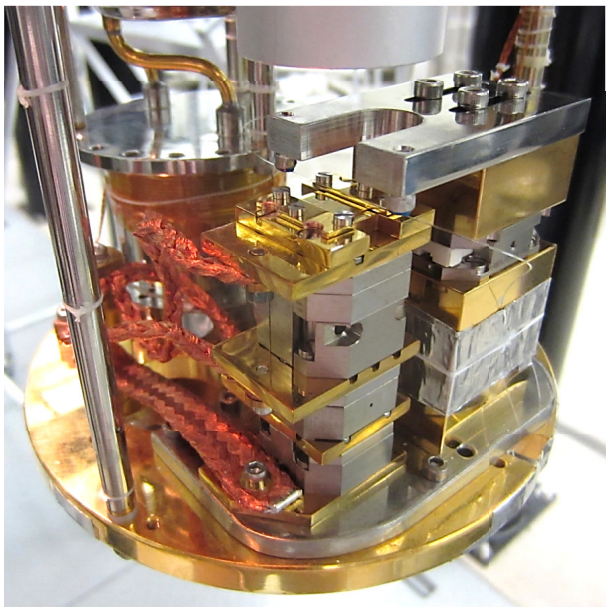

Figure 3.10: **Low temperature apparatus** A photograph of the optomechanical apparatus installed on a baseplate of the dilution refrigerator. The core components are similar to the room temperature apparatus: imaging system, dimpled tapered fibre, and nano-positioning stages.

achieved. Described in this section is the principle of a dilution fridge, which leads to our next discussion of low-temperature torque sensing in the next chapter.

3.3.3.1 Background

Kamerlingh Onnes, in the early 1900's, reached temperatures below 1 K using series of pumps to manually reduce the vapour pressure of liquid helium. By accessing this temperature range, anomalies of helium density around 2.2 K (superfluidity) and superconductivity of mercury were discovered [92; 93]. Because ^{3}He was unavailable at the time, the only way to lower the temperature further was the adiabatic demagnetization of magnetic moments in paramagnetic salts [94; 95]. Later, improvements in magnetic field strengths and precooling methods of ^{3}He and ^{4}He mixtures, allowed nuclear spins to be also used for refrigeration, where temperatures near 10 μK was achieved [96]. Further discussion of adiabatic demagnetization will be mentioned in the appendix as an outlook. With more ^{3}He available for commercial usage, many low-temperature refrigerators can hold continuous operation down

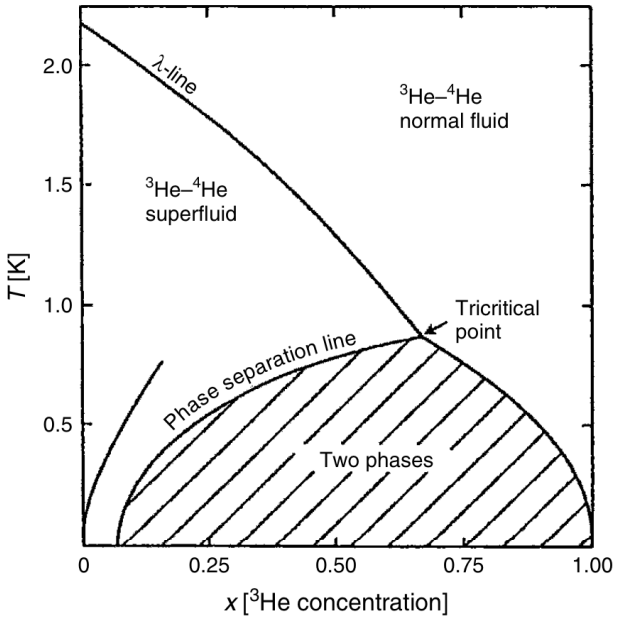

Figure 3.11: **Phase diagram of liquid mixtures of ^{3}He and ^{4}He** The phase diagram of the ^{3}He and ^{4}He mixtures, where there are three regions: superfluid phase, normal phase, and the forbidden phase (dashed), where the phase separation of the ^{3}He-rich (pure) and the ^{3}He-poor ($\sim$6.5% diluted) phase occurs. Even at $T = 0$, phase separation occurs for a wide range of ^{3}He concentrations (from Ref. [98]).

to mK temperatures, such as a dilution refrigerator, and a closed-system pulse tube cryocoolers. A pulse-tube system, which uses dynamic compression and expansion of ^{3}He gas, can cool down to sub-Kelvin temperatures without the use of cryogenic liquids. However, this system is mechanically noisy, where efforts to reduce the vibrations have been made by attaching damped-springs to the MFRM experiment [97]. In general, cryogen-free refrigerator is not compatible with vibration sensitive optomechanical measurements. A commercial dilution refrigerator, where the entire fridge is housed on an extruded floating optical table, situated on a separate foundation from the rest of the building, is used to remove all mechanical noise of the system, while taking advantage of the base temperature of 9 mK. In the next few sections, I will discuss some basic aspects of different cooling stages in a dilution refrigerator, prior to the experimental results in the next chapter.

3.3.3.2 Cooling principle of a dilution refrigerator

The cooling principle of a dilution refrigerator is similar to evaporative cooling except that mixtures of ^{3}He/^{4}He was used instead of pure ^{4}He. When the mixture is cooled below $\sim$

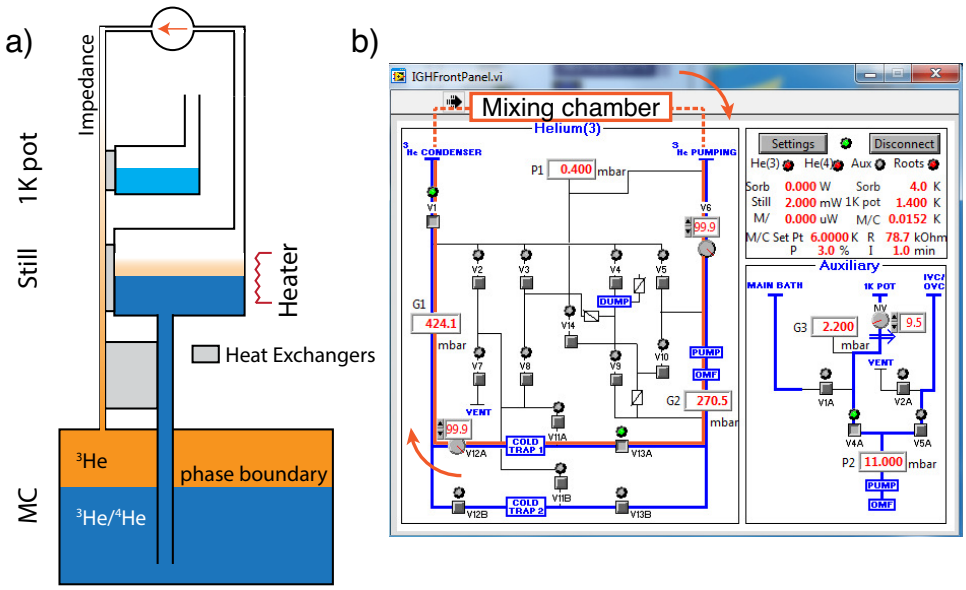

Figure 3.12: **Operation of a dilution refrigerator** (a) A schematic of the operating principle behind a dilution refrigerator. Inside the IVC, the room-temperature gas is pre-cooled to the 1 K pot. After a succession of thermally-linked heat exchangers, the ^{3}He gas condenses to a pure liquid, which is fed to the mixing chamber. From the mixing chamber, the ^{3}He atoms in a diluted phase is pumped away from the still line creating a continuous closed-cycle. As the circulation continues, balanced by the impedance line, the base temperature of 9 mK was reached at the baseplate (unloaded). (b) The control panel of the ^{3}He circulation outside the IVC. The ^{3}He atoms are mechanically pumped from the still line and cycles through a cold trap, which it is fed back to the IVC.

870 mK, it goes under spontaneous phase separation of the ^{3}He-rich phase (near 100% ^{3}He) and the dilute phase (6.5% of ^{3}He in ^{4}He) as confirmed from various experiments [99]-[101]. The ^{3}He atoms in the ^{3}He-rich phase have lower entropy than the dilute phase, where it absorbs heat from its environment when the ^{3}He atoms transfers from the ^{3}He-rich phase to the dilute phase. By an interplay of zero-point energy and binding energy, even at $T = 0$, there is always a finite solubility of ^{3}He in liquid ^{4}He, where this process can cool down to sub-Kelvin temperatures. The transfer of ^{3}He atoms from rich to dilute phase is initiated by a strong mechanical pump to evaporate ^{3}He atoms in the dilute phase, where the ^{3}He atoms are replenished into the dilute phase to maintain its 6.5% concentration. For a continuous operation of this cooling mechanism, one has to a supply evaporated ^{3}He atoms recondensed into the ^{3}He-rich phase, completing the cycle. Hence the circulation of ^{3}He, outside the mixing chamber, requires multiple heat-exchangers for re-liquification of evaporated ^{3}He from the still.

The circulation of ^{3}He in a closed-loop system is shown in Fig. 3.12a. Beginning at the still, heat is applied to increase the efficiency of pumping. From the mixture, ^{3}He is predominantly pumped due to higher vapour pressure and goes through a cold trap outside the dewar to purify the ^{3}He gas. The room temperature ^{3}He gas enters the inner vacuum chamber (IVC), precooled at the 1K pot. A high impedance flow maintains a high pressure such that ^{3}He condenses efficiently. After passing through multiple heat exchangers, liquid ^{3}He enters the return line at the mixing chamber — where the cooling occurs as the ^{3}He atoms cross the phase boundary to the dilute phase.

3.3.3.3 Components of the fridge

Over the years, dilution refrigerators have been re-engineered due to widespread commercial and acadamic usages, especially with the modern engineering of quantum computers. Described here are the standard parts of a dilution fridge, going from the top to bottom as seen in Fig. 3.13b.

1 K pot

The 1 K system is a copper pot containing a small volume of liquid ^{4}He, where a pump is connected to cool near 1.4 K by evaporative cooling. There are feed-lines from the ^{4}He dewar to supply the liquid, with a slightly-opened needle-valve to the pump, to regulate the temperature in the 1 K pot. The main purpose of the 1 K pot is to provide a first heat link for the condensation of incoming ^{3}He from the dilution circuit.

Still

The still serves the similar purpose as the 1 K pot, except that it operates at a lower temperature (typically 500-700 mK). The distillation process is performed in the still, where liquid ^{3}He is evaporated by a mechanical pump and a heater to control the flow. There are also heat exchangers, placed inside the still, to cool the incoming ^{3}He atoms from the 1 K pot to the mixing chamber.

Heat exchangers

After the still, additional heat exchangers are used to further cool the liquid prior to the mixing chamber. To overcome a large thermal resistance, known as the Kapitza resistance (or acoustic impedance in the interface of helium and metals), it is required to have large surface areas [102]. Hence, step heat exchangers are installed in addition to continuous heat exchangers. Continuous exchangers use a helical structure inside a helical design, to increase the surface area. The step exchangers, on the other hand, have a copper block with a cylindrical hole in it, where sintered silver powder is filled to provide a large surface area. Multiple step exchangers can be included to have a strong thermal link between the

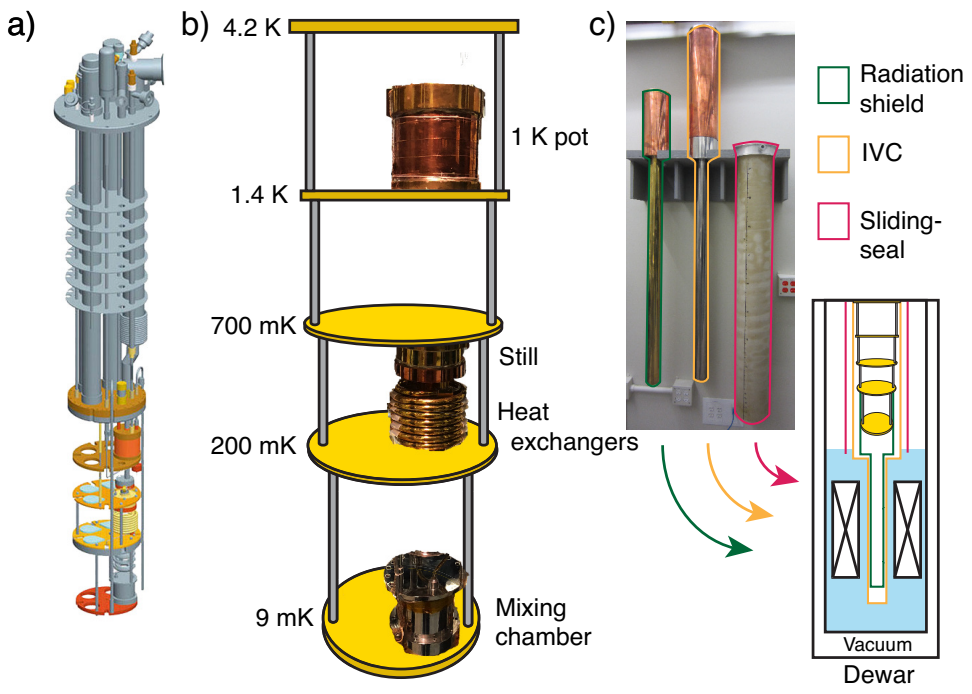

Figure 3.13: **Layout of the fridge** (a) A commercial rendering of our Oxford Kelvinox400HA system where the bottom half is sealed by IVC and the whole system is covered by sliding-seal and dewar. (b) Cropped pictures of the core dilution parts overlayed with a rendered flanges to simplify the layout. The top flange is 4.2 K linked to the ^{4}He dewar, followed by 1.4 K flange based on the 1 K pot, 1.0 K flange from the still, 200 mK flange from heat exchangers, and 7 mK at the base plate where the mixing chamber resides. (c) A photograph of the radiation shield, IVC, and the sliding seal is shown from left to right and is illustrated below where the radiation shield and the IVC creates a thermal isolation to the bath except at the top flange of b). The sliding seal is in place to prevent condensation of air while raising and lowering a cold dewar.

incoming and outgoing flow outside the mixing chamber. With well-designed exchangers, we reached 9 mK as a base temperature of an unloaded fridge.

Mixing chamber

The heart of the dilution fridge is the mixing chamber: a pot, made similar to the 1K pot and the still, contains two phases of the mixture. When the two phases separate, the heavy ^{4}He-rich, sink below the ^{3}He-rich phase. The capillary connected the ^{3}He-rich portion, called the 'still line', is used to extract the ^{3}He through a mechanical pump. The ^{3}He is cooled via heat exchangers, then recondensed back through the capillary, called 'condenser line', connected to the top of the pot.

The crucial part of this closed-loop system is the efficiency of pre-cooling of the condenser line to the still line. Despite the best efforts to achieve this by heat exchangers, there are heat loads to the mixing chamber. Assuming that the heat load comes from the incoming ^{3}He, the cooling power, $\dot{Q}_{\rm mc}$, can be balanced as,

$$\dot{Q}_{\rm mc} = \dot{N}(95T_{\rm mc}^2 - 11T_{\rm ex}^2), \tag{3.4}$$

where $\dot{N}$, is the ^{3}He circulation rate, $T_{\rm ex}$ is the temperature right before entering the mixing chamber, and $T_{\rm mc}$ is the final temperature at the mixing chamber [98]. Note that radiation losses and vibration losses are neglected in the expression. Based on Eqn. 3.4, with a fixed circulation rate, best cooling power is achieved by installing continuous and step efficient heat exchangers as we have discussed before. In our system, we have total of three step exchangers to reach base temperature of 9 mK.

3.3.3.4 Thermometry

Temperature is a thermodynamic property that can be measured at low temperatures with a large number of thermometers, classified in two categories: primary and secondary thermometers. Primary thermometers measure temperature without any prior calibration, where it relies on independent and reproducible measurements defined by fundamental laws of physics. In contrast, secondary thermometers require calibration to other thermometers, typically primary thermometers. Rather than listing all the possible thermometers used at low temperatures, I will enumerate ones I have used in my experiments: nuclear orientation therometer and resistance thermometers.

Nuclear orientation thermometer

Our primary thermometer is the nuclear orientation thermometer, which counts the statistics of the γ-ray emission, a quanta of decay in a radioactive nuclei (^{60}Co). The host material of a ferromagnetic needle creates a strong magnetic field to split degenerate levels of the nuclei. By measuring the anisotropy of the γ-ray emission along the needle-axis direction, the thermal occupation of sublevels can be inferred [103]. Fig. 3.14 depicts the method using the count rate of γ emission as a function of temperature. The nuclear orientation thermometer is highly accurate in the temperature range from 5 mK to 50 mK; however, the measurement is slow due to count-statistics. A constant background of radioactive decay will contribute to a small part of the heat load. The detector is placed outside the dewar, which needs to be properly aligned and mounted prior to the mK temperature operation.

Resistance thermometers

The calibration of all secondary thermometers must ultimately originate from a primary thermometer. After successful calibration, secondary thermometers are often easier and

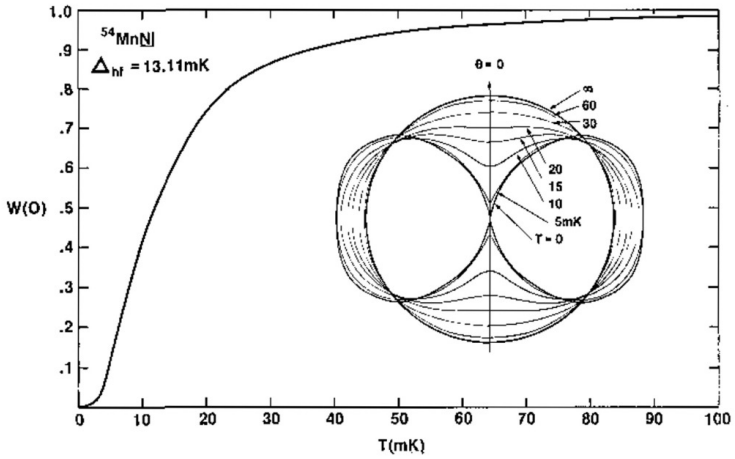

Figure 3.14: **Nuclear orientation thermometer** The inset shows an illustration of the γ-ray spectrum as a function of temperature: at high temperature, $T = \infty$, the spectrum is isotropic, where at $T = 5$ mK, the emission-rate along the magnetized axis ($\theta = 0$) gradually decreases. This is shown by the data, where the vertical axis is the normalized γ-emission count-rates of a single crystal ^{60}Co along $\theta = 0$ axis ($W(0)$) and the horizontal axis varies in mK temperatures (reproduced from Ref. [103]). From the large slope, or large sensitivity, below ~ 30 mK, this type of primary thermometer is used in our dilution refrigerator.

quicker to use than primary thermometers. In most low-temperature laboratories, the widely used thermometer is based on the temperature dependence of the electrical resistance of conducting materials: metals, semiconductors, and carbon resistors. These are commercially available and inexpensive, depending on the temperature range. We have used a conductive compound RuO_2 resistor to measure temperature range below 50 mK, which becomes less accurate below 20 mK. The advantage of these thermometers is their reproducibility and quick measurements. The primary and the secondary thermometers are used complimentary to observe the absolute temperature for long periods and to detect abrupt changes in temperatures during measurements.

3.3.3.5 Operating maintenance

While running the dilution refrigerator at full capacity, there are two closed-loop systems: ^{3}He for the dilution stage and ^{4}He for the dewar supply. As previously mentioned, ^{3}He circulation requires a cold trap outside the dewar to clean the ^{3}He flow prior to condensation. This maintenance is done by topping up the cold trap liquid nitrogen as frequently as possible, where failure to do so may cause blockage in the impedance capillary to the mixing chamber. For the ^{4}He cycle, the 1 K pot extracts liquid ^{4}He from the dewar where a manual

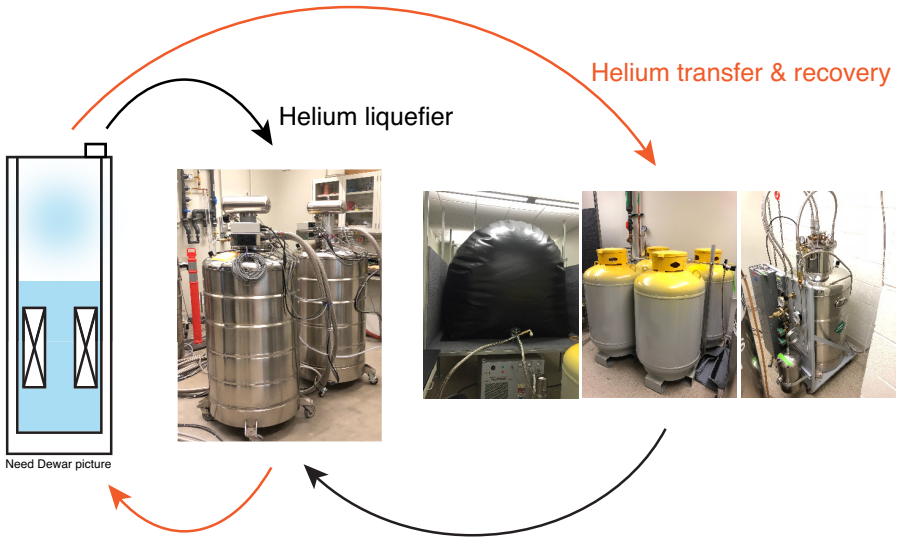

Figure 3.15: **^{4}He recovery system** During normal operation, noted by black arrows, evaporated ^{4}He atoms from the dewar and 1 K pot are fed directly to the liquefier by a compressor. When the liquid is running low in the dewar, where the ^{4}He level is near the bottom of the 1 K pot feedline, a manual ^{4}He transfer is conducted to top-up the helium level from the liquefier using a transfer stick and pressurized ^{4}He gas, as indicated by the bottom orange arrow. During the transfer process, a large volume of ^{4}He is generated, which is captured first in a black recovery bag located at a separate room, as noted by top orange arrow. To accommodate all the helium, a compressor takes ^{4}He into pressurized yellow cylinders for storage. Afterwhich, ^{4}He atoms are purified in a cold trap and is pressurized to the liquefier in our lab. Based on this efficient recovery system, experiments can be prolonged to years of operation as long as the weekly ^{4}He transfers are met.

helium transfer is required to maintain a certain helium level above the pot feedline. Here, we have an efficient helium recovery system: the evaporated ^{4}He gas is collected in a bag outside the lab, pressurized and purified by a LN_2 coldtrap, and ends up in a liquifier where a manual transfer is done by a transfer tube. A summary is shown in Fig. 3.13, where the transfer routine is performed once per week. During the transfers, both coldtraps in the ^{3}He/^{4}He systems are filled.

3.3.3.6 Low temperature endoscope

An objective, to align the micron-size tapered fibre to the optical microdisk, is crucial for optomechanical coupling. At low temperatures, this is difficult due to thermal contraction of materials, where the alignment of the fibre and the disk cannot be done blindly. Hence, the first project on a commercial dilution refrigerator was to implement a low-temperature

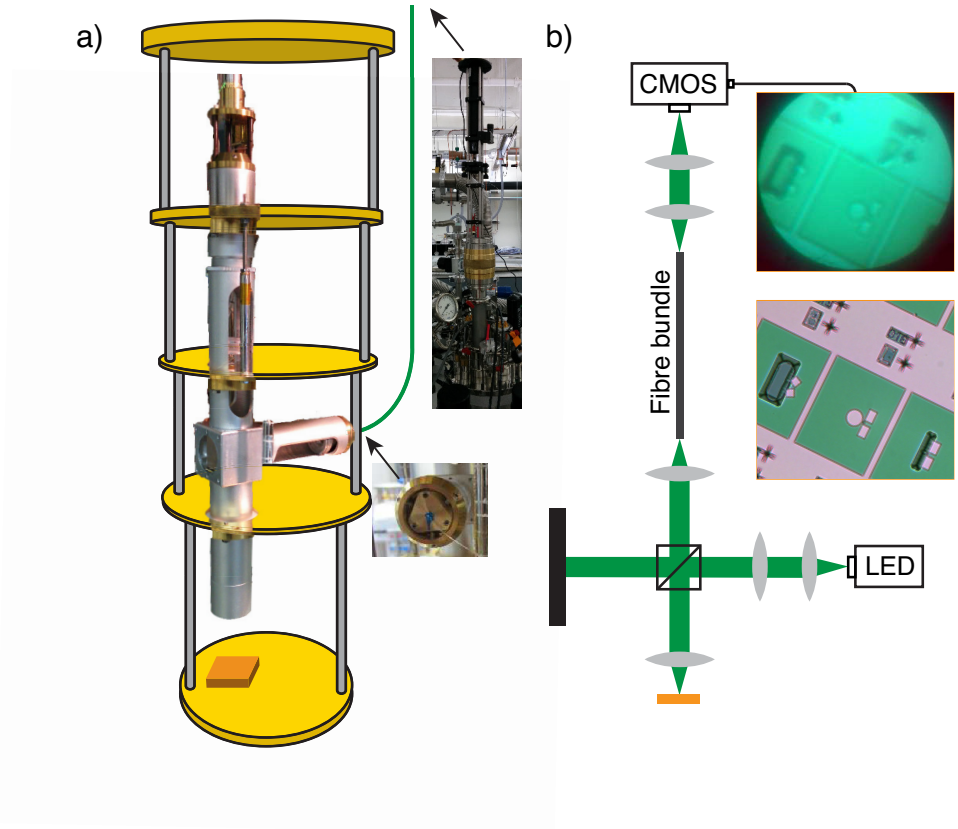

Figure 3.16: **Low temperature optical microscope** (a) From the same schematic, as seen in Fig. 3.12, the tonfa-shaped imaging system is overlayed in a photograph. Additional photographs of the top portion, including the camera, the 37,000 fibre-bundle, and the thimble system to translate the imaging system vertically is shown as well as the LED fibre feedthroughs on the bottom. (b) The imaging principle is shown here where the green LED is focused and collimated through the sample and is collected through a fibre-bundle toward a CMOS-based CCD camera. The image collected from this system is crisp and clear in comparison to an actual microscope image of the same chip.

compatible microscope. We have installed a fibre-bundle system, modelled after the Helsinki system, to collect light with a charged-coupled device (CCD) camera outside the fridge [90]. A light-emitting diode (LED) at 530 nm is chosen as an illumination source for better image contrast. Utilizing the space given from the commercial dilution parts, we successfully colliminated and focused the green LED source to the coherent 37,000 fibre-bundle system (Fujikura FIGH-40) to translate image from the chip on the baseplate to the CCD outside the fridge as 37,000 pixels, shown in Fig. 3.16a. When operating the fridge, the only knob allowed to manipulate is the image focus, where a thimble (Huntington VF-178-275) translates the

entire imaging apparatus vertically. An example of the image taken is shown in Fig. 3.16b. So far we have discussed the cooling mechanism of a dilution refrigerator with some initial work on the imaging system. Further discussions on incorporating on-chip optomechanics to a dilution refrigerator will be featured in the next chapter.

- Chapter 4 -

APPROACHING THE STANDARD QUANTUM LIMIT OF MECHANICAL TORQUE SENSING

What is essential is invisible to the eye.

- The Little Prince

This chapter highlights my research, where I reduced the torque sensitivity near the quantum level at low-temperatures. After covering the details of standard processes for on-chip fabrication, the custom-built optomechanical apparatus to detect torque at room temperature, and operating principles of a dilution refrigerator, we are now ready to embrace the combination of torsional optomechanics and low-temperature apparatus. This chapter is based on the publication in 2016, highlighting the first optomechanical torque sensor built at low-temperatures, accentuating the importance of low-temperature for torque sensitivity [48].

§ 4.1 Introduction

Cavity optomechanics allows measurement of extremely small mechanical vibrations via effective path length changes of an optical resonator, as epitomized by the extraordinary detection of the strain resulting from transient gravitational waves at LIGO [15]. Harnessing cavity optomechanics has enabled measurements of displacement (the basis for force and torque sensors) of on-chip mechanical devices [17; 104] at levels unimaginable by previous techniques. Here we focus on cavity optomechanics as a platform for measuring torque applied to a torsional spring. Classically, for a thermally-limited measurement, the minimum

resolvable mechanical torque spectral density is given by

$$S_\tau^{\mathrm{th}} = 4k_{\mathrm{B}}T\Gamma I, \tag{4.1}$$

where k_{B} is the Boltzmann constant, and T is the mode temperature. Minimization of the moment of inertia, I, and the mechanical damping, Γ, can therefore result in improved torque sensitivity at a given temperature. Yet, reducing the mechanical damping is notoriously challenging, and even with modern nanofabrication techniques — and cavity optomechanical detection of sub-optical wavelength structures — the moment of inertia can only be lowered so far. Here geometric optimization leads to the design previously shown in Fig. 3.2e, with a room temperature torque sensitivity of 0.5 zNm/$\sqrt{\mathrm{Hz}}$; a modest improvement over the 0.8 zNm/$\sqrt{\mathrm{Hz}}$ of previous incarnations of cavity optomechanical torque sensors (Fig. 3.2b [48], Fig. 3.1c [70]). Therefore further improvement demands lowering of the mechanical mode temperature.

Fortunately, on-chip optomechanical devices have been successfully integrated into cryogenic environments. Multiple architectures are now capable of cooling near the quantum ground state either directly through passive cooling [8; 105; 106], or in combination with optomechanical back-action cooling [24; 107]. Yet, as we demonstrate below, only passive cooling is compatible with reducing the thermal noise in an optomechanical torque sensor. Furthermore, while these architectures are well suited to tests of quantum mechanics and applications of quantum information processing, they are not well suited to integration with external systems one may wish to test. Hence our cavity optomechanical torque sensing platform is unique in that it enables straightforward integration with test samples and operates in a dilution refrigerator with near quantum-limited torque sensitivity.

4.1.1 Fundamental limits of torque sensitivity

The torque sensitivity involves three spectra in the quantum regime: the device's intrinsic angular displacement spectrum, $S_\theta^{\mathrm{qu}}(\Omega)$, the back-action and imprecision noise spectra associated with the measurement apparatus, $S_\theta^{\mathrm{ba}}(\Omega)$ and $S_\theta^{\mathrm{imp}}(\Omega)$ — where the total noise spectral density can be written as,

$$S_\theta(\Omega) = S_\theta^{\mathrm{qu}}(\Omega) + S_\theta^{\mathrm{ba}}(\Omega) + S_\theta^{\mathrm{imp}}(\Omega). \tag{4.2}$$

Here the intrinsic noise is generated from the combination of the thermal and quantum fluctuations of the mechanical element and the measurement apparatus. Going term by term, the intrinsic angular noise spectrum ($S_\theta^{\mathrm{qu}}(\Omega)$) can be expressed mathematically using the

(quantum) fluctuation-dissipation theorem [108] for the single-sided angular displacement as

$$S_\theta^{\mathrm{qu}}(\Omega) = 4\hbar\left(\langle n\rangle + 1/2\right)\mathrm{Im}\{\chi(\Omega)\} = 4\hbar\Omega\Gamma I\left(\langle n\rangle + 1/2\right)|\chi(\Omega)|^2. \tag{4.3}$$

Substituting the susceptibility, $S_\theta(\Omega) = |\chi(\Omega)|^2 S_\tau(\Omega)$, to Eqn. 4.3, we can identify the intrinsic quantum torque spectrum as $S_\tau^{\mathrm{qu}}(\Omega) = 4\hbar\Omega\Gamma I\left(\langle n\rangle + 1/2\right)$, where $\langle n\rangle$ is the phonon occupation of the torsional mode. For the case of thermal equilibrium with a bath at temperature T, the phonon occupation is given by the Bose-Einstein occupation factor $\langle n\rangle = \bar{n}_{\mathrm{th}} = (e^{\hbar\Omega/k_B T} - 1)^{-1}$. Note that we also have an addition of one-half to this thermal occupation corresponding to the ground state motion of the mechanical resonator. In the high-temperature limit, $\langle n\rangle \approx k_B T/\hbar\Omega \gg 1$, this ground state contribution can be neglected and $S_\tau^{\mathrm{qu}}(\Omega)$ reduces to the familiar classical white-noise torque spectrum of $S_\tau^{\mathrm{cl}} = 4k_B T\Gamma I$ [86].

Likewise, one can express the back-action angular noise spectrum as $S_\theta^{\mathrm{ba}}(\Omega) = |\chi(\Omega)|^2 S_\tau^{\mathrm{ba}}(\Omega)$, where we have now introduced a back-action torque noise spectrum, $S_\tau^{\mathrm{ba}}(\Omega)$. In general, this back-action torque spectrum, as well as the angular imprecision noise spectrum, $S_\theta^{\mathrm{imp}}(\Omega)$, will contain contributions from both classical technical noise and fundamental quantum noise, with the product of the two spectra obeying the Heisenberg uncertainty relation (for single-sided spectra) [108]-[110]

$$S_\tau^{\mathrm{ba}}(\Omega) S_\theta^{\mathrm{imp}}(\Omega) \geq \hbar^2. \tag{4.4}$$

Note that the equality in Eqn. 4.4 corresponds only to quantum-limited measurement noise.

We can now determine an equivalent torque noise spectrum from Eqn. 4.3 using the angular susceptibility of the system as

$$S_\tau(\Omega) = \frac{S_\theta(\Omega)}{|\chi(\Omega)|^2} = 4\hbar\Omega\Gamma I\left(\langle n\rangle + n_{\mathrm{imp}}(\Omega) + n_{\mathrm{ba}}(\Omega) + 1/2\right), \tag{4.5}$$

It is this torque noise spectrum that sets the minimum resolvable torque, and hence the sensitivity, of our system. In Eqn. 4.5, we have introduced the noise equivalent quanta due to measurement imprecision and back-action, $n_{\mathrm{imp}}(\Omega) = S_\theta^{\mathrm{imp}}(\Omega)/4\hbar\Omega\Gamma I|\chi(\Omega)|^2$ and $n_{\mathrm{ba}}(\Omega) = S_\theta^{\mathrm{ba}}(\Omega)/4\hbar\Omega\Gamma I|\chi(\Omega)|^2$, whose product can be found from Eqn. 4.4 to obey

$$n_{\mathrm{imp}}(\Omega) n_{\mathrm{ba}}(\Omega) \geq \frac{1}{16\Omega^2\Gamma^2 I^2|\chi(\Omega)|^2}, \tag{4.6}$$

with equality again corresponding to quantum-limited measurement noise. Note that at the mechanical resonance frequency, Eqn. 4.6 reduces to the familiar form $n_{\mathrm{imp}}(\Omega_{\mathrm{m}}) n_{\mathrm{ba}}(\Omega_{\mathrm{m}}) \geq$

1/16 [110].

For the minimum possible torque noise spectrum as allowed by quantum mechanics, we first look to minimize the added measurement noise ($S_\theta^{\rm imp}(\Omega) + S_\theta^{\rm ba}(\Omega)$) of our system. By taking equality in the Heisenberg uncertainty relation of Eqn. 4.4, we find the optimal measurement noise spectra of $S_\theta^{\rm imp}(\Omega) = S_\theta^{\rm ba}(\Omega) = \hbar|\chi(\Omega)|$, or equivalently, $S_\tau^{\rm ba}(\Omega) = \hbar/|\chi(\Omega)|$, corresponding to the so-called standard quantum limit (SQL) of continuous position measurement [108; 109]. Furthermore, by tuning to the mechanical resonance frequency, $|\chi(\Omega)|$ is maximized, thus minimizing the torque noise $S_\tau(\Omega)$ in Eqn. 4.5 with respect to frequency. Returning to our effective quanta notation, we find that $n_{\rm imp}(\Omega_{\rm m}) = n_{\rm ba}(\Omega_{\rm m}) = 1/4$ at the SQL, such that the minimized torque noise is found to be

$$S_\tau^{\rm SQL} = S_\tau^0(\langle n\rangle + 1), \tag{4.7}$$

where $S_\tau^0 = 4\hbar\Omega_{\rm m}\Gamma I$ is the fundamental torque noise spectrum associated with the continuous monitoring of a mechanical resonator in its quantum ground state at the SQL. It is this zero-point torque spectrum that sets the quantum limit for the minimum resolvable torque for a given device, half of which arises from the zero-point motion of the resonator, the other half from the Heisenberg-limited measurement noise at the SQL, whereas the limit at finite temperature will be given by the quantity in Eqn. 4.7.

4.1.2 Passive versus active cooling

As demonstrated by Eqn. 4.7, the torque sensitivity is improved as the average phonon occupancy of the device is reduced by passive cooling the device. However, one might think to use an active mode-damping method to reduce the phonon occupancy of the mechanical resonator and therefore its minimum resolvable torque. Unfortunately, in such a process the torque sensitivity generally decreases by the increase in the mechanical resonance's linewidth.

Consider the case of optomechanical back-action cooling (OBC), where photons trapped in an optical cavity impart a dynamical radiation pressure force on the mechanical resonator, increasing its intrinsic linewidth by an amount $\Gamma_{\rm OM}$, such that $\Gamma \to \Gamma + \Gamma_{\rm OM}$. In this example, the average phonon occupancy of the resonator becomes,

$$\langle n\rangle = \frac{\Gamma\bar{n}_{\rm th} + \Gamma_{\rm OM}\bar{n}_{\rm min}}{\Gamma + \Gamma_{\rm OM}}, \tag{4.8}$$

where $\bar{n}_{\mathrm{min}}$ is the minimum attainable average phonon occupancy using this method [111; 112], ($\bar{n}_{\mathrm{min}} = \kappa_{\mathrm{cav}}/4\Omega_{\mathrm{m}}$ for $\kappa_{\mathrm{cav}} \gg \Omega_{\mathrm{m}}$, whereas $\bar{n}_{\mathrm{min}} = \kappa_{\mathrm{cav}}^2/16\Omega_{\mathrm{m}}^2$ in the sideband resolved case of $\kappa_{\mathrm{cav}} \ll \Omega_{\mathrm{m}}$, with κ_{cav} being the linewidth of the optical cavity). Note that for $\Gamma_{\mathrm{OM}} = 0$ (*i.e.* no optomechanical damping), $\langle n \rangle = \bar{n}_{\mathrm{th}}$ and thermal equilibrium is restored.

Placing Eqn. 4.8 into Eqn. 4.7, we obtain the minimum resolvable torque spectrum associated with OBC as

$$\begin{aligned} S_\tau^{\mathrm{obc}} &= 4\hbar\Omega_{\mathrm{m}} I(\Gamma + \Gamma_{\mathrm{OM}}) \left(\frac{\Gamma \bar{n}_{\mathrm{th}} + \Gamma_{\mathrm{OM}} \bar{n}_{\mathrm{min}}}{\Gamma + \Gamma_{\mathrm{OM}}} + 1 \right) \\ &= 4\hbar\Omega_{\mathrm{m}} I(\Gamma \bar{n}_{\mathrm{th}} + \Gamma_{\mathrm{OM}} \bar{n}_{\mathrm{min}}) + 4\hbar\Omega_{\mathrm{m}} I(\Gamma + \Gamma_{\mathrm{OM}}) \\ &= 4\hbar\Omega_{\mathrm{m}} \Gamma I(\bar{n}_{\mathrm{th}} + 1) + 4\hbar\Omega_{\mathrm{m}} \Gamma_{\mathrm{OM}} I(\bar{n}_{\mathrm{min}} + 1) \\ &= S_\tau^{\mathrm{SQL}} + S_\tau^{\mathrm{OM}} \geq S_\tau^{\mathrm{SQL}}, \end{aligned} \tag{4.9}$$

where $S_\tau^{\mathrm{OM}} = 4\hbar\Omega_{\mathrm{m}}\Gamma_{\mathrm{OM}} I(\bar{n}_{\mathrm{min}} + 1)$ is the contribution to the minimum resolvable torque spectrum due to optomechanical back-action. Note that the inequality in the last line of Eqn. 4.9 arises due to the fact that $S_\tau^{\mathrm{OM}} \geq 0$ for optomechanical damping (where $\Gamma_{\mathrm{OM}} \geq 0$), with equality corresponding to $\Gamma_{\mathrm{OM}} = 0 \Rightarrow S_\tau^{\mathrm{OM}} = 0$. Therefore, one can see that while the phonon occupancy of the mechanical mode decreases, there is an counter-intuitive increase in the minimum resolvable torque spectrum. Physically, this can be understood due to the fact that any apparent reduction in the minimum resolvable torque by reducing the phonon occupancy of the resonator using back-action cooling, is negated by a commensurate increase in the mechanical damping rate. Therefore, a torsional optomechanical resonator must be passively cooled using a fridge to approach towards ground state occupation, achieving the quantum limit of torque sensitivity.

§ 4.2 Experiment

To meet the challenge of passively cooling our devices, we describe experimental details inside a dilution refrigerator. One outstanding aspect of this system is that the use of a dimpled-tapered optical fibre results in a total optical efficiency of $\eta = 32\%$, an improvement over other state-of-the-art quantum optomechanics experiments [105; 106], which aids in the low-power optical measurements. I begin with the basic layout of the chip, including the pluto design — which possess the best torque sensitivity and optomechanical coupling coefficient. Additional step-by-step fabrication recipes are shared to achieve the smallest gap made for this chip and to deposit superconducting materials on the landing pad for a potential hybrid system. Lastly, our efforts to construct dimpled-microfibre-compatible fridge are described.

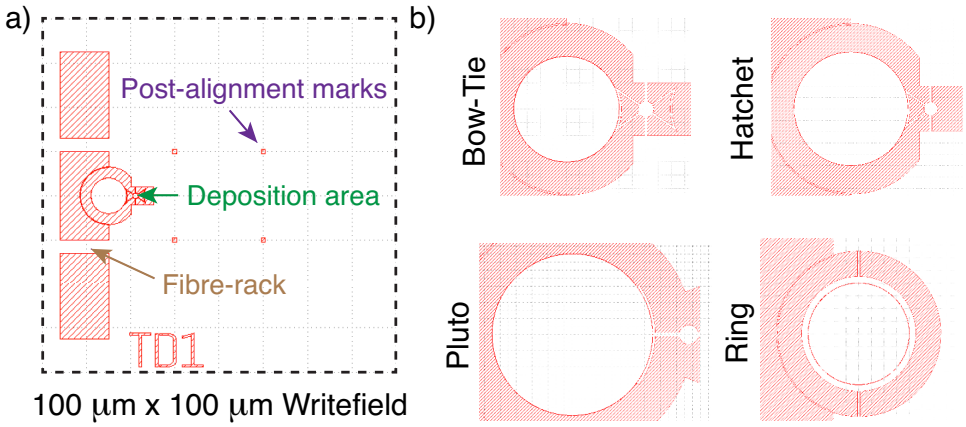

Figure 4.1: **GDSII layout for e-beam lithography** (a) A writefield is an 100 μm $\times$ 100 μm square area that is used for the pattern generator to directly expose the e-beam resist. At the centre, four 1 μm square alignment marks are designed for potential post-process of depositing materials. On the left side of the optical disk, a trench is designed to give room for dimpled microfibre manipulation, with two fibre-racks to hold the fibre in place. (b) Four different torque sensors are designed. For three designs, bow-tie, hatchet, and pluto, have a small 1 μm diameter area reserved for hybrid systems, whereas the ring-resonator design can explore optomechancial effects at low-temperatures.

4.2.1 Chip design

Measured Parameters	Material Parameters (Si)	Calculated Quantities
$l_1 = 155$ nm	$\rho = 2329$ kg·m^3	$\kappa_1 = 1.09 \times 10^{-10}$ N·m
$w_1 = 175$ nm	$E = 170$ GPa	$\kappa_2 = 1.16 \times 10^{-11}$ N·m
$l_2 = 1.46$ μm	$\nu = 0.28$	$I_{\kappa_1} = 1.23 \times 10^{-31}$ kg·m^2
$w_2 = 175$ nm		$I_{\kappa_2} = 1.15 \times 10^{-30}$ kg·m^2
$w_r = 125$ nm		$I_1 = 5.14 \times 10^{-29}$ kg·m^2
$t = 250$ nm		$I_2 = 8.06 \times 10^{-28}$ kg·m^2
$R_d = 570$ nm		
$R_r = 4.88$ μm		
$\psi = 60.2$ deg		
$r_{\max} = 2.51\mu$m		

Table 4.1: Measured and calculated parameters, as labelled in Fig. 4.2, for the torsional device studied in this work.

On the chip, there are total of 62 devices with four different designs, as seen in Fig. 4.1. With the best efforts to minimize the iteration process using FEM simulations (COMSOL), still ten trials were made to test the limitations of fabrication. The moment of inertia cannot be decreased indefinitely due to detection limits, and a maximum optomechanical coupling,

on the other hand, has generally large moment of inertia (see table 3.1). Also the beam length, or the torsion arm, cannot be arbitrarily long due to material properties, where a long beam with a given Young's modulus will cause sagging after the undercut process. Rather than listing all the solutions and improvements, I will state that the chip installed in a dilution refrigerator has the finalized mechanical dimensions (see table 4.1), where the only variation came from the gap between the optical and the mechanical resonators. This gap is an important feature as it improves the optomechanical coupling with a small trade-off in optical dissipation. In extremely small gaps, the torsional resonator would experience a short-ranged van der Waals force, but based on fabrication limitations in achieving < 40 nm gaps, the restoring force is assumed to be negligible [113].

4.2.1.1 Modelling of pluto design

As mentioned previously, the pluto design (Fig. 3.2e) was the winner for having a balanced low moment of inertia with a high optomechanical coupling. Here, a deposition area, a 1 μm diameter disk, is included along the torsion arm as a prototype for next implementation of magnetic films, including superconductors. Because of this addition, we treat this resonator as a coupled torsional oscillator (see Fig. 4.2c): one punctuated by the sample disk, the other by the ring segment used to couple to the optical disk, each with its own torsional spring constant, κ_i, and moment of inertia, I. From Eqn. 2.4, we see that in order to calculate the effective moment of inertia of a torsional mode, we need to determine its mechanical mode-shape by the density, $\rho(\boldsymbol{r})$, or more specifically, the scaling function, $h(y)$. For the geometry in Fig. 4.2b, the torsion rods have a simple rectangular cross-section, such that the torsional spring constants will be given by

$$\kappa_i = \frac{\beta w\ t^3 E}{2l\,(1+\nu)}, \tag{4.10}$$

where l and w are the length and width of the torsion rod, and t, E and ν are the thickness, Young's modulus and Poisson ratio of the device, while β is a numerical coefficient given by

$$\beta = \frac{1}{3}\left[1 - \frac{192}{\pi^5}\frac{w_i}{t}\sum_n^{\infty}\frac{1}{n^5}\tanh\left(\frac{n\pi t}{2w_i}\right)\right], \tag{4.11}$$

where n are positive odd integers [50; 114]. Note that we have assumed $t > w_i$, as this is the case for the device studied here.

The moment of inertia of the sample disk is found from its geometry to be

$$I_1 = \frac{m_d}{4}\left(R_d^2 + \frac{t^2}{3}\right), \tag{4.12}$$

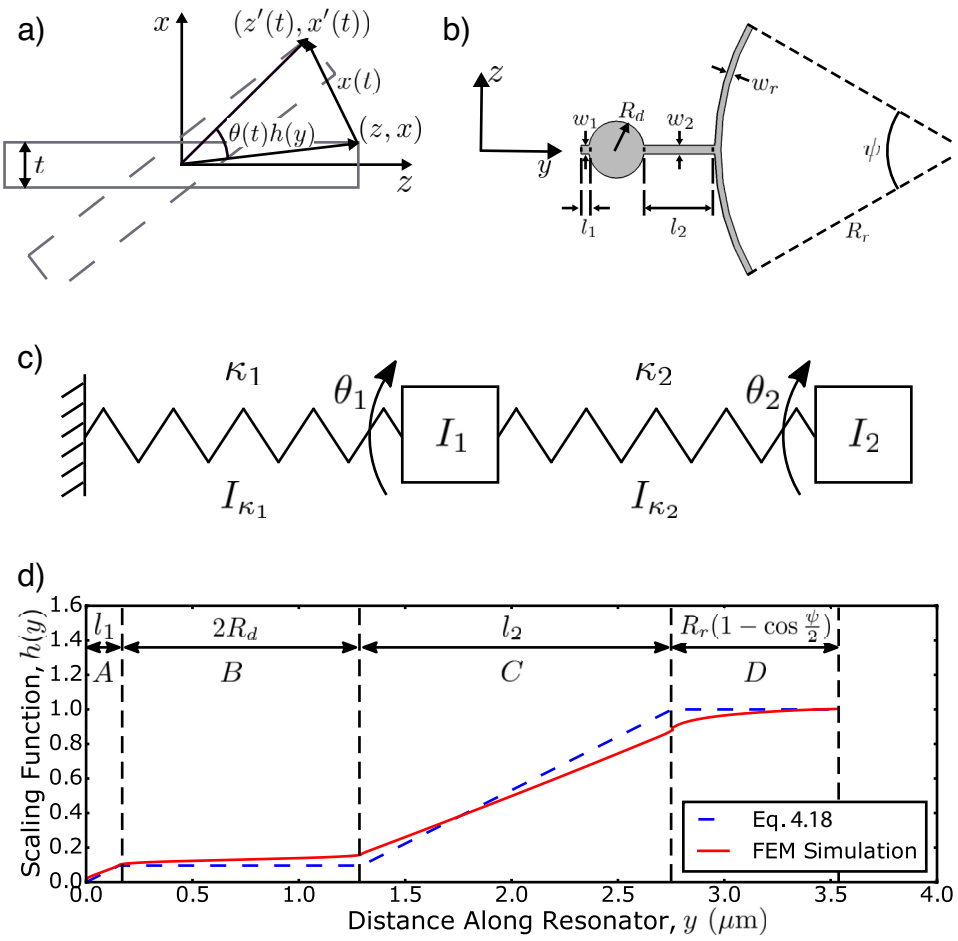

Figure 4.2: **Coupled torsional model schematic and angular scaling function** (a) A schematic depicting the out-of-plane displacement of a simple torsional mode. (b) A top-down view of the torsional resonator geometry used in this work with the critical dimensions labeled. The measured numerical value for each dimension can be found in table 4.1. (c) A torsional "mass-and-spring" diagram illustrating the simple coupled oscillator model. (d) Plot of the scaling function $h(y)$ using both the analytical model of Eqn. 4.18 (blue - dashed) and FEM simulation (red - solid), with the following four regions of the resonator demarcated: A - first torsion rod, B - sample disk, C - second torsion rod and D - ring segment.

where R_d and $m_d = \rho\pi R_d^2 t$ are the radius and mass of the sample disk (see Fig. 4.1b), with ρ being the density of the device. On the other hand, the moment of inertia of the ring segment is given by

$$I_2 = \frac{\rho t w_r \left(2R_r + wr\right)}{8}\left[\left(\left(R_r + w_r\right)^2 + R_r^2\right)\left(\psi - \sin\psi\right) + \frac{\psi t^2}{3}\right], \tag{4.13}$$

where w_r, R_r and ψ are the width, radius of curvature and sector angle of the ring segment (see Fig. 4.2b).

Once we have determined the above torsional spring constants and moments of inertia, the equations of motion for the device (excluding damping for simplicity) are then given by

$$\begin{aligned} I_1\ddot{\theta}_1 &= -\kappa_1\theta_1 - \kappa_2\left(\theta_1 - \theta_2\right), \\ I_2\ddot{\theta}_2 &= -\kappa_2(\theta_2 - \theta_1), \end{aligned} \tag{4.14}$$

where θ_1 (θ_2) is the angular displacement of the sample disk (ring segment), as demonstrated schematically in Fig. 4.2a. Applying a Fourier-transform to these equations of motion, such that $\ddot{\theta}_i = -\Omega^2\theta_i$, we can rewrite them in matrix form as $A\vec{\theta} = 0$, with A and $\vec{\theta}$ given by

$$A = \begin{bmatrix} \Omega^2 - \frac{\kappa_1+\kappa_2}{I_1} & \frac{\kappa_2}{I_1} \\ \frac{\kappa_2}{I_2} & \Omega^2 - \frac{\kappa_2}{I_2} \end{bmatrix}, \quad \vec{\theta} = \begin{bmatrix} \theta_1 \\ \theta_2 \end{bmatrix}. \tag{4.15}$$

Solving this system of equations, we find the eigenfrequencies of this coupled system to be

$$\Omega_\pm = \sqrt{\frac{1}{2}\left(\frac{\kappa_2}{I_2} + \frac{\kappa_1+\kappa_2}{I_1}\right) \pm \frac{1}{2}\sqrt{\left(\frac{\kappa_2}{I_2} + \frac{\kappa_1+\kappa_2}{I_1}\right)^2 - \frac{4\kappa_1\kappa_2}{I_1 I_2}}}, \tag{4.16}$$

where the negative (positive) frequency corresponds to the symmetric (antisymmetric) torsional mode. Note that for the experimental parameters given in table 4.1, $\Omega_-/2\pi = 18.1$ MHz, which is somewhat larger than the experimentally measured mechanical resonance frequency of $\Omega_\mathrm{m}/2\pi = 14.5$ MHz.

Focusing on the symmetric mode (as this is the mode examined in this work), we can insert the negative eigenfrequency, Ω_-, into the system of equations given by Eqn. 4.15 to obtain an expression for θ_2 in terms of θ_1 as

$$\theta_2 = \frac{1}{2}\left(-\frac{I_1}{I_2} + \frac{\kappa_1+\kappa_2}{\kappa_2} + \sqrt{\left(\frac{I_1}{I_2} + \frac{\kappa_1+\kappa_2}{\kappa_2}\right)^2 - \frac{4\kappa_1 I_1}{\kappa_2 I_2}}\right)\theta_1 \approx \frac{\kappa_1+\kappa_2}{\kappa_2}\theta_1, \tag{4.17}$$

where we have made the experimentally relevant approximation $I_1 \ll I_2$. We can now use the relative angular displacements of the sample disk and ring segments given in Eqn. 4.17 to determine the mode-shape scaling function $h(y)$. To do this, we assume the simplest imaginable torsional mode-shape [114; 115], where the mechanical device is rigidly clamped at one end ($\theta = 0$), with the angle of deflection increasing linearly along the torsion rods, while remaining constant over both the sample disk and ring segment. In this case, $h(y)$ is

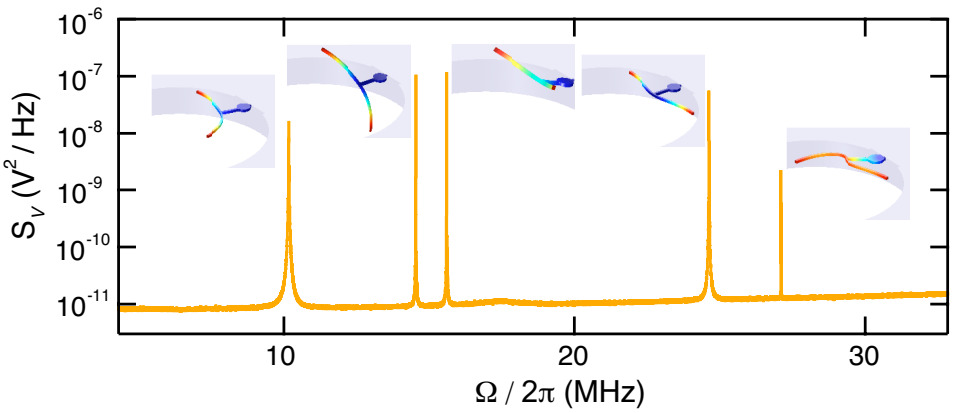

Figure 4.3: **Mechanical modes and simulations of pluto design** Optomechanically measured thermal noise voltage spectrum of the five mechanical modes at 4.2 K, associated with FEM simulations of the mode-shapes colour coded by their total displacements. The signal is optimized at the second resonance corresponding to the torsional mode.

given by the piecewise function

$$h(y) = \begin{cases} \frac{\kappa_2}{\kappa_1+\kappa_2}\frac{y}{l_1}, & y \in A \\ \frac{\kappa_2}{\kappa_1+\kappa_2}, & y \in B \\ \frac{\kappa_1}{\kappa_1+\kappa_2}\frac{y-l_1-2R_d}{l_2} + \frac{\kappa_2}{\kappa_1+\kappa_2}, & y \in C \\ 1, & y \in D. \end{cases} \tag{4.18}$$

A plot of this function using the measured/calculated device parameters (as given in Table 4.1) can be seen in Fig. 4.2d, where we have also defined the regions A-D.

Finally, by inputting Eqn. 4.18 into Eqn. 2.4, we can determine the effective moment of inertia for this simple analytical model to be

$$\begin{aligned} I &= \left(\frac{\theta_1}{\theta_2}\right)^2 \frac{I_{\kappa_1}}{3} + \left[1 + \frac{\theta_1}{\theta_2} + \left(\frac{\theta_1}{\theta_2}\right)^2\right] \frac{I_{\kappa_2}}{3} + \left(\frac{\theta_1}{\theta_2}\right)^2 I_1 + I_2 \\ &\approx \left(\frac{\kappa_2}{\kappa_1+\kappa_2}\right)^2 \frac{I_{\kappa_1}}{3} + \left[1 + \frac{\kappa_2}{\kappa_1+\kappa_2} + \left(\frac{\kappa_2}{\kappa_1+\kappa_2}\right)^2\right] \frac{I_{\kappa_2}}{3} + \left(\frac{\kappa_2}{\kappa_1+\kappa_2}\right)^2 I_1 + I_2 \approx I_2, \end{aligned} \tag{4.19}$$

where I_{κ_1} and I_{κ_2} are the geometric moments of inertia corresponding to the two torsion rods with spring constants κ_1 and κ_2 ($I_{\kappa_i} = \rho l_i w_i t(w_i^2 + t^2)/12$), and we have again used the experimentally valid approximation that $I_2 \gg I_1, I_{\kappa_1}, I_{\kappa_2}$. For the device studied here, the analytical model predicts an effective moment of inertia $I \approx I_2 = 807$ fg·μm^2.

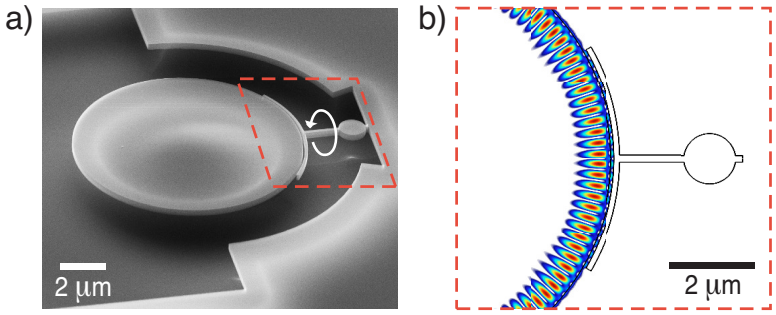

Figure 4.4: **Low-temperature optomechanics** (a) Tilted view of a SEM image of the singly clamped optomechanical torque sensor, which oscillates by the yellow arrow. A 10 μm diameter microdisk is evanescently coupled to a torsional resoantor by a gap of 60 nm. (b) A FEM simulation of the dispersively coupled optical fields. The scale bar is also 2 μm.

While the analytical model of the previous section allows for a qualitative understanding of the torsional mode-shape of our resonator, a much more accurate mode-shape, and therefore effective moment of inertia, can be determined using FEM simulations. An example of such a mode-shape generated using COMSOL can be seen in the inset of Fig. 4.3. From this simulated mode-shape, the effective moment of inertia of the device can be calculated numerically using Eqn. 2.4, for which we find a value of $I = 774$ fg$\cdot\mu$m^2. It is this value that we use to calculated the torque sensitivities.

Furthermore, the scaling function $h(y)$ extracted from the FEM simulation is compared to the analytically determined one given by Eqn. 4.18 in Fig. 4.2d, highlighting the deviation of the analytical model from the numerical one. This disparity is likely due to the fact that the analytical model ignores the resonator's support structure, as well as the elasticity of the material. As such, the analytical model overshoots the scaling function in the critical region of the ring segment, predicting a larger effective moment of inertia than the numerical model.

Placing the singly-clamped torsional resonator next to an optical disk, as seen in Fig. 4.4, the coupling should be nonlinear — where the observed frequency should be twice the mechanical frequency from the quadratic coupling. However, the data seem to agree with the FEM simulation to first order, suggesting that the optomechanical coupling is linear. There are two suggested sources of linear coupling: the slanted sidewalls based on imperfect nanofabrication and asymmetric optical mode due to the dimpled microfibre placement on the disk. In some cases, I have observed a small second order peak in addition to the first order coupling, similar to the cantilever example in Ref. [69]. Despite the best efforts

to achieve second order coupling by making straighter sidewalls and having a fibre-rack (Fig. 4.1a) for evanescent coupling, the optomechanical coupling tends to be dominantly linear. For the rest of our discussion in torque sensitivity, we will assume linear coupling for the optomechanical torque sensors.

4.2.2 Nanofabrication

The core of our optomechanical design is an optical disk resonator, diameter of 10 μm, evanescently coupled with the mechanical torsional element via a small gap. This total separation of mechanics and optics aids in thermalization at low-temperatures, but the gap is small enough ($\sim$60 μm) to have good overlap of optical field and displacement field to achieve large coupling (G_θ = 3.4 GHz/mrad, G_x = 1.4 GHz/nm), which is necessary to observe mechanical response at low power and low-temperature. Hence the scope of the fabrication methods were to obtain the smallest gap and to test the possibility of hybrid structures with metal films. Since the general principles of e-beam lithography were already shared, I will enumerate the recipe as a reference and further discuss the latter part of hybrid device fabrication.

4.2.2.1 Fabrication recipe of a SOI torque sensor

1. Prepare a chip (250 nm thick SOI chip with 3 μm buried oxide layer)
    - The chips are diced into 10 mm $\times$ 5 mm rectangle with a protective HPR506 resist-coating
    - Rinse 3 times with Acetone followed by IPA to remove the resist
    - Final rinse with DI H_2O (Deionized water) with N_2 dry
2. Piranha clean
    - Mix 800 mL H_2SO_4 with 200 mL H_2O_2 and place the chip close to the meniscus (80 °C hot region)
    - Clean for 20 minutes
    - Rinse the chip with DI H_2O 5 times followed by a N_2 dry
3. HF dip
    - A quick 40 s rinse in concentrated HF (49%)
    - Rinse the chip with DI H_2O 5 times followed by a N_2 dry
4. Resist spin

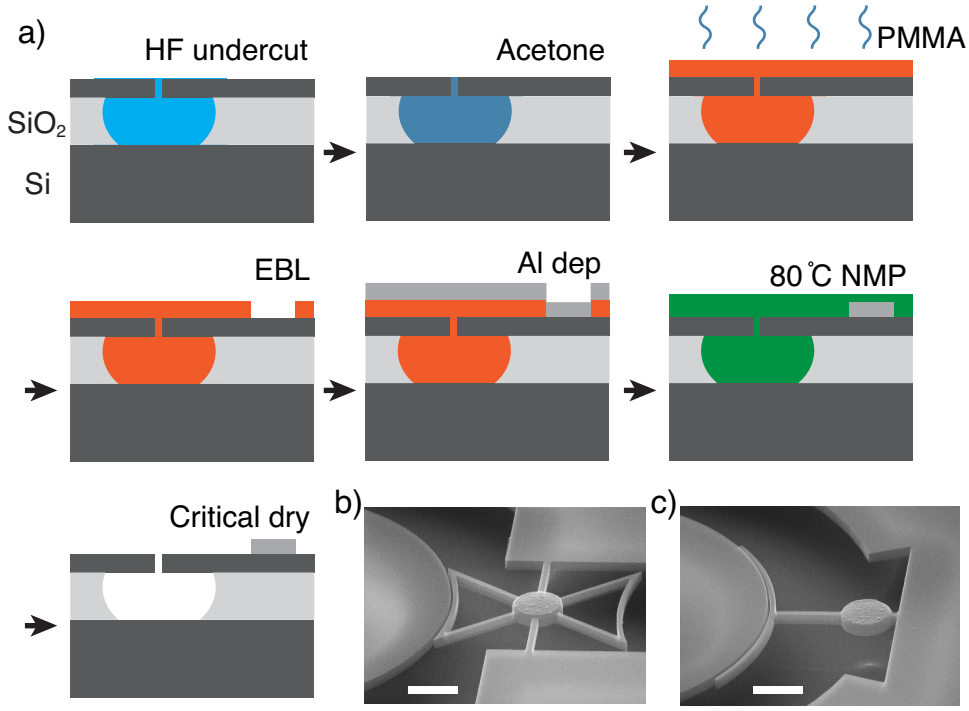

Figure 4.5: **Modified processflow for hybrid structures** (a) Additional steps to Fig. 3.3 have been taken to address hybrid structure to pattern aluminium disk on the optomechanical torque sensor. Followed by a HF undercut, the chip is submerged in acetone without drying. Placing the chip on a chuck, with an acetone droplet intact, PMMA950k-A8 resist is supplied as the solvent evaporates in air. After the solvent is fully replaced with the resist, spinning and baking is performed to prepare for EBL. Post-alignment is performed to create small windows for aluminium deposition. After e-beam evaporation, a lift-off process in a stronger solvent (NMP) is made to ensure cleanliness against the resist. Finally, a critical point drier is used to avoid stiction, producing hybrid (b) bow-tie and (c) pluto devices with 45 nm Al thick disks.

- Place the chip on the smallest chuck on the Brewer spinner
- Ensure that the ZEP-N50 resist is warmed up to room temperature (pull the bottle out of the storage fridge during the previous cleaning steps)
- Put 2 droplets on the chip using a pipette such that they are contained on the chip without spilling on the edges
- After waiting 1 minutes, spin the resist using the recipe "PK_ZEP"
  - spin: 100 RPM, ramp: 100 RPM/s, time: 2 s
  - spin: 5000 RPM, ramp: 2500 RPM/s, time: 60 s
- Inspect the back-side of the chip (soak cleanroom-compatible Q-tips with ace-

tone/IPA to wipe out excess resist on the back-side.

- For immediate EBL use, bake the chip at 180 °C for 20 minutes followed by a 15 minutes waiting period (cool-down/hydration period)
- For later usage (> 1 day), then baking is not necessary
- The resist thickness should be uniform near the centre (∼325 nm). Resists are thicker near the edge (called the edge bead), so avoid patterning near the edges.

5. EBL

   - Scratch the bottom left corner of the chip using a diamond tip prior to loading in RAITH-150Two
   - Define the bottom left corner (U, V) = (0, 0) and perform an angle alignment
   - Focus on a particle near the scratched corner with 30 kV EHT (accelerating voltage) and 10 μm (aperature)
   - Perform a write-field alignment until four zero's or nine's are obtained (*i.e.*X: 0.99994, Y: 1.00003)
   - Record the beam current in units of pA
   - Set dose at 310 μC/cm^2 for cold-development (128 μC/cm^2 for room-temperature development)
   - Adjust the curve-step as 8 nm and area-step as 4 nm
   - Run the position-list file (.pls format) which includes GDSII layout file (.csf format)
   - Development
     - Using Stir-Kool cold plate, set the developer (ZED-N50) and quencher (IPA) at −15 °C using a stir-stick at 70 RPM
     - Develop in ZED-N50 for 20 s followed by a IPA rinse for 20 s
     - N_2 dry immediately without the use of water rinse

6. RIE at NRC-NANO cleanroom (Oxford Chlorine etcher)

   - Conditioning a blank Si wafer using "Si Mixed etch_opt1" recipe for 10 minutes
   - Mount the chip on a wafer near the centre using a small dab of silicone grease for adhesion
   - Process the chip for 46 s using the same recipe
   - Finish with a 20 minute O_2 chamber cleaning recipe

7. Resist strip

- Use Ozone-bonder, without O_2 flow, as a UV flood source
- Process for 15 minutes
- Soak with PG remover for 2 minutes followed by $\times 5$ DI H_2O rinse

8. Piranha clean
   - Prepare the same piranha solution as before and clean for 20 minutes
9. BOE/HF undercut
   - Soak in BOE solution for 26 minutes followed by $\times 5$ DI H_2O rinse
   - Rinse in a diluted HF for 1 minute followed by $\times 5$ DI H_2O rinse
   - Soak the chip in IPA
10. CPD
    - Load the chip as seen in Fig. 3.7b
    - Set purge dial to 2
    - Gentle N_2 blow to remove any dust on the sample
    - Rush to the apparatus, store it in vacuum or N_2 environment

The pluto device, patterned and fabricated on a SOI chip, is shown in Fig. 4.4a, where a nice gap of 60 nm is formed. At room temperature, this particular device demonstrates $Q_m = 8151$, $\Omega_m = 11.09$ MHz, and $\sqrt{S_\tau} = 0.5$ zNm/$\sqrt{\text{Hz}}$. Prior to the experimental details regarding the optomechanical apparatus in a dilution refrigerator, I will now highlight a parallel process to the chip, where an aluminium disk was selectively deposited on the landing pad as shown in Fig. 4.5bc.

4.2.2.2 Deposition

Although testing the limits of torque sensitivity by means of design, nanofabrication, and temperature, are important — these efforts would have been in vain if torque sensors cannot demonstrate hybrid systems, such as to study magnetism. For example, when a magnetized sample on a torque sensor is under an alternating field, the torsional mode feels a torque that can be studied to extract material properties and study nanoscale physics. As a preview to next chapters of hybrid systems, I demonstrate our first prototype to incorporate aluminium films to our torque sensors. Beginning with some deposition principles of metal films, a modification to the previous recipe, based on Ref. [85], is shared. Note that prior to deposition, a secondary EBL lithography is processed for a lift-off procedure.

Thermal Evaporation

There are two common ways to deposit thin films by the use of thermal evaporation or by sputtering in either DC or RF plasma. In thermal evaporation, a low base pressure is required, in which the evaporated atoms can flow with a long mean free path, or minimal collision with residual gas atoms from the source to the substrate. To achieve pressure in the range of ($< 10^{-6}$ Torr), a cryo-pump, ion-pump, or a diffusion-pump is required to acquire high quality films. In the case of an electron-gun evaporator, a strong e-beam (10 kV) is magnetically steered to hit the source target, which is placed in a water-cooled carbon crucible. The e-beam evaporates a small area of a target material until the vapour pressure is high enough to acquire a steady deposition rate. Once the shield is opened, the ballistic transport from the source adheres to a resist-patterned chip mounted upside down. Since the metal coverage is protected by a patterened e-beam resist, usually a bi-layer PMMA film, a lift-off process can transfer the e-beam pattern to a material pattern. For alunimium, the adhesion strength is quite strong to the substrate; however, some films, such as gold, require an additional adhesion layer of Cr or Ti to promote adhesion. In the case of Cr, the film evaporates from a solid phase (sublimation), where it is hard to control the deposition rate due to inconsistent thermal contact of the e-beam. Here, the thickness of the deposited material is monitored using a calibrated quartz crystal microbalance. Despite the benefit of high quality films, based on the base-pressure, an evaporator system is also not usually compatible for insulating devices, as the built-up charge and deflections will usually cause contamination of the chamber. Hence, it is often easier to work with a sputtering system for film uniformity and wide range of films including insulators.

Sputter deposition

Similar to thermal evaporation, the base-pressure of the chamber plays an important role to the quality of the film, ensuring a clean slate prior to introducing an inert gas, such as Ar, for generating a plasma. One common type of sputtering gun is planar magnetron, where magnets are placed behind the cathode, made of the sputter material, and the anode faces the cathode, trapping the plasma tightly between the two plates. High energy ions ablate the target and are transported to the substrate with some kinetic energy. In contrast to an evaporator system, number of collision process occur which give rise to a possibility of reactive sputtering. For example, a flow of nitrogen gas with an Al target, allows an AlN film to be deposited (see appendix). Here RF sputtering is used to deposit insulating films, where the deposition is part of a series capcitance — where changing the RF network does not impact the deposition rate. Due to residual kinetic energy, there is better coverage of material to the substrate, where a bi-layer PMMA lift-off recipe does not work as well as the directional deposition (*i.e.* evaporation). Therefore, a thicker resist (three-to-one ratio of the resist to the film thickness) is needed to lift-off using sputtering. Although sputtering is

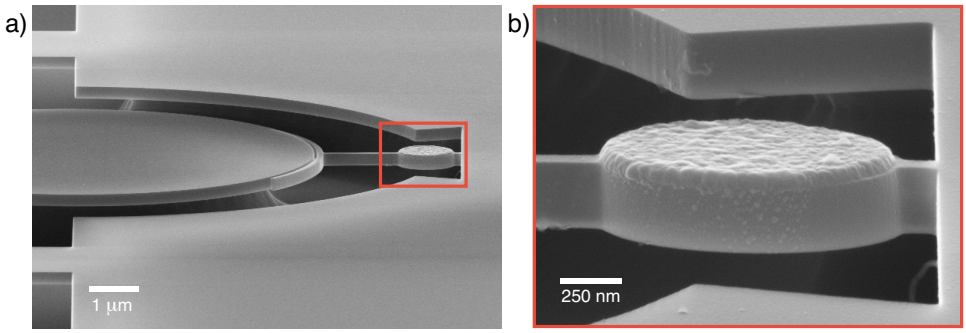

Figure 4.6: **Prototype of optomechanical studies for mesoscopic superconductivity** (a) Tilted SEM image to demonstrate the optomechanical torque sensing platform via integration of a single mesoscopic aluminium disk (1.2 μm diameter, 45 nm thick) and a (b) zoomed image of the red box.

widely used for wide range of targets, the quality of the film is not comparable to evaporation or chemical vapour deposition due to the difference in deposition pressure.

4.2.2.3 Prototype of superconducting disk NOMS torque sensor

For superconductor deposition, evaporation is used to ensure the quality of the film. However, the major problem does not originate from the deposition methods but the etching process where BOE/HF-water mixtures etch aluminium and most magnetic materials. A modification to the recipe is made to Fig. 3.3: prior to the CPD, an additional step is included, where the chip was transferred to an acetone solution. Note that this procedure is outlined in Ref. [85], where PMMA950k-A8 resist was added on the acetone droplet on the chip to replace the liquid to the resist without ever drying. After spinning the resist, writefield alignments were done on the already patterned alignment marks (four 1 μm $\times$ 1 μm squares near to the centre of the write-field, see Fig. 4.1a). For this process, the visibility during the alignment procedure was poor, due to the thick PMMA layer of 730 nm, but increasing the box size to 5 μm made the alignment possible with great accuracy. A high-purity aluminium (99.9999%) was deposited using a e-gun evaporation system. The chamber was cryo-pumped overnight (2×10^{-7} Torr) to avoid oxidation during the deposition process. After depositing 45 nm thick aluminium film, the lift-off was done in NMP (N-Methyl-2-pyrrolidone) solvent for 1 hour at 80°C. After the resist was stripped, we transferred to IPA solvent to do the final step of critical point drying. Despite the best efforts to handle the solvent-resist replacement process, most of the small gaps did not survive during this step — yielding a small percentage of larger-gap devices ($\sim$10%). Although this method works for most magnetic applications, a sensitive small gap structure needs an alternative method. Fortunately, VHF does not attack most metals, including aluminium films, where

we will see some examples VHF with iron and permalloy in the next chapters with full yield.

4.2.3 Optomechanics apparatus in a dilution refrigerator

Fortunately, the area of cavity optomechanics has seen remarkable success when integrated into cryogenic environments and the number of low-temperature optomechanics are continually growing. Multiple architectures are now capable of cooling to the ground state either directly through passive cooling [8; 105; 106], or in combination with optomechanical active cooling [24; 107]. Yet, as we demonstrate later, the purpose of this study is to show that only passive cooling is advantageous in relation to reducing the noise in an optomechanical torque sensor. Hence the optomechanical apparatus must be carefully constructed to thermalize strongly to the mixing chamber, while minimizing thermal drifts at low-temperatures — important for alignment procedure of of dimpled microfibres to an optical disk. The basic layout of the apparatus was inspired by the straight-forward detection mechanism: the incident photons confined in an optical cavity probes torsional oscillations encoded in changes of optical-pathlengths. To use the same fibre-based setup, the implication is not that simple as to simply change the translation stages to a low-temperature-compatible attocubes. Re-engineering of the microscope to a fibre-bundle endoscope is just one example, shared previously, of changes made to the apparatus. Here I will highlight our efforts to minimize thermal contractions, while thermally linking on-chip devices to the baseplate of the mixing chamber — which consequently allowed successful manoeuvrability of the dimpled fibre to a particular device of choice.

4.2.3.1 Thermal contraction

Recall that one of the effective strategies to inject photons to the optical cavity was the use of dimpled tapered fibres — where the smaller dimples (radius of curvature of $\sim$ 30 μm) are now comparable spatially to the optical cavity (radius of $\sim$5 μm disk). To replicate the room temperature apparatus on the dilution refrigerator, the first step is to work with materials that have low thermal contraction. As seen in Fig. 4.7a, the best material for low thermal contraction is Invar (FeNi36), having $\sim$ 0.05% contraction from 300 K to 4 K. After the fibre-fork is machined, I secured a dimpled tapered fibre by applying a cryogenically compatible epoxy called Tra-bond (Loctite bipax 2151), as pictured in Fig. 4.7b. Note that the dimpled fibre was slightly detentioned $\sim$ 30 μm during the gluing procedure to account for the tensioning at low-temperature. The whole apparatus sits on a Invar plate (green highlighted parts in Fig 4.7c) such that the fibre and the device have minimum thermal drifts.

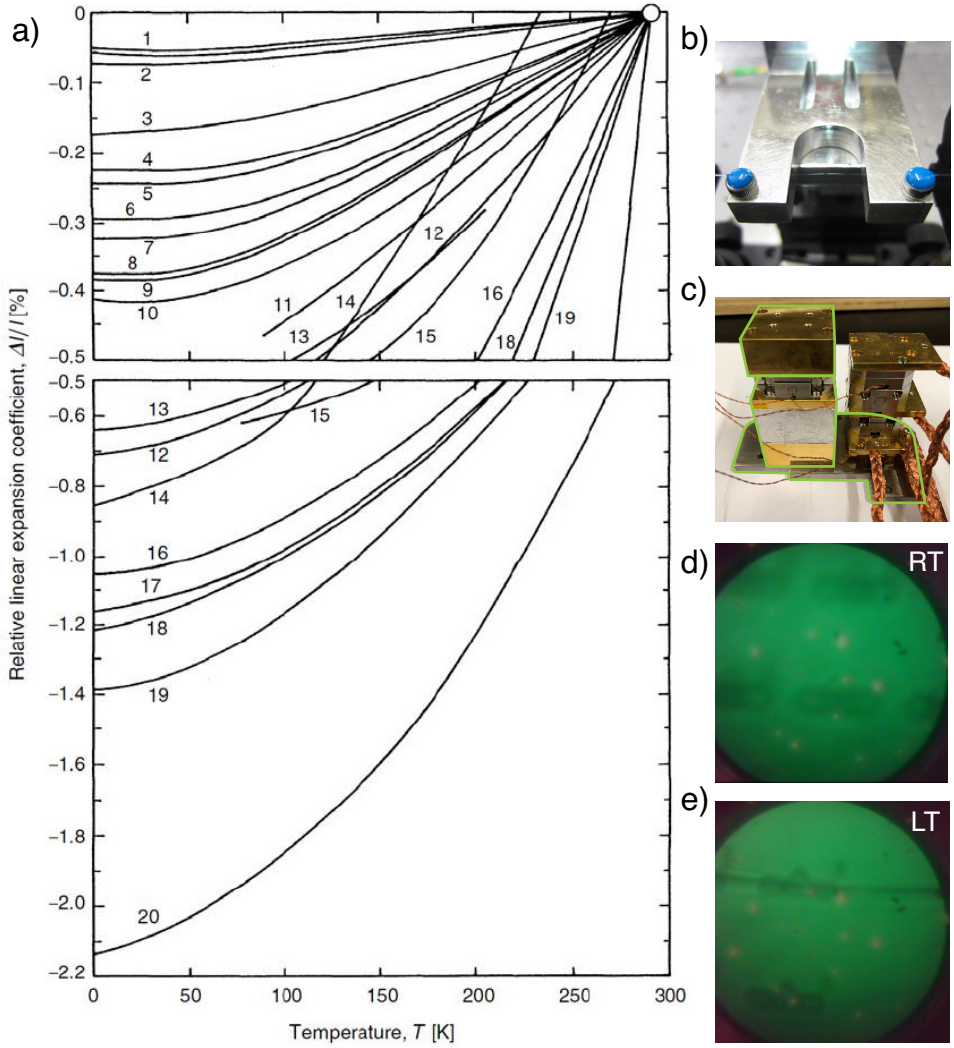

Figure 4.7: **Thermal expansions of various materials and our apparatus** (a) Thermal expansion coefficients of various materials as a function of temperature from 0 to 300 K (from Ref. [98]). For the materials used in our experiment: 1) Invar and glass, 7) copper, and 10) aluminium. (b) An Invar fork holds the dimpled-microfibre using low-temperature-compatible glue, Tra-bond, with thermal expansion between 10) and 11). (c) The base of the apparatus and the fibre-fork mount were all machined out of Invar to minimize thermal contractions at low-temperatures (outlined in green). Since we have the endoscope, we can account for the contractions occurring at low-temperatures by having a certain offset prior to cool-down. Hence, the tapered fibre is not visible in the (d) room temperature case, but through thermal contractions the tapered fibre is clearly located using an endoscope at (e) low-temperatures.

The challenge is often locating the dimple at low-temperatures, despite the imaging system from the fibre-bundle because the endoscope is fixed in x, y position and magnification. It requires some trial-and-error to locate the dimpled tapered fibre after the cooldown. Here the optimized magnification gives the image circle of ~ 850 μm in diameter, and we have found an ideal position for the dimpled-microfibre: applying a 3/4 turn clockwise, using a 6-32 adjustment screw (or ~ 590 μm), such that the dimpled fibre escapes at the top of the image (Fig. 4.7d). Here a red HeNe laser is used to assist in this process, where the scattering pattern, known previously (Fig. 4.9)c, is used to pin-point the dimple. After cooling the apparatus, the fibre is in sight where we can move laterally to locate the dimple with a red diode laser. The purpose of the red laser is to realize the scattering of the dimple when touching the chip with the fibre.

4.2.3.2 Thermal conduction

Heat can be transferred by conduction, convection, and radiation; hence, the challenge is to minimize external heatload, while the chip is thermally anchored to the base-plate. The apparatus is located in a radiation shield inside the IVC where aluminium tape is used to cover holes between plates to minimize radiation heating. Pumping-down the IVC with a turbo-molecular pump (TMP) reduces convection heating from the dewar, while thermal conduction is maximized for on-chip devices to the mixing chamber of the dilution fridge, the sample chip is clamped onto a gold-plated oxygen free high-purity copper (OFHC) mount, sitting on a stack of low-temperature-compatible nanopositioners, with thermal braids linking them to the base-plate of the dilution refrigerator. With this set-up, we were able to refrigerate down to 9 mK, comparable to the unloaded base-temperature of the fridge (6 mK).

4.2.3.3 Dimpled tapered microfibre in the dilution refrigerator

Our system is fully fibre-based, which aids in low-power optical measurements at the fridge base temperature of 9 mK. To reduce the heat load from the long fibre, it is taped around the plates multiple times down to the mixing chamber such that the fibre is cold as well (Fig. 4.9a). After installation, as seen in Fig. 4.9d, there are some transmission losses during the cool-down procedures, but transmission stays rather stable after reaching 4.2 K. There are a total of four attocubes, low-temperature-compatible nano-positioners, where three are responsible for x-y-z axis of the chip and the remaining one moves the fibre mount along the fibre to find the dimple. With stable transmission, at low-temperatures, alignment has been successful as seen in Fig. 4.9 where the lowest spot was placed on the fibre-racks (see Fig. 4.1a). Note that the fibre-circuit, outside the fridge, is omitted as it is near-identical to the room temperature case, as illustrated in Fig. 3.9a.

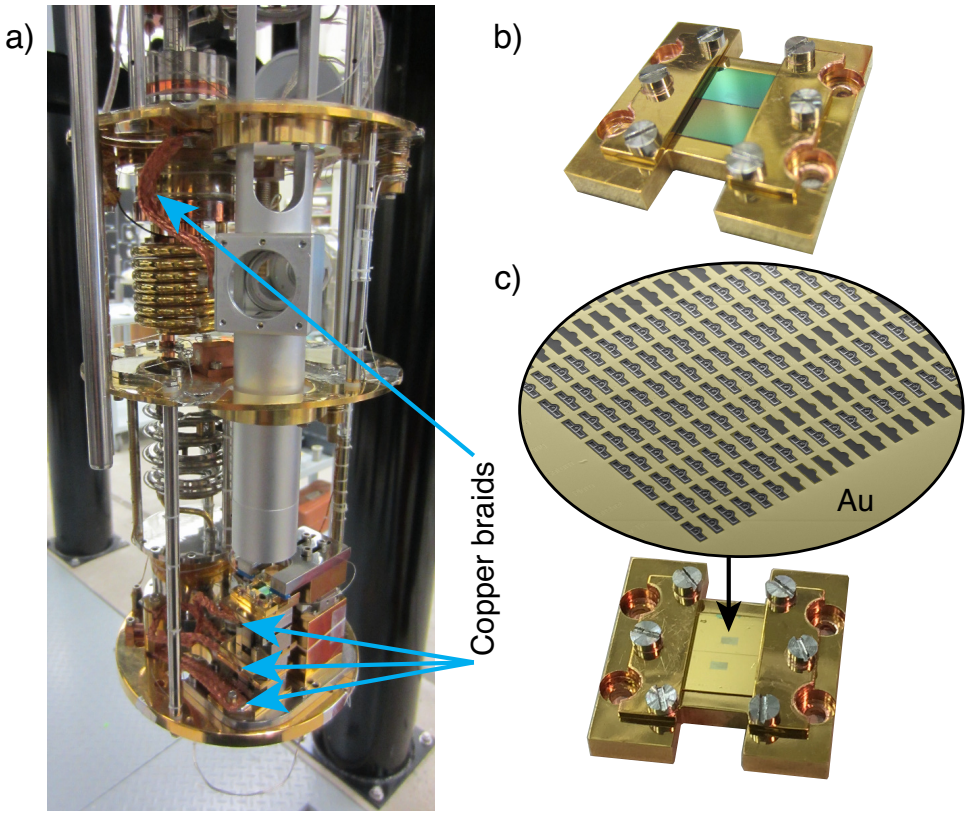

Figure 4.8: **Thermal conduction** (a) High purity copper braids are used throughout the fridge, even for our chip, to provide thermal pathways to its cold-plate. Between the three nanopositioning stages and the chip holder, three copper braids are mounted to the mixing chamber. (b) Two chips are firmly mounted on the holder, made out of gold-plated OFHC, to minimize thermal contact resistance. The top chip is the SOI chip for torque sensors and the bottom chip is a SiN chip for other project. (c) For the next generation of chips, not used in this thesis, the chip is gold-patterned around the devices to produce a better thermal conduction.

§ 4.3 Results and discussion

The torsional mechanical mode of the pluto device, at $\Omega_m/2\pi = 14.5$ MHz, has a low effective mass [86], $m_{\text{eff}} = 123$ fg (geometric mass of 1.14 fg), and a low effective moment of inertia: $I = 774$ fg·μm^2. To measure the small angular motion of the device, we engineer a large dispersive optomechanical coupling, $G/2\pi = \partial\omega_{\text{cav}}/\partial z$. The arms of the torsional resonator arc along the optical disk over one sixth of the perimeter of the disk, resulting in $G/2\pi = 1.4$ GHz/nm, while reducing the optical absorption in the mechanical element as compared to optomechanical crystals [17; 105]. In addition, the optical resonance at 1605 nm is strongly

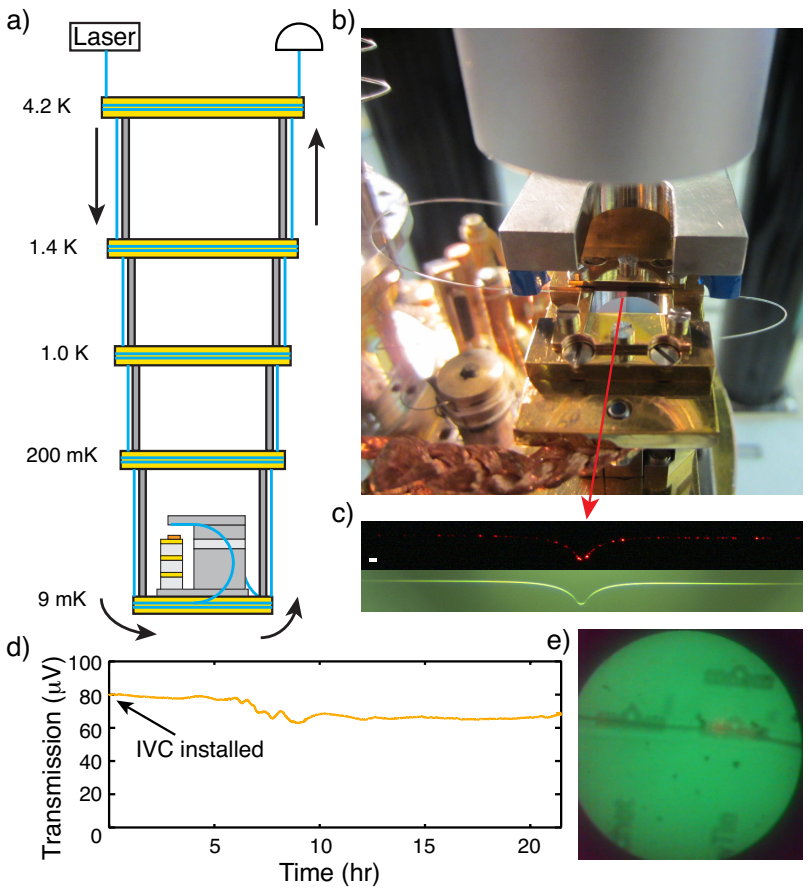

Figure 4.9: **Dimpled microfibre system in a dilution refrigerator** (a) A schematic of the optical fibre system. A long spool of fibre is thermally anchored to each stage of the fridge, and aluminium tapes are used to secure it in place. The dimpled tapered fibre mounted on a Invar fork is fusion spliced at the bottom such that the connection between the laser and the photodiode is made. (b) A photograph of the assembly of the chip and the dimpled microfibre, where extra caution was made to reduce the overhang such that the fibre does not touch the IVC, avoiding heatload from the IVC wall. (c) Microscope images of the dimpled tapered-fibre used for the experiment: the top image transmits a red HeNe laser where scattered spots were observed near the tapered region. The scale bar is 65 μm. (d) After mounting the fibre to the dilution apparatus, the IVC is closed with an indium-seal. The transmission is monitored during the cool-down process. There are some optical transmission losses during the one-day period, but transmission remains constant after reaching a stabilized temperature at 4.2 K. (e) An example of an endoscope image during the coupling procedure. Here we see a red scattering on the fibre-rack, where it is touched, due to a red diode laser.

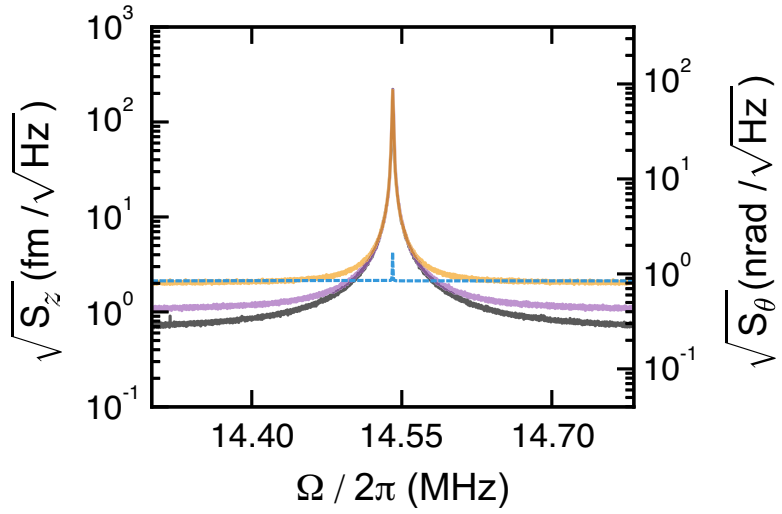

Figure 4.10: **Power dependence at 4.2 K** Optomechanically measured thermal motion of the nanomechanical torsional resonator in the presence of helium exchange gas. As the optical power injected into the device in increased, the photon shot noise is reduced and the measurement imprecision drops below that corresponding the standard quantum limit. Power (number of photons) in the optical resonator corresponds to orange 21 μW (0.2 $\times 10^{15}$ photons/s), yellow 57 μW (0.5 $\times 10^{15}$ photons/s), blue 103 μW (0.8 $\times 10^{15}$ photons/s). Zero-point power spectra, calculated from measured device parameters, shown as the green dashed line.

over-coupled, $\kappa_e = 44$ GHz and $\kappa_i = 16$ GHz, to reduce optical absorption. Due to the small mass and low frequency, the zero point motion is relatively large at $z_{zpf} = \sqrt{\hbar/2m_{eff}\Omega_m} = 66$ fm. The resulting single-phonon coupling rate is $g_0/2\pi = Gz_{zpf}/2\pi = 12$ kHz, and the single photon cooperativity is $C_0 = \frac{4g_0^2}{\kappa_{cav}\Gamma} = 2 \times 10^{-4}$, which describes the efficiency in exchanging photons and phonons in a optomechanical system. Here I am merely using the sensitive transduction scheme without trying to manipulate the mechanics by optomechanical effects, where a low cooperativity is desired for my application.

As mentioned previously, there are other designs on the chip: namely bow-tie, hatchet and ring resonators. These devices also tend to have great torsional properties (see Table. 3.1); however, two main results for the pluto devices at 4.2 K and at 17 mK are highlighted in this chapter.

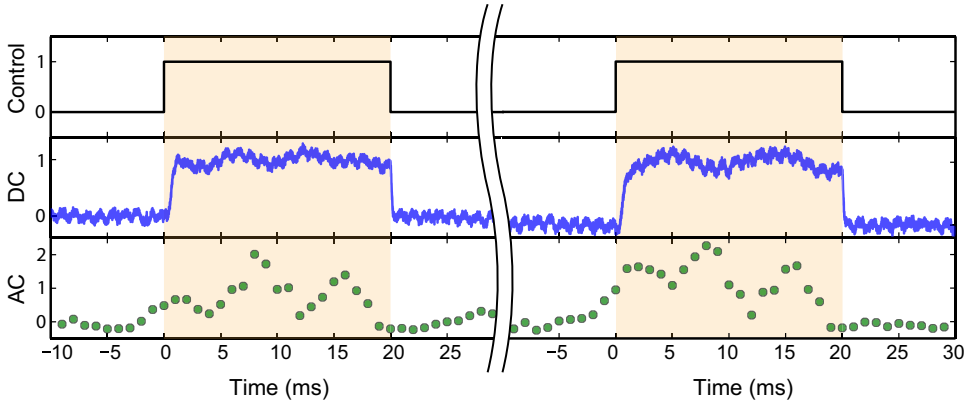

Figure 4.11: **Low duty-cycle measurement scheme** When the device is thermalized to the dilution refrigerator base-plate (17 mK) by copper braids, the heating from a continuous laser (1605 nm) can be significant. To circumvent the resistive heating from optical powers, we implemented a low-duty cycle measurement scheme of 20 ms of data acquisition window followed by a 2 minute waiting period using a voltage controlled variable optical attenuator (VCVOA). At each equilibrated temperatures of the base plate using a PID controller, we averaged 20 ms of data over an hour to get our mechanical spectrum.

4.3.1 Measurements at 4.2 K

First, we find that ^{4}He exchange gas is efficient (by convection cooling) to thermalize optomechanical resonators at 4.2 K, even at high optical input powers [110; 91]. It is true that the there is an upper limit on the input laser power, which may cause deformation of the dimple, two-photon absorption in silicon, and heat-load on the mechanical oscillator; however, with sufficient continuous power above $P_{\rm in} > P_{\rm SQL} = 8\ \mu$W, this device enables measurement imprecision (or a constant noise floor) below the SQL, as shown in Fig. 4.9. Here the torque sensitivity reached was 22 yNm/$\sqrt{\rm Hz}$ at 4.2 K which is already $\times$22 smaller than the room temperature sensitivity. In addition to torque sensitivity, this device displays excellent displacement sensitivity of 0.5 fm/$\sqrt{\rm Hz}$.

4.3.2 The best achievable sensitivity at 25 mK

In contrast to dissipationless superconducting circuits of microwave optomechanics [24], telecom wavelengths are bound to cause optical heating in the absence of exchange gas [105; 106; 91; 116]. To avoid parasitic optical-induced heating at millikelvin temperatures (with a small power of $P_{\rm dim}$=1.26 μW) we lowered the duty cycle of the optomechanical measurement using a voltage-controlled variable optical attenuator, (VCVOA) we apply a 20 ms optical pulse (limited by the mechanical linewidth) while continuously acquiring AC

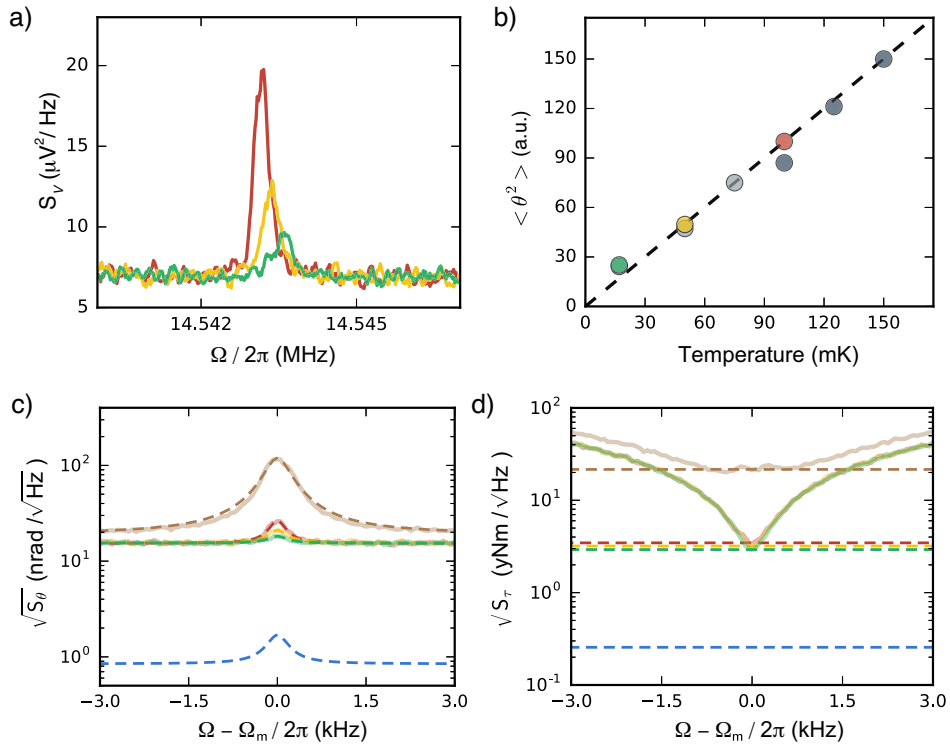

Figure 4.12: **Data at mK temperatures** (a) Power spectral densities of the torsional resonance at bath temperatures of 100 mK (red), 50 mK (yellow) and 17 mK (green) using low duty cycle measurements. (b) The integrated area under the curve as a function of bath temperature for three trial runs. The coloured data corresponds to the data in (a), where light and dark grey points are two additional trials. With a low duty cycle measurement and heavy averaging, only three data points can be obtained for each trial due to an existing slow drift in the system. The minimum thermalized temperature is 25 mK. (c) Calibrated angular displacement spectrum of the torsional mode at 4.2 K (brown), 100 mK (red), 50 mK (yellow), and 25 mK (green) with corresponding zero-point fluctuations at the SQL (blue). (d) Calibrated torque sensitivities corresponding to (c) where dashed lines are the resonant torque sensitivity, with a record of 2.9 yNm/$\sqrt{\text{Hz}}$ at 25 mK, just over a factor of 10 above its fundamental quantum limit of 0.26 yNm/$\sqrt{\text{Hz}}$.

time-domain data, which were subsequently Fourier transformed. We then waited 120 s (corresponding to a duty cycle of 0.017%) to re-thermalize the mechanical mode to the bath. To obtain sufficient signal-to-noise, this optical pulse sequence was repeated 100 times as seen in Fig. 4.11. The averaged results are shown in Fig. 4.12, where we extract the mode temperature by the linearity of the area under the mechanical resonance to the temperature at the mixing chamber (Fig. 4.12b). The resulting averaged power spectral densities, as shown

in Fig. 4.12a, are fit [86] to extract the area under the mechanical resonance, $\langle\theta^2\rangle$, which is proportional to the device temperature. The mechanical mode temperature is confirmed by comparing the linearity of the area under the power spectral densities with the mixing chamber temperatures, as measured by the fast ruthenium oxide thermometer referenced to the ^{60}Co primary thermometer, Fig. 4.12b. We find that at the mechanical mode is well thermalized to the bath temperature, until $\sim$ 17 mK at which point the mechanical mode limits to $\sim$ 25 mK — corresponding to an average phonon occupancy of $\langle n\rangle = 35$. The limitation was a small systematic drift in the period of $\sim$6 hours, where only three sequence at a time could be obtained.

According to Eqn. 4.7, $\langle n\rangle = 35$ places the torque sensitivity a factor of six above the fundamental quantum limit, when operating at the SQL. Yet thermomechanical calibration of the displacement using the mechanical mode temperature reveals that the low optical powers used to limit heating result in measurement imprecision above the SQL, Fig. 4.12c. Specifically, we find that we have $\sim$ 65 quanta of measurement noise — instead of the ideal single quanta — dominated by measurement imprecision, placing these measurements approximately ten times above the standard quantum limit. Nonetheless, calibration in terms of torque sensitivity, 4.12d, reveals that at temperatures below 100 mK we reach ~ 3 yNm/$\sqrt{\text{Hz}}$, more than a 260-fold improvement over previous generations of torque sensors [48; 70] and more than 160-fold improvement from the room temperature sensitivity of the same device.

To give some idea of what a torque sensitivity of 2.9 yNm/$\sqrt{\text{Hz}}$ enables, imagine an experimental scenario as in Refs. [117; 2], where the torsional mode is driven on resonance by an AC magnetic field, $\boldsymbol{H}$, orthogonal to both the magnetic moment of the test sample and the torsional axis, $\boldsymbol{\tau} = \boldsymbol{m} \times \boldsymbol{H}$. A reasonable drive field of 1 kA/m would imply the ability to resolve 325 μ_B, where μ_B is the Bohr magneton, or the moment of an electron spin.

§ 4.4 Conclusion and outlook

Excitingly, this sensitivity allows unleashing the advanced toolbox of mechanical torque spectroscopy [29; 47; 2] on mesoscopic superconductors, previously limited to static measurements of bulk magnetization via ballistic Hall bars with $\sim 10^3\mu_\text{B}$ sensitivity [118]. As a first step in this direction, we show in Fig. 4.6 a prototype optomechanical torsional resonator with a single micron-scale aluminium disk integrated onto its landing pad, fabricated

via secondary post-release e-beam lithography [85]. Room-temperature optomechanical measurements of devices with integrated aluminum disks in this geometry reveal that neither the optics or mechanics are degraded by the presence of the metal. Future integration of bias and drive fields into our cryogenic system will enable measurements of the dynamical modes [2] of single superconducting vortices [119], and even paramagnetic resonance of trapped electrons in the silicon device itself. With this near-quantum limited torque sensitivity, one can imagine a host of new experiments forthcoming.

- Chapter 5 -

MAGNETIC ACTUATION AND FEEDBACK COOLING OF A CAVITY OPTOMECHANICAL TORQUE SENSOR

Our virtues and our failings are inseparable, like force and matter. When they separate, man is no more. - *Nicolai Tesla*

Following up on the optomechanical torque sensor at low temperatures — yielding remarkable torque sensitivities of 2.9 yNm/$\sqrt{\text{Hz}}$ thermalized at 25 mK, the next logical step is to demonstrate the application of hybrid optomechanical systems, namely torque magnetometry, to elucidate properties of nanoscale magnetism. Although I have successfully fabricated a prototype of aluminium-embedded optomechanics, which are of special interest for mesoscopic superconductivity studies, incorporating orthogonal magnetic fields was not available at the time. Here, I studied the classical signature of a ferromagnetic system, where torques are generated for a magnetized sample in a magnetic field. From this, our optomechancial system shows great field sensitivity of 150 nT/$\sqrt{\text{Hz}}$ and that we can extract material properties of an iron film. Mathematically, the responsiveness of the torsional resonator to magnetic actuation is simply,

$$\boldsymbol{\tau} = \boldsymbol{m} \times \mu_0 \boldsymbol{H}, \tag{5.1}$$

where $\boldsymbol{m}$ is the magnetic moment and μ_0 is the vacuum permeability, and $\boldsymbol{H}$ is the external magnetic field. Maxmimum torque occurs when the magnetization is orthogonal to the field direction. Rather than using an external DC field, the iron film is magnetized during its deposition step and is shaped as a high-aspect-ratio needle to sustain magnetization along x axis. By driving the AC field in the z-direction a torque is generated toward y, where our sample is designed to detect this torque (recall in Fig. 1.1a). Consequently, our system is a great field sensor and is a great platform to study material properties of magnetism. Also in a feedback-loop, I was able to demonstrate active-damping of the torsional mode down

to 12 K, proving the point made previously, that active cooling does not improve its torque sensitivity. I acknowledge that this device is not the first optomechancial field sensor [49], but it is the first torque magnetometer ever made with cavity optomechanics. This chapter is based on the manuscript [120].

§ 5.1 Introduction

While the field of cavity optomechanics has enabled remarkable advances in measuring and manipulating nanomechanical resonators at, or approaching, their quantum limits [24; 58], the most attractive applications of optomechanics require integration with one or more additional systems [121]. For example, the first definitive test of quantum behaviour in a mechanical resonator was enabled by integration with a superconducting qubit [8]. Further experiments have demonstrated coupling between optomechanical resonators and atomic gases [122], superfluids [116], and magnetic materials [49; 22], with the possibility of coupling to small numbers of spins [123; 124; 125; 126] and even biological samples [127]. Such hybrid systems are potentially the key to microwave to telecom wavelength conversion at the quantum level,[128] and enable ultra-sensitive measurements of nano- and mesoscale samples [2].

Unfortunately, most optomechanical systems are not amenable to integration with external samples. For example, two of the most impressive architectures for cavity optomechanics – the optomechanical crystal [58] and the superconducting membrane [24] – are particularly difficult to directly integrate with condensed matter systems. In an optomechanical crystal, the optical mode significantly overlaps with the mechanical motion [58] – providing good optomechanical coupling but difficulty in placing a secondary system onto the mechanics without adversely affecting the optical mode. Likewise, the membrane resonators used with superconducting microwave cavities have extraordinarily small capacitor gaps and are highly tensioned [24], neither of which are compatible with integration of an additional condensed matter system onto the mechanical membrane. There remains a need for carefully-designed structures to allow for useful hybrid integration, such as the open geometry of 3D microwave cavities [129], fabrication out of the condensed matter system under study [123; 125; 126], or – as we use here – a modular structure of separate optical and mechanical components with tailorable coupling.

Here, we demonstrate integration of a mesoscale ferromagnetic needle with a cavity optomechanical resonator, and show that this hybrid system can be used for magnetic field

sensing, with a thermal limit of 0.12 A m^{-1} (150 nT); quantitative determination of the magnetization of the needle; and magnetic feedback cooling of the mechanical mode from room temperature to below 12 K – representing the first demonstration of feedback cooling with a magnetic cavity optomechanical system.

5.1.1 Torque magnetometry

I have a keen interest in torque magnetometry for on-chip devices. In some situation, low frequency micromechancial cantilevers achieved better stability and resolution for atomic force microscopy and scanning probe microscopy in ambient or in liquid environment using positive feedback (or amplification), where the resolution in mass sensing for biological or chemical sensors improved [130; 131]. As precision measurements are essential to our understanding of fundamental laws, such as magnetism, this device has been engineered to drive the torsional mode effectively, and to test the feedback technique to manipulate the amplitude of the torsional mode.

§ 5.2 Experiment

5.2.1 Hybrid device design

One of the main considerations in the design of hybrid systems is taking advantage of the best properties of the individual systems, without sacrificing their performance during integration. Hence, we have chosen to directly integrate a magnetic structure onto our mechanical resonator. The architecture of our magneto-optomechanical system is shown in Fig. 5.1. The mechanical structure, with a low effective moment of inertia (see Fig. 1b), is separated from the evanescent field of a WGM optical cavity by an 87 nm vacuum gap. A platform for the magnetic sample was designed near the end of the torsion arm, amplifying the magnetic actuation of the torsional resonator [68], yet is sufficiently far from the evanescent field of the WGM such that its optical properties are unaffected ($Q_{\mathrm{opt}} = 5.3 \times 10^4$). One main difference is the shape of the magnetic structure, needle instead of the disk, to preserve magnetization in a preferential direction. On this platform we have deposited a ferromagnetic sample, which enables the mechanical motion to be driven, amplified, or dampened, by an AC external magnetic field.

The simulation in Fig. 5.1c shows agreement of torsional mode at 7.2 MHz, where we extracted the effective mass ($m_{\mathrm{eff}} = 0.45$ pg) and the moment of inertia ($I = 4.4$ pg·μm^2).

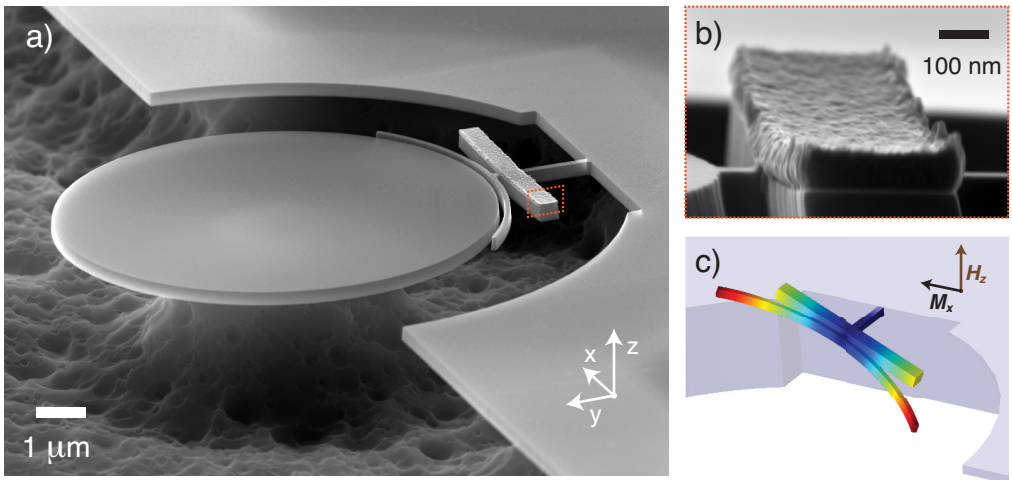

Figure 5.1: **Design of a hybrid iron-needle torque sensor** (a) Scanning electron microscope (SEM) image, tilted to 70 degrees, shows the optomechanical torque sensor, integrated with a magnetized Fe-needle deposited near the torsion-arm. The tri-layer of Cr, Fe, and Cr has a total thickness of 83 nm (4.39 nm long and 410 nm wide) as seen in the (b) cross section. (c) Simulated torsional mode at 7.2 MHz can be driven by out-of-plane magnetic fields as a resulting torque along the torsion rod (y-axis).

The device in Fig. 5.1a shows the best device, where the diameter of the microdisk was 8.8 μm, and the torsion arm encapsulates the microdisk by an angle of 86 deg (or 1.5 rad). The Fe-needle has a length of 4.39 μm and a width of 0.41 μm and is placed as near to the optical disk without affecting the optical scattering from the evanescent field.

5.2.2 Nanofabrication

Two unique features are added to the previous recipe: magnetizing the iron film during the deposition, and the use of VHF to avoid the wet-etch problem of magnetic films. Starting with a 250 nm SOI chip, two EBL steps were involved: first, to pattern the silicon device using the same recipe mentioned previously. This is followed by a second EBL process, with careful alignment, in order to define area for subsequent metal deposition. Electron-gun evaporation was used to deposit an 83 nm thick trilayer of Cr, Fe, and Cr. The purpose of the first 8 nm thick Cr layer is for adhesion to the silicon, whereas the last Cr layer, of equal thickness, serves as a capping layer to protect the iron from oxidation. During the deposition, a rare-earth magnet (NbFeO) was placed directly underneath the 5 mm $\times$ 10 mm SOI chip to preferentially orient the iron magnetization direction along the length of the needle (x-axis in Fig. 5.1a). The magnetic field strength at the position of the device during deposition was measured to be 94 kA m^{-1}.

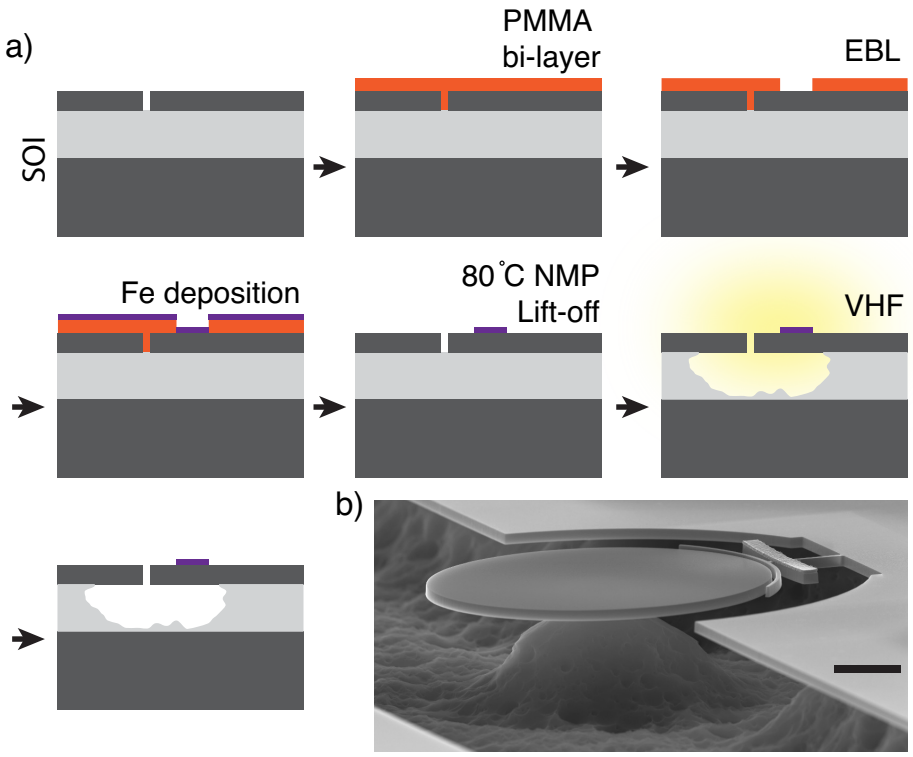

Figure 5.2: **Iron-needle fabrication** (a) Beginning with a silicon-on-insulator chip with device thickness of 250 nm, fabrication has two main e-beam lithography steps. First e-beam lithography is used to pattern the optomechanical layout as outlined in Fig. 1a using a positive ZEP520a e-beam resist and a 30 kV e-beam lithography system (RAITH-150TWO). Following a plasma etch (ICP-RIE), a second e-beam lithography process, with careful alignment, patterns a PMMA bi-layer resist in order to make windows for metal deposition. An e-gun evaporator was used to deposit series of Cr, Fe and Cr. The purpose of the first Cr layer, 8 nm in thickness, is for adhesion, where the last Cr layer, with equal thickness, is a capping layer to protect Fe from oxidation. A careful deposition took place in a electron-gun evaporation system in a low vacuum of 1.2×10^{-7} Torr. A permanent magnet is placed underneath the 5 mm $\times$ 10 mm chip during the deposition of Fe (99.9999%) to permanently magnetize the iron. After a lift-off process in N-Methyl-2-pyrrolidone (NMP) solvent, the chip is placed in a vapour HF system (MEMStar Vapour HF) to etch the sacrificial layer (SiO_2) - avoiding the problem of stiction and Fe-etch. Note that this was a modified process over Ref. [85] to better handle small gaps and achieve better alignment through the use of the VHF etcher. Consequently, this improved method has full yield on all of the devices. (b) A tilted view of the optomechanical structure is shown with scale bar of 2 μm.

After lift-off of the PMMA and deposited metal using N-Methyl-2-pyrrolidone (NMP), the chip is placed in a vapour HF system (MEMSstar) to etch the sacrificial SiO_2 layer.

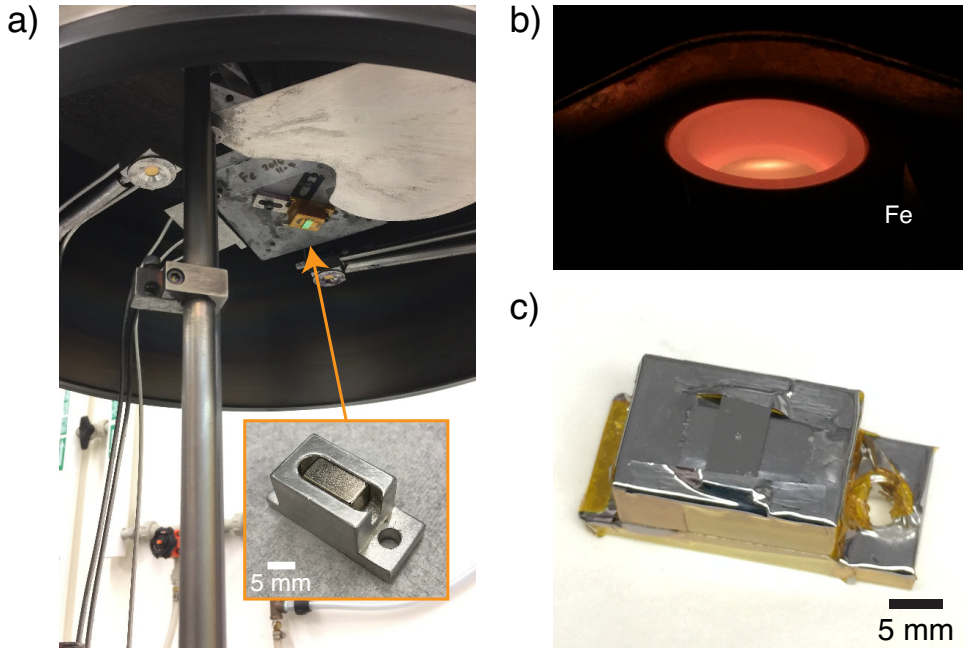

Figure 5.3: **Iron deposition** (a) A picture of inside of the e-beam evaporator, where the sample is mounted on a rectangular cuboid permanent magnet. The chip is oriented such that the film is magnetized along the needle design. (b) The iron source on a copper crucible, heated via magnetically steered electron gun to evaporate the material. (c) The tri-layer of 83 nm Cr-Fe-Cr is deposited on the chip, ready for a lift-off process.

Use of the HF vapour etch, instead of a buffered oxide etch, simultaneously avoids both problems of stiction and etching of the iron sample.

5.2.2.1 Fabrication recipe for hybrid NOMS

10. Resist spin

    - Place the chip on the smallest chuck in the Laurell spinner in the fumehood (Brewer spinner also works)
    - Put 2 droplets of PMMA495k-A2 on the chip using a pipette such that they are contained on the chip without spilling on the edges
    - After waiting 1 minute, spin the resist using the recipe "PK_PMMA"
        - spin: 500 RPM, ramp: 100 RPM/s, time: 10 s
        - spin: 4000 RPM, ramp: 350 RPM/s, time: 45 s

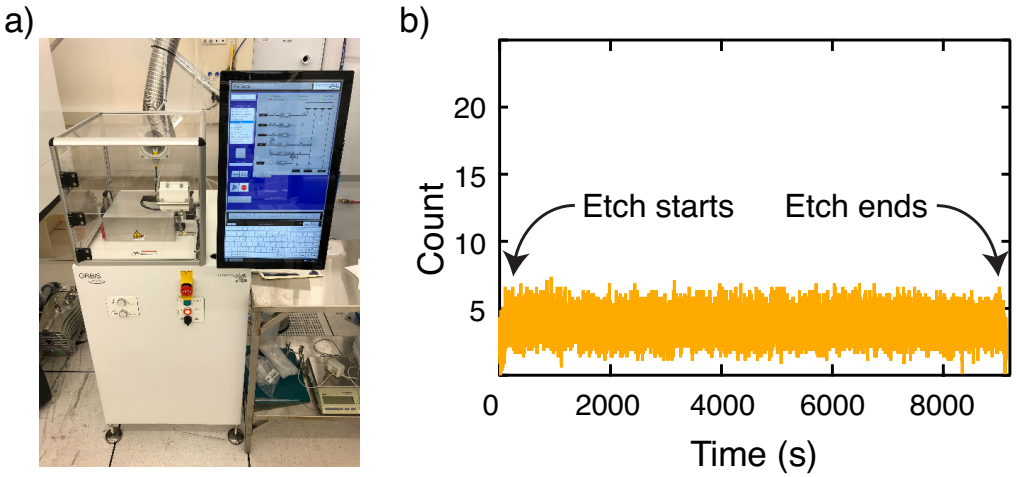

Figure 5.4: **VHF system at nanofab** (a) A photograph of the vapour HF etcher, Memsstar Orbis Alpha, where the chip is placed inside the chamber to etch-release the torsional structures without damaging the iron film. (b) An IR detector monitors the by-product of the etched material (SiF_4) where the uniform etch-rate is performed throughout the 9000 s. Due to the small chip used, the count-rate is low but discernible from start to finish.

- Inspect the back-side of the chip (soak cleanroom-compatible Q-tips with acetone/IPA to wipe out excess resist on the back-side
- Bake the chip at 180°C for 5 minutes followed by a 2 minutes waiting period (cool-down/hydration period)
- Repeat the spin/bake process for PMMA950k-A2 resist
- This should give a total thickness of $\sim$ 120 nm near the centre ($\sim$ 55 nm each)
- Depending on the desired thickness for deposition, four layers can be used, two PMMA450k-A2 layers followed by two PMMA950k-A2 layers, which gives total thickness of $\sim$ 190 nm ($\sim$ 95 nm each)

11. EBL (post-alignment)

- Scratch the bottom left corner of the chip using a diamond tip prior to loading in RAITH-150Two
- Temporarily, define the bottom left corner (U,V) = (0,0) and perform an angle alignment
- Focus on a particle near the scratched corner with 10 kV EHT (accelerating voltage) and 10 μm (aperature)
- Perform a write-field alignment until four zero's or nine's are obtained

- Perform a three-point-alignment (U,V,W) in local coordinates
  - For example, corners of the 1000 μm $\times$ 1000 μm design outline was used (0,0), (880,60), and (60,980) for the file in the appendix
- Record the beam current in units of pA ($\sim$ 19 pA)
- Set dose at 170 μC/cm^2
- Adjust the curve-step as 10 nm and area-step as 20 nm
- Run the position-list file (.pls format), which includes layer 63 boxes for beam-alignment (four 1 μm $\times$ 1 μm near the centre of the write field, followed by exposing each write field GDSII layout file (.csf format)
  - This step is similar to the writefield alignment on a particle, except that the layer 63 squares are manually aligned to the patterned boxes (the method in Ref. [85] requires larger alignment boxes, 5 μm squares, to resolve features of a thicker PMMA resist)
- Develop in MIBK:IPA (1:3) for 60s, followed by IPA for 20s, and final rinse in DH_2O for 15s

12. e-gun evaporation (CCIS phase1 L1-330 Prof. Meldrum's lab)

- Base pressure: 2.9 $\times 10^{-7}$ Torr
- Cr deposition
  - Target: 7 nm
  - Rate: 0.5 Å/s
  - Pressure: 9.0 $\times 10^{-8}$ Torr
  - Current: 0.05 A
- Fe deposition
  - Target: 45 nm
  - Rate: 0.4 Å/s
  - Pressure: 1.2 $\times 10^{-6}$ Torr
  - Current: 0.14 A
- Cr deposition: same as the first layer
- Between each deposition, 1 hr cool-down was needed to not heat the sample
- Because the chip was mounted on top of the NdFeB magnet, as seen in Fig. 5.3c, to magnetize the sample during evaporation, the deposition rate was faster than the thickness monitor — giving a total thickness of (83 $\pm$ 8) nm, instead of 44 nm in this case (from Alpha-Step IQ)

13. Lift-off

    - Soak the chip in acetone for 45 min, where the bulk of iron is removed by a gentle stir
    - Final cleaning in heated NMP at 75 °C for 30 min, followed by a 30 min room-temperature NMP (fresh solution)
    - Here a magnetic stir-bar is not used as it strips the iron film destructively

14. VHF (MEMSTAR)

    - Processed for 2 hrs and 30 min
        - HF rate: 40 sccm
        - N_2 rate: 20 sccm
        - H_2O rate: 5 sccm
        - Pressure: 12 mTorr
    - Note that the vapour etch, by nature, is not very uniform compared to the wet-etch, where increasing the etch rate (increasing H_2O rate and decreasing VHF rate) gives very erratic profile; hence, the etch rate is kept low at $\sim$ 20 nm/min to keep consistent undercut throughout the chip (see Fig. 5.2b)

Parameters	Pump	N_2	H_2O/HF	Ramp	Main-etch	Purge
Pressure (Torr)	0.5	15	30	11.5	12	15
N_2 (sccm)	10	20	20	20	20	50
H_2O (sccm)	-	-	5	5	5	-
HF (sccm)	-	-	40	40	40	-

Table 5.1: The etch parameters for Memsstar orbis alpha were selected such that the rate is moderate ($\sim$ 20 nm/min), allowing a somewhat-uniform etch throughout the chip. Consequently, the yield is near perfect since the alignment can be done prior to the oxide etch rather than after. Note that the purge steps in the beginning and at end are there to ensure safety in handling toxic gases. After the introduction of VHF, 9000 seconds are processed for ≤ 3 μm etch. Here a default step of field-etch is omitted for consistency and uniformity

This processflow is a modified recipe over Ref. [85], which gives a better method for ease alignment by substituting VHF in place of wet-etch. By doing so, the lift-off process can be done prior to the undercut, where the yield is nearly 100% since the SOI heterostructure is intacted during the lift-off. In addition, the bi-layer e-beam resist can be coated much thinner, giving a better contrast during alignment. The above recipe begins with step 10, where steps 1 through 9 follow the exact recipe in Sec. 4.3.2.1. One of the advantages, as we will see later, is that the VHF does not degrade the quality of the magnetic film. The

four parameters, pressure, oxygen, nitrogen, and HF, were tested to control the etch rate of the buried oxide. The IR detector inside the VHF chamber detects the amount of SiF_4 generated by the etch as a monitoring process, shown in Fig. 5.4b. Since we are using a small 10 mm $\times$ 5 mm chip, the volume of the chemical product is extremely small compared to a full wafer — making it harder to resolve the etching process. However, as indicated by a nice flat line in Fig. 5.4b, the etch process is stable and slow. Here, I have removed the field-etch step, a default process prior to the main-etch to remove native oxide, which sometimes cause inconsistent results by the blast of field-etch. As long as the chip was immaculate prior to VHF, the results were highly consistent for the same recipe. Specific steps and parameters used for the etch is listed in table 5.1. It is also worth mentioning that the metallic needle cannot be designed arbitrarily long, as the stress induced during deposition, despite the best efforts to minimize heat, causes deformation of the silicon resonator, apparent in Fig. 5.2.

5.2.3 Experimental apparatus

Our experimental apparatus follows the same optomechanical tune-to-slope detection scheme demonstrated previously [48; 68] with the exception that we added microwave transmission lines to apply magnetic fields in the system, allowing feedback control to the torsional mode as illustrated in Fig. 5.5a. A dimpled tapered fibre, comparable to the previous fibres (radius of curvature of 70 μm) touches the optical microdisk for stability and over-coupling [89]. All of these components, including a printed-circuit-board (PCB) with two axes of orthogonal magnetic drive coils (Fig. 5.5b) [2], are housed in a room-temperature optical-access vacuum chamber of 10^{-5} Torr. While coupled, the AC signal from the photodiode gets amplified and power-split (50:50) to the DAQ and to the feedback loop, passing through a band pass filter (6.7 $\sim$ 11 MHz) and a 37 dB amplifier. We calibrate the total phase of our system using a reference output from the high-frequency lock-in amplifier (Zurich Instruments HF2LI). The lengths of the cable were adjusted accordingly to control the feedback phase. The lock-in amplifier can also drive ac currents through the z-axis excitation coil.

§ 5.3 Results and discussion

The device presented here has an optomechanical coupling of $g_0 = Gz_{\mathrm{zpf}} = 38$ kHz, where the mechanical zero-point fluctuations are given by $z_{\mathrm{zpf}} = 51$ fm. The reasonably large g_0 enables measurement of the mechanical motion down to an imprecision noise-floor of 25 fm $\mathrm{Hz}^{-1/2}$. It is worth noting that, despite the reasonably large g_0 of our device, optomechanical damping is insignificant compared to feedback damping. For example, at the highest optical powers used here, feedback cooling results in an increased dissipation of $\Gamma_{\mathrm{fb}}/2\pi = (\Gamma_{\mathrm{tot}} -$

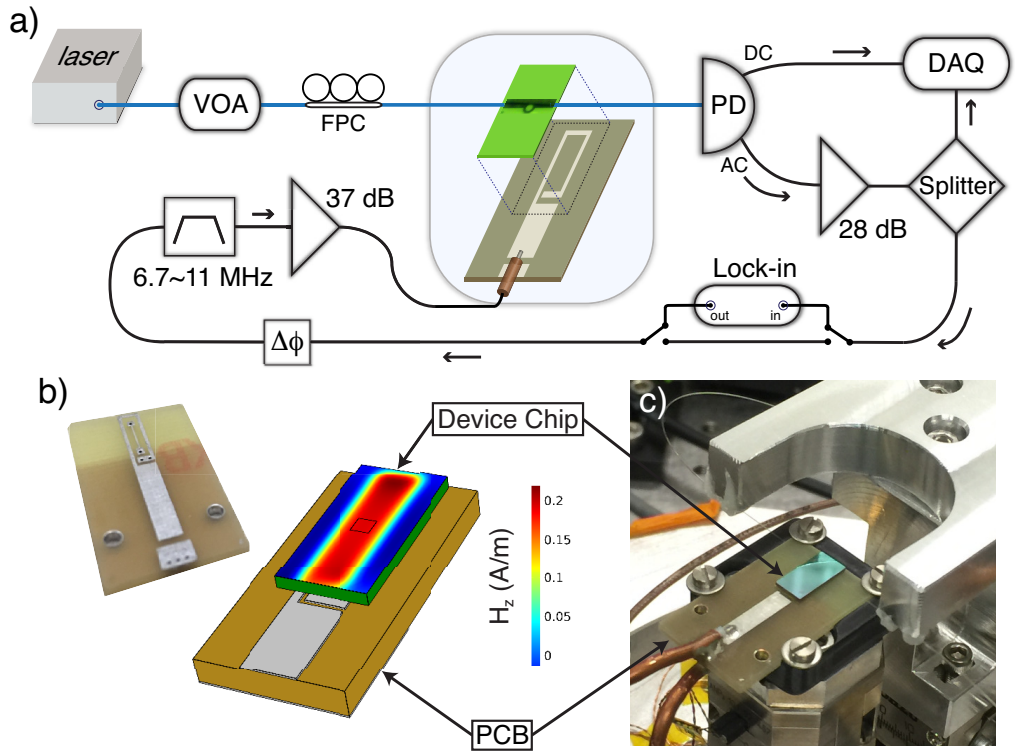

Figure 5.5: **Magnetic-needle apparatus** (a) The schematic of the optomechanical transduction and the feedback apparatus using the transmission lines. The phase of the feedback signal is calibrated by the lock-in amplifier and is varied by the length of the coax cable. (b) A photograph (left) and simulation (right) of the out-of-pane magnetic field along the z-axis at the top surface of the device chip, with 1 mA of applied current. The device position is indicated by the black square, chosen for large field strength and relative field uniformity. (c) A photograph inside the chamber depicts the contents inside the vacuum chamber: the optomechanical chip, the PCB drive chip, and the dimpled tapered fibre.

$\Gamma_i)/2\pi \approx 27,000$ Hz, whereas the maximum optomechanical damping that is possible is just $\Gamma_{om}/2\pi = 29$ Hz for our device parameters [57].

5.3.1 Magnetic actuation

As seen in Fig. 5.1a, the magnetic moment is along the x-axis. We apply an orthogonal ac magnetic field along the z-axis that generates a torque along the y-axis, *i.e.* the torsional axis of the resonator. We first characterized the linear driven response without any feedback using the device shown in Fig. 5.1a. The output current from the lock-in amplifier was calibrated to the out-of-plane magnetic field ($\boldsymbol{H_z}$) using a Tektronix CT-2 current probe and then swept

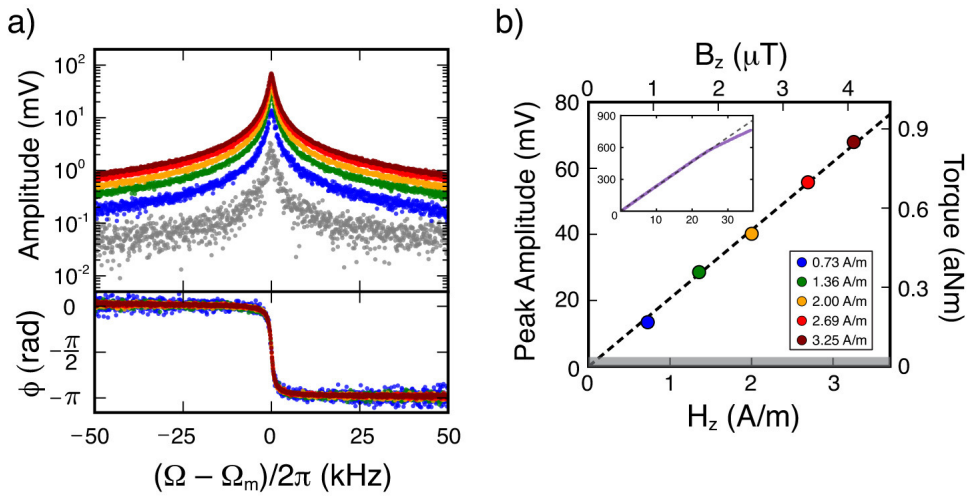

Figure 5.6: **Magnetic actuation and sensing** (a), Amplitude of the thermomechanical (grey) and magnetically actuated (coloured) torsional resonance, with corresponding phase of the driven traces. Colours in (a) correspond to the drive magnetic field plotted in panel (b), which shows the relationship between the peak mechanical signal amplitude (left axis) and calibrated torque (right axis), versus the magnetic drive. The grey band represents the thermomechanically-limited minimum field sensitivity of 0.12 A m^{-1}, corresponding to a thermal torque of 32 zNm. Inset, with the same axes, shows the deviation of the continuously-measured peak response (purple) from the linear fit extrapolated from low-field (dashed). Above 25 A m^{-1} the optical resonance is shifted due to heating from the drive chip.

in frequency with a bandwidth of 100 Hz to obtain a raw mechanical spectrum, and its phase response, Fig. 5.6a. The linear relationship of peak amplitude as a function of mechanical frequency still continues until 25 A/m (31 μT), shown inset to Fig. 5.6b, where the drive chip starts to heat the optomechanical chip causing the optical resonance to drift. The minimum field sensitivity, limited thermally, was 0.12 A/m (150 nT) out-of-plane, which is on par with the microtoroid optomechanical magnetometer [49]. In addition, the properties of the magnetic film can be inferred by calibrating the field-driven torque as a function of known magnetic fields to extract magnetic moment from its slope. The responsivity (slope) is 168 $\pm$ 2 μrad/(A/m). Note that lowering the temperature of the resonator would improve its dynamic range and sensitivity [68]. As we can see in Eqn. 2.20, such an improvement stems from both the lowering thermal torque noise and the intrinsic damping rate at low temperatures, although the exact mechanism for decreased mechanical damping is complex [132].

Using the thermomechanical calibration method outlined previously, we determine the measured thermal torsional motion of the mechanical resonator, and hence the thermal

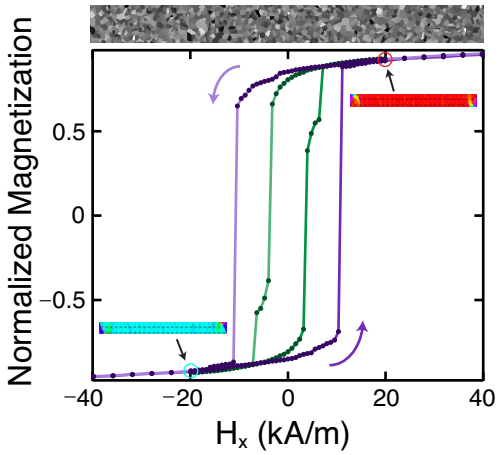

Figure 5.7: **Magnetic simulation** Simulated magnetization (normalized to M_s) hysteresis with in-plane domain structure at circled points. At high fields the needle is nearly saturated, with triangular domains at each end. As the field is lowered these domains move towards the centre, reducing the net magnetization. For a uniform iron film (green trace) at zero field, the remanent magnetization corresponds to 79% of the saturation moment. Adding polycrystalline grains, as shown above the panel, increases the remanent magnetization to 85%, as seen in the purple trace.

torque applied to it. The right axis of Fig. 5.6b shows the calibrated torque measured at the mechanical resonance frequency, with a minimum (thermal) torque of 32 zNm. In addition, the straight line fit to the data in Fig. 5.6b using Eqn. 5.1 allows extraction of the total magnetic moment of the ferromagnetic needle, $|\boldsymbol{m}| = (2.06 \pm 0.02) \times 10^{-13}$ Am^2, or equivalently, $(2.22 \pm 0.02) \times 10^{10} \mu_B$. Taking into account the measured volume of the iron portion of the needle, $V = (1.21 \pm 0.09) \times 10^{-19}$ m^3, we find a magnetization, M of 1710 ± 140 kA/m. This is an excellent agreement with the room temperature saturation magnetization of bulk iron, $M_s^{\text{iron}} = 1710$ kA/m [133]. Furthermore, the large measured magnetization suggests that domain wall pinning — resulting from polycrystalline grains — plays an important role, as it serves to increase the remanent magnetization above that of a uniform film.

5.3.1.1 Magnetic simulation

Here, I acknowledge the work of Fatemeh for her simulations, where a GPU-accelerated open-source program, mumax (version 3.9), was used to simulate the zero-temperature properties of a ferromagnetic needle with the as-fabricated dimensions of $4390 \times 410 \times 67$ nm^3 and the bulk properties of iron: exchange stiffness constant $A_{ex} = 13.3$ pJ m^{-1} and the $T = 0$ saturation magnetization $M_s = 1740$ kA m^{-1} [133], with a cell size of $10 \times 10 \times 6.7$ nm^3. While

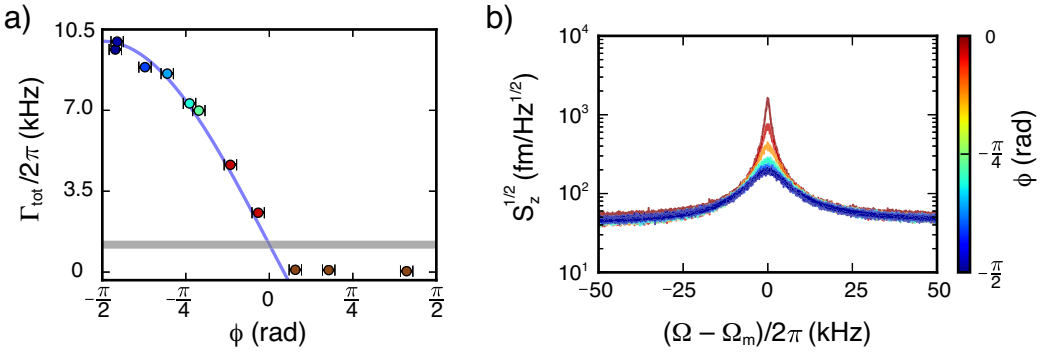

Figure 5.8: **Magnetic feedback cooling and self-oscillations** (a) The total dissipation, $\Gamma_{\rm tot}/2\pi$, as a function of phase in the feedback loop, shows excellent agreement with a fit to Eqn. 5.2 (blue curve). The optical power is 4.1 μW at the device. Error bars represent the standard deviation in the phase noise, as measured by the Zurich lock-in amplifier. Maximum damping occurs at $-\pi/2$, and self-oscillation occurs for measured phases greater than zero (brown). The grey horizontal line shows the intrinsic dissipation, $\Gamma_{\rm i}/2\pi = 930$ Hz, identical to the total dissipation at $\phi = 0$. (b) The same colour-coded data represent in terms of calibrated displacement spectral densities, for $\phi < 0$.

the simulation does not take into account the effects of temperature, hence the $T = 0$ value of the saturation magnetization is used, at room temperature the saturation magnetization is expected to be reduced by 2% to 1710 kA m^{-1} due to spin waves [134]. Magnetocrystalline anisotropy is neglected on account of the large aspect ratio, which makes shape anisotropy dominant [135].

The hysteresis loop starts at a large positive field, 80 kA m^{-1}, and the field is swept to -80 kA m^{-1}, finally returning to the original positive field. A portion of the hysteresis loop, from -40 to 40 kA m^{-1} is presented in Fig. 5.7. Hysteresis loops were simulated for both a uniform film, and one with a polycrystalline grain size of 40 nm, with a random variation of M_s by $\pm$10%. The insets to Fig. 5.7 show the corresponding magnetization states at $\pm$ 20 kA m^{-1} for a granulated structure.

5.3.2 Feedback damping and amplification

Beyond using an AC current source for magnetic actuation, we can also use the measured mechanical signal to amplify or dampen the resonator motion. This type of feedback has been used in the cantilever sensing community, where amplification allows cantilever motion to be detected in highly damped conditions such as liquid environments [131]. When lower-

ing the mode temperature, it is important to note that feedback cooling (or amplification) cannot increase the torsional sensitivity of the resonator, as the quality factor compensates the reduction of temperature. To test the performance of feedback amplification and cooling in our magneto-optomechanical system, we implement the scheme shown in Fig. 5.5a. Half of the ac signal, measuring the thermomechanical motion, is sent to a high-frequency data acquisition system, while the other half is phase shifted, bandpass filtered around the mechanical resonance of interest, and amplified, before being sent to the z-axis drive coil. Here, a lock-in amplifier is used to calibrate the total phase in the system. The phase shift is particularly important, as can be seen from the equation of motion for a damped, driven harmonic oscillator subject to a feedback force. From Eqn. 2.30, the first term on the right hand side, $\tau_{\rm th}/I_{\rm eff}$, is proportional to the thermal force acting on the mechanical resonator, while the second, $-g_{\rm fb}\Gamma e^{i(\phi+\pi/2)}(\dot{\theta}+\dot{\theta_n})$, is related to the applied feedback force. Here $g_{\rm fb}$ is the gain of the feedback loop, ϕ is the measured phase difference between the drive and the displacement, and $z\theta_{\rm n}$ is the measurement noise [136; 137]. The resulting total mechanical dissipation can therefore be written as

$$\Gamma_{\rm tot} = \Gamma_{\rm i}(1 + g_{\rm fb}\cos(\phi + \pi/2)). \tag{5.2}$$

The phase controls whether the feedback gain results in cooling ($\phi = -\pi/2$), amplification ($\phi = \pi/2$), or does not modify the damping rate ($\phi = 0$). In Fig. 5.8, we show how the measured dissipation, $\Gamma_{\rm tot}$, is affected by the phase in the feedback loop. These measurements were performed with a moderate optical power of 4.1 μW at the microdisk, resulting in a feedback gain of $g_{\rm fb} = 7.4 \pm 0.1$, extracted from fitting Eqn. 5.2 to the $\phi < 0$ data in Fig. 5.8a. We note that the gain was kept moderate in these measurements to prevent overloading of the electronic components in the region of feedback amplification, $\phi > 0$ data in Fig. 5.8a, where the mechanical linewidth narrows and results in induced self-oscillation [138].

5.3.3 Limits on active cooling

To demonstrate our full feedback cooling efficacy, we increase the optical power at the microdisk to 18 μW, which results in a shot-noise-limited noise floor of $\sqrt{S_z^{\rm imp}} = 25$ fm Hz$^{-1/2}$. This optical power produces our largest feedback gain, as shown in Fig. 4, increasing the total dissipation from $\Gamma_{\rm i}/2\pi = 930$ Hz ($Q_{\rm m} = 7{,}760$) to $\Gamma_{\rm tot}/2\pi = 28{,}000$ Hz ($Q_{\rm m} = 260$). Evaluating Eqn. 5.2 at $\phi = -\pi/2$, a quantitative value for the feedback gain can be determined as $g_{\rm fb} = \Gamma_{\rm tot}/\Gamma_{\rm i} - 1 = 29$. Furthermore, we can infer the reduced mechanical mode temperature using the relation: [110; 136]

$$T_{\rm fb} = \left(T + \frac{m_{\rm eff}\Omega_{\rm m}^2\Gamma_{\rm i}g_{\rm fb}^2 S_z^{\rm imp}}{4k_{\rm B}}\right)\frac{1}{1+g_{\rm fb}}, \tag{5.3}$$

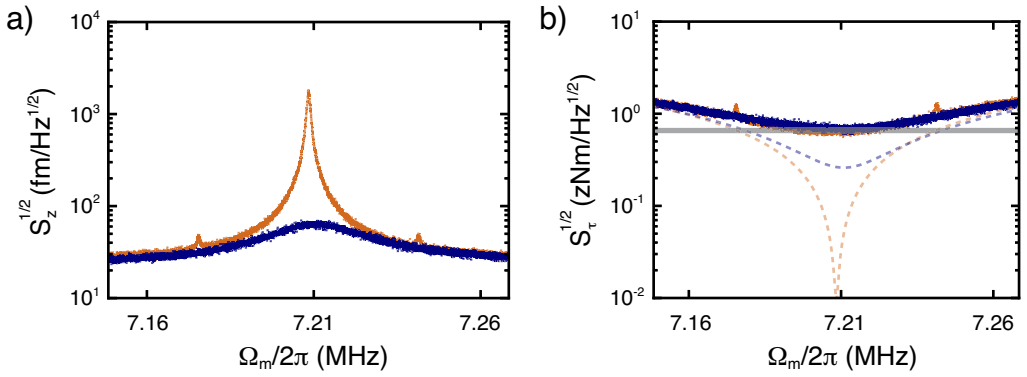

Figure 5.9: **Optimal feedback cooling and torque sensitivity** (a) Increasing the power in the optical cavity enables sensitive mechanical transduction, lowering the imprecision noise floor to 25 fm/$\sqrt{\text{Hz}}$ (orange trace). The theoretical minimum temperature achievable with this noise floor is 8.6 K, and with a feedback phase of $-\pi/2$ and a feedback gain of 29 we find we are able to cool to 11.6 K (blue trace). (b) The calibrated torque sensitivity before (orange) and after (blue) feedback damping to a Q_m of just 260. Dashed traces correspond to torque sensitivities in the absence of thermal noise, which is given by the grey line. The device maintains a minimum torque sensitivity of 0.6 zNm/Hz, regardless of whether or not feedback is applied.

for which we find we can cool from room temperature to a value of $T_\mathrm{fb} = 11.6 \pm 0.1$ K. Note that the second term in Eqn. 5.3 arises due to the fact that feeding back imprecision noise onto the resonator will act to heat the mechanical mode. The reduced mode temperature calculated from Eqn. 5.3 is in reasonable agreement with that determined from the relative areas under the power spectral densities, which gives a mode temperature of 13.17 ± 0.02 K.

Comparing with the theoretical minimum achievable temperature using feedback cooling, which for high-temperatures ($k_\mathrm{B}T \gg \hbar\Omega_\mathrm{m}$) and large gain ($g_\mathrm{fb} \gg 1$) is given by

$$T_\mathrm{min} = \sqrt{\frac{m_\mathrm{eff}\Omega_\mathrm{m}^2\Gamma_\mathrm{i}TS_z^\mathrm{imp}}{k_\mathrm{B}}}, \tag{5.4}$$

we find $T_\mathrm{min} = 8.6$ K for the values reported here. Note that this minimum temperature would be reached at a feedback gain of

$$g_\mathrm{fb,opt} = \sqrt{\frac{4k_\mathrm{B}T}{m_\mathrm{eff}\Omega_\mathrm{m}^2\Gamma_\mathrm{i}S_z^\mathrm{imp}}}, \tag{5.5}$$

providing the optimal balance between cooling the mechanical motion via the cold damping feedback force and heating by feeding noise back onto the mechanical resonator. We calculate $g_{\mathrm{fb,opt}} = 68$ using the experimental parameters from the data in Fig. 5.9, approximately a factor of two above the measured value. The result is a reduced temperature 3 K above the fundamental limit for the experiment performed here.

It is worth noting that, as stated earlier, the torque sensitivity is not improved (or substantially degraded) by feedback cooling. We show in Fig. 5.9b the calibrated torque sensitivity using the room temperature data before cooling, and after cooling (damping) the torsional mode to 11.6 K. Despite dramatically different dissipation rates and mechanical mode temperatures, they have identical torque sensitivities, with a minimum value of 0.6 zNm/$\sqrt{\mathrm{Hz}}$ – a factor of two better than the only other room temperature cavity optomechanical torque sensor with an integrated nano-magnetic sample [22].

§ 5.4 Conclusion and outlook

In summary, we have successfully integrated a ferromagnetic sample with a cavity optomechanical torsional resonator. First, we used this magneto-optomechanical system as a magnetic field sensor with a linear response from 150 nT to 31 μT, and a responsivity of 0.134 ± 0.003 rad/mT. Next, we quantitatively determined the magnetic properties of the magnetic sample, showing the potential of this system for studying mesoscopic condensed matter samples. And finally, we showed that using magnetic actuation, the resonator motion could be driven into self-oscillation or cold-damped to below 12 K. Future experiments could extend measurements to high frequency using torque-mixing [2], low temperatures for superconducting samples and enhanced sensitivity [68], or explore quantum spin tunnelling [139] and exotic magnetic excitations such as those in topological systems [140; 141].

- Chapter 6 -

BROADBAND OPTOMECHANICAL TRANSDUCTION OF NANOMAGNETIC SPIN MODES

An expert is a person who has made all the mistakes that can be made in a very narrow field.

- Niels Bohr

A vortex structure involves a physical parameter that is curling around a singular core and is widespread in nature: a turbulent flow in liquid, order parameter of type-II superconductors, matter density of black holes, and magnetization in two-dimensional ferromagnets. The stable magnetic vortex state, unlike the other examples, can be carefully studied and controlled in an experimental setting as long as the sample is in a ordered state (*i.e.* below the Curie temperature) and the thickness is much less than the diameter of the ferromagnetic disk. Magnetic vortex is one of the most interesting and potentially useful phenomenon in nanomagnetism [142]. A variety of tools have been applied to study the vortex state, and collective spin excitations corresponding to harmonic motion of the vortex, but to-date these tools have measured either strongly driven vortex resonances or have been unable to simultaneously measure static properties such as the magnetization. Here we show that by combining the sensitivity of cavity optomechanics with the technique of torque mixing resonance spectroscopy, we are able to measure the magnetization, in-plane susceptibility, and spin resonances of individual vortices in the low-drive limit. These measurements elucidate the complex behaviour of the vortex as it moves through the pinning landscape of the disk.

§ 6.1 Introduction

Torque magnetometry enabled by micro and nanomechanical resonators has proven to be one of the most useful probes of nanomagnetism. Torsional resonators have allowed the observation of such a phenomenon as real-time creation and annihilation of single magnetic vortices [117], Barkhausen noise from a single defect [47], mechanical ferromagnetic resonance spectroscopy [143], and collective spin modes using the technique of torque mixing resonance spectroscopy (TMRS) [2]. Adding to this the sensitivity of cavity optomechanics, which allows thermomechanical torsional motion to be observed from room temperature [48; 22] down to millikelvin temperatures [68], has the potential to uncover new physics, particularly in the stochastic domain, of nanomagnetism. Here we show that by using a cavity optomechanical torque magnetometer [48] optimized for torque mixing resonance spectroscopy, we are able to observe spin modes in magnetically-soft permalloy disks above 1.1 GHz. By comparing with micromagnetic simulations and direct-torque susceptometry measurements [22], we show that these modes are consistent with the gyrotropic mode [144]-[148] of the vortex sampling the disorder potential of the polycrystalline magnetic disk [47; 149].

Importantly, we are able to track these spin modes at all frequencies, that is we see no drop-outs in the spin resonances, which allows us to follow the behavior of the vortex as it traverses the disk. In future studies, it should be possible to work backwards from these spin modes to recover the energy landscape of the magnetic structure [47]. We also note that this work amounts to conversion of UHF (ultra-high frequency) signals through spin resonances to telecom wavelengths. Such wavelength conversion is a key topic in quantum technology applications [67; 150; 151], and improvements to the existing device architecture may provide a promising route to high-efficiency wavelength conversion [128] through quadruply-resonant (optical, mechanical, spin, and microwave) devices.

§ 6.2 Experiment

The apparatus used for this experiment is near-identical to the previous project with iron-needles, except two AC drive fields (x and z direction) are used to drive and down-mix a gyrotropic disk mode. Fabrication steps are also alike, except that the deposition of Py took place in an ultra-high-vacuum environment (UHV) for a better film quality.

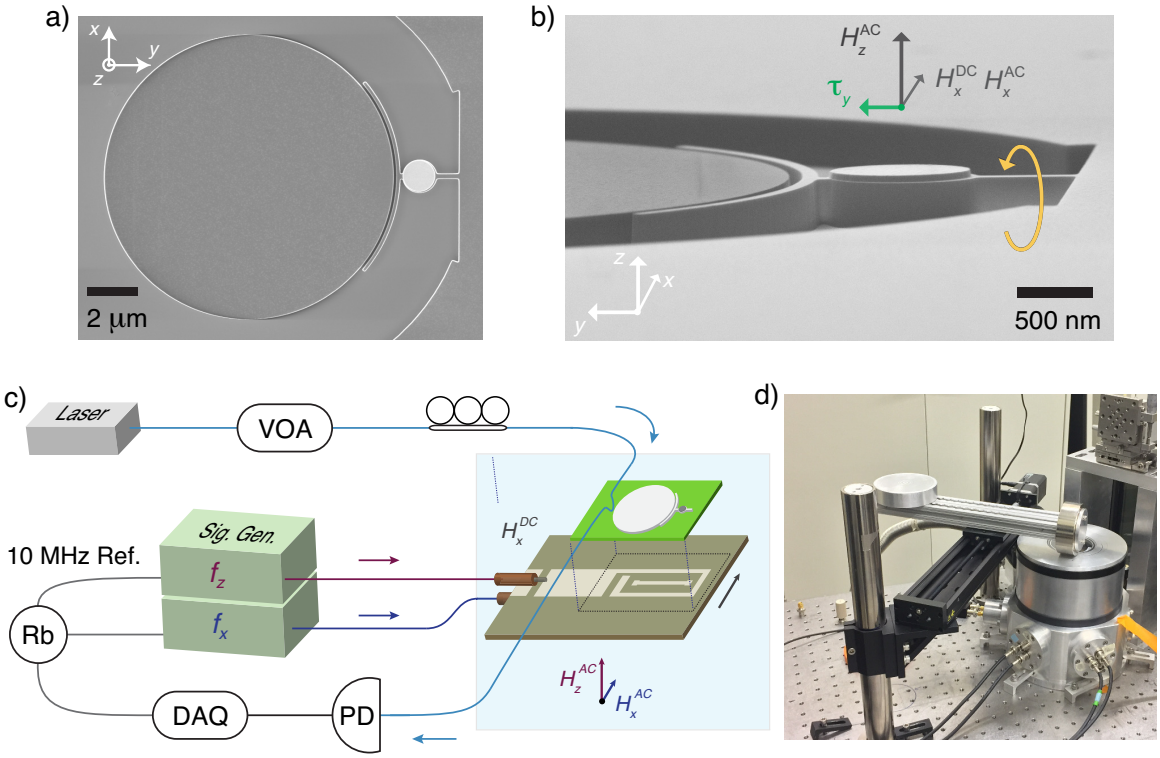

Figure 6.1: **Optomechanical torque-mixing resonance spectroscopy** (a) SEM image of a 1.1 μm diameter permalloy disk fabricated onto a silicon optomechanical torsional resonator. (b) Tilted view of the same image with field directions on the panel. The thickness of Py disk is 50 nm. (c) Schematic showing the optomechanical detection and magnetic drive. Torsional motion is read out through a dimpled-microfibre [89], which monitors an optical resonance of the WGM microdisk. AC magnetic fields are applied via a printed circuit board and driven using two signal generators synchronized to an external rubidium clock. The data acquisition system (DAQ) records the optomechanical signal at the mechanical resonance frequency, also synchronized to the rubidium clock. PD represents a photodiode and VOA a variable optical attenuator. (d) A picture of the apparatus with the permanent magnet on top. After a successful alignment of the dimpled-microfibre and a microdisk, the microscope is removed and replaced with the magnet mount to keep the magnet field direction strongly along the x-axis. Note that the field strength is calibrated using a 3D hall probe prior to measurement.

6.2.1 Hybrid device design

It is important to consider the geometry of the applied magnetic fields and the spin texture of the magnetic structure in this experiment to understand the spin resonance that we observe. To first order, the spins in the magnetically-soft permalloy can be considered to

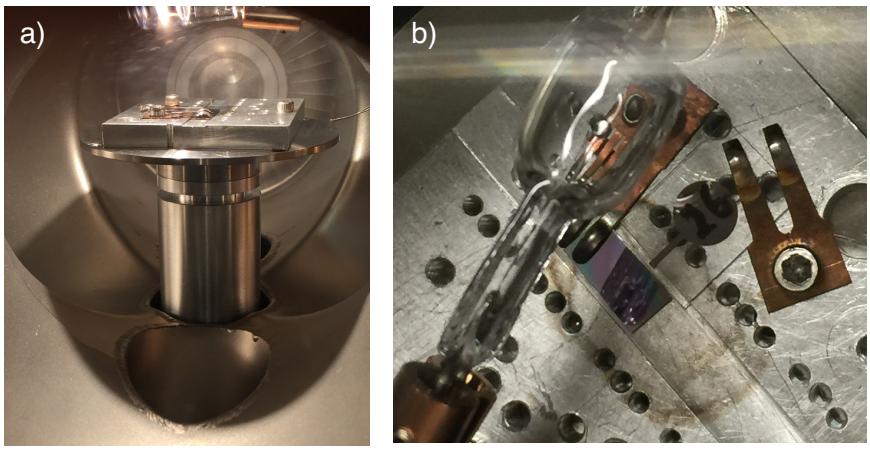

Figure 6.2: **UHV Py evaporator** (a) An inside picture of the UHV evaporator during the pump-down, where the lamp is turned on to bake the deposition chamber. After pumping the chamber with an ion pump for a few days, pressures near 10^{-10} Torr can be achieved in this system. (b) A photograph of the top-view, where the chip and a glass sample is mounted on a holder. A collimated deposition widow is enough to cover the whole chip and a portion of a glass sample, where the thickness of the film can be characterized after the deposition.

point in any direction. Yet in mesoscale structures the magnetization is often dictated by the boundary conditions of the disk, *i.e.* shape anisotropy. In a thin disk, as patterned here, the magnetization lies in the plane – and curls around the boundaries of – the disk, forming a vortex at the center of the disk in zero magnetic field [152]. When a DC magnetic field is applied in the plane of the disk, this vortex is displaced orthogonal to the applied field. For example, when a DC field is applied along the x-axis, the vortex is displaced along the y-axis, increasing the magnetization in the x direction and hence the direct torque measured. An additional AC drive field applied along the x-axis will drive gyration of the vortex in the plane of the disk. This gyration can then be detected by down-mixing to the mechanical resonance frequency with an additional AC drive along the z-axis.

6.2.2 Nanofabrication

We present data from two devices, fabricated simultaneously on the same 500 μm thick SOI chip, with different permalloy disk diameters. Nanofabrication is performed using two e-beam lithography steps. The first defines the optical disks and mechanical resonators, followed by reactive ion etching to transfer this pattern to the single crystal silicon. After etching, the resist is removed and a second e-beam lithography step is used to define a disk on the "landing pad" of the torsional resonator. Up to this point fabrication is similar our previous torsional devices (see Sec. 5.2.2.1), but in this work we slowly deposit 50 nm of

permalloy ($Ni_{80}Fe_{20}$) in ultra-high vacuum to produce low-defect density nanomagnetic disks [47; 117]. After permalloy deposition and lift-off procedure, we release the silicon torsional resonator from the underlying sacrificial layer using VHF. A completed device is shown in Fig. 6.1a.

6.2.3 Experimental apparatus

The chip of nanomagnetic optomechanical resonators is aligned on top of a printed circuit board patterned with drive coils [2; 120] inside of a custom measurement vacuum chamber. The drive coils allow AC excitation in both the x and z-axes, Fig. 6.1c, for the purpose of resonant drive for measurement of magnetization (using the z-axis coil) and down-mixing of high frequency spin modes (using both the x and z-axis coils). Optomechanical measurement is performed using dimpled tapered fiber coupling [153; 89] to the WGM optical resonator. Thermomechanical calibration [86] reveals a torque sensitivity of 0.5 zNm/$\sqrt{\text{Hz}}$ sensitivity for both devices presented here, approximately four orders of magnitude better than devices used in previous TMRS measurements [2], This level of torque sensitivity enables us to drive the AC excitation coils without the need for high-power amplifiers that in past measurements have limited the drive frequency [2], extending our measurement bandwidth above 1 GHz. Finally, external magnetic fields are applied using a permanent magnet affixed to a long-range-travel positioning stage (see Fig. 6.1d), and measured with a three axis Hall probe (SENIS F3A-03A02F-A02T2K5M). TMRS data is acquired by simultaneously sweeping the frequencies of UHF signals applied to x and z-axis coils, keeping their frequency difference locked to that of the torsional resonance. The two signal generators are synced to an external rubidium frequency standard. The optomechanically-detected, down-mixed signal is recorded using a 50 MHz digital lock-in.

§ 6.3 Results and discussion

6.3.1 Torque-mixing spectrum

TMRS data is acquired by simultaneously sweeping the frequencies of UHF signals applied to the x and z-axis coils, keeping their frequency difference locked to that of the torsional resonance. The torque applied by a magnetic field, $\boldsymbol{H}$, applied to a magnetic moment, $\boldsymbol{m}$, on a torsional resonator is given by

$$\boldsymbol{\tau} = \boldsymbol{m} \times \mu_0 \boldsymbol{H}. \tag{6.1}$$

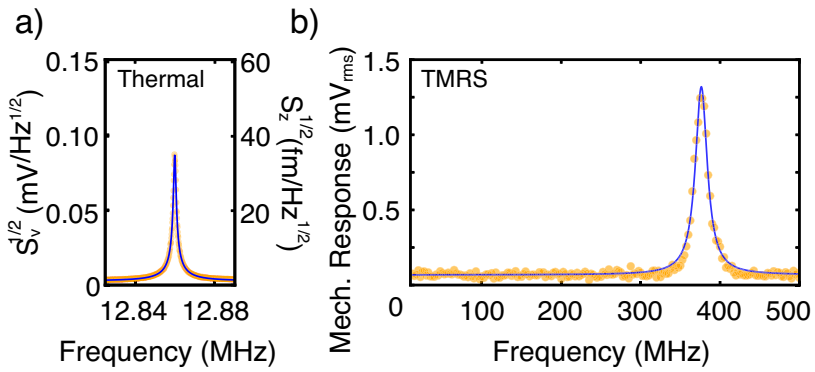

Figure 6.3: **TMRS data** (a) An example of a typical optomechancial response with thermal motion at room temperature. (b) The mechanical response as a function of the swept drive frequency (H_x^{AC}) are shown, where the gyrotropic mode is transduced as an amplification at the torsional frequency. Using this technique, any high frequency spin modes can be mapped to the torsional frequency.

Considering the fixed orientations in our experiment, this can be rewritten as

$$\tau_y = V\chi_m H_x(f_x) \times \mu_0 H_z(f_z), \tag{6.2}$$

where $f_x - f_z$ is fixed at the torsional resonance frequency. Here χ_m is the magnetic susceptibility of the permalloy disk (along the x axis) and V is the disk volume. Sweeping $f_x - f_z$ then measures the frequency dependence of the spin modes via the frequency dependence of χ_m, and allows observation of spin resonances.

In Fig. 6.4, we show a sample of such a down-mixed spin resonance for a 0.85 μm diameter permalloy disk, with a thickness to radius ratio of 0.12. In the absence of pinning, the in-plane gyration of the vortex, called the gyrotropic mode, is expected to be at 480 MHz [145], in good agreement with the average value in the current experiment. Yet there is significant variation of the gyrotropic mode frequency with the applied in-plane magnetic field. A variety of features can be seen, such as a range of applied fields from 160 to 180 Oe where the resonance changes slowly and smoothly, and regions – near 200 Oe (16 kA/m) for example – where the resonance frequency varies more significantly and with abrupt changes. This can be understood as the vortex core, which is roughly 10 nm in diameter [152], moving through defect-free regions where the resonance remains constant or regions where the vortex interacts with defects [144; 154]. Interaction with a defect, such as a variation in the film thickness [155], is known to confine and pin vortices [149; 156]. The gyrotropic spin mode can be thought of as a harmonic oscillation of the vortex in a potential well defined by the stiffness of the in-plane magnetization [157]. When the vortex interacts with a defect it

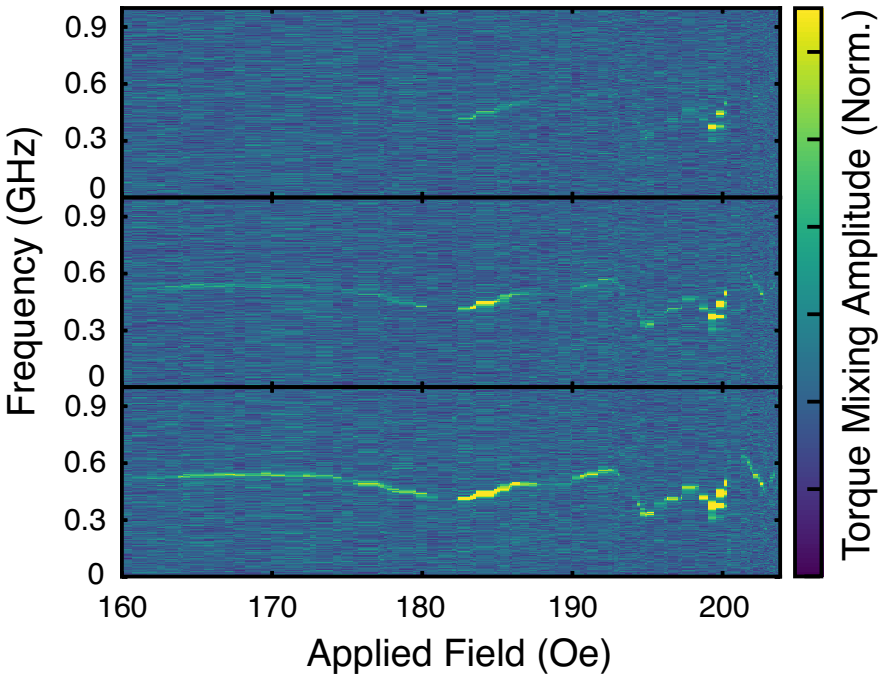

Figure 6.4: **Spin resonances** The spectrum of the spin-modes, corresponding to the gyrotropic motion of a single magnetic vortex in a 0.85 μm diameter permalloy disk, is shown at three diffrent UHF drive powers, 3, 5, and 7 dBm from top to bottom. The same power was applied in both the x and z axes. At these levels, the UHF drive fields do not alter the gyrotropic mode frequencies, revealing the unadulterated behavior. High powers cause drifts in the optomechanical read-out scheme by thermally shifting the optical resonance.

becomes more tightly localized and the stiffness increases, increasing the frequency of the gyrotropic spin mode [156; 158].

The UHF magnetic field applied along the x-axis serves to drive the vortex gyrotropic processions and, in principle, could alter the potential landscape seen by the vortex [159] and hence the gyrotropic mode frequencies. To test whether or not our drive fields affect the spin resonance frequencies we scanned the identical vortex pathway through the permalloy disk at multiple UHF drive powers. Fig. 6.4 demonstrates that we are indeed in the regime where one can safely ignore the influence of the drive amplitude (we show three drive powers that range from a barely visible signal to the verge of heating the optomechanical chip). Residing in this regime allows us the opportunity to observe the effects of pinning, whereas at higher gyration amplitudes the vortex effectively sees a pristine landscape [145; 156].

Future experiments mitigating sample heating effect could test magnetically assisted vortex de-pinning and its effect on the gyrotropic mode frequencies [156; 159].

6.3.2 Vortex pinning

We now turn our attention to a second device, fabricated to house a 1.1 μm diameter permalloy disk. As seen in Fig. 6.5 the average gyrotropic mode frequency in this disk is somewhat lower, ∼400 MHz, consistent with expectations from geometric scaling arguments. A larger disk has lower magnetic stiffness since the vacuum boundaries are further away and hence lower gyrotropic mode frequency, predicted to be ∼385 MHz for a thickness to radius ratio of 0.09 [145]. Here we additionally perform measurements of the total magnetization of the nanomagnetic disk by directly driving the torsional mode on resonance with an AC magnetic field along the z-axis and measuring the direct torque, Fig. 6.5 [29; 47]. Furthermore, with a small component of the AC magnetic field applied along the x-axis, the vortex is dithered in-plane and the direct torque also encodes the in-plane magnetic susceptibility, $\partial m/\partial H$, as recently discovered in Ref. [22]. The result is a peak in the direct torque whenever there is a change in the susceptibility, as can be seen in Fig. 6.5a. These susceptibility peaks can be compared with the behaviour of the gyrotropic mode frequencies. Specifically, one can see that at the applied DC magnetic fields where there is an increased susceptibility the gyrotropic mode frequency dips. This is consistent with the picture of the vortex oscillating in a potential defined by the magnetic stiffness, as quantified by the susceptibility. When the susceptibility increases it is easier to alter the magnetization, hence the potential well is shallower and the mode frequency lower.

In light of this, one realizes that the magnetic fields in which the gyrotropic mode frequency increases correspond to the tightest confinement of the vortex, and likely correspond to defects in the permalloy disk. In order to identify a possible source of these defects we compare with micromagnetic simulations (performed using mumax) [160]. Fig. 6.5b shows simulations of the gyrotropic mode spectrum including a polycrystalline grain size of 20 nm with variations in the saturation magnetization of ±10% (around $M_s = 800$ kA m^{-1}) [161]. Good qualitative agreement is seen between the simulation and measurement, with large variations in the spin mode frequencies as the vortex moves through the pinning associated with the simulated grains. Therefore, the pinning defects observed in the measurements could originate from polycrystallinity. We also note that these simulations suggest that the vortex annihilation should occur at an applied field just above which we used in these experiments. Comparing with the radius of the disk, one can roughly calibrate the applied magnetic field in terms of vortex displacement. One can then read off of Fig. 6.5a that a defect occurs roughly every 50 Oe, suggesting that our permalloy film contains polycrystalline

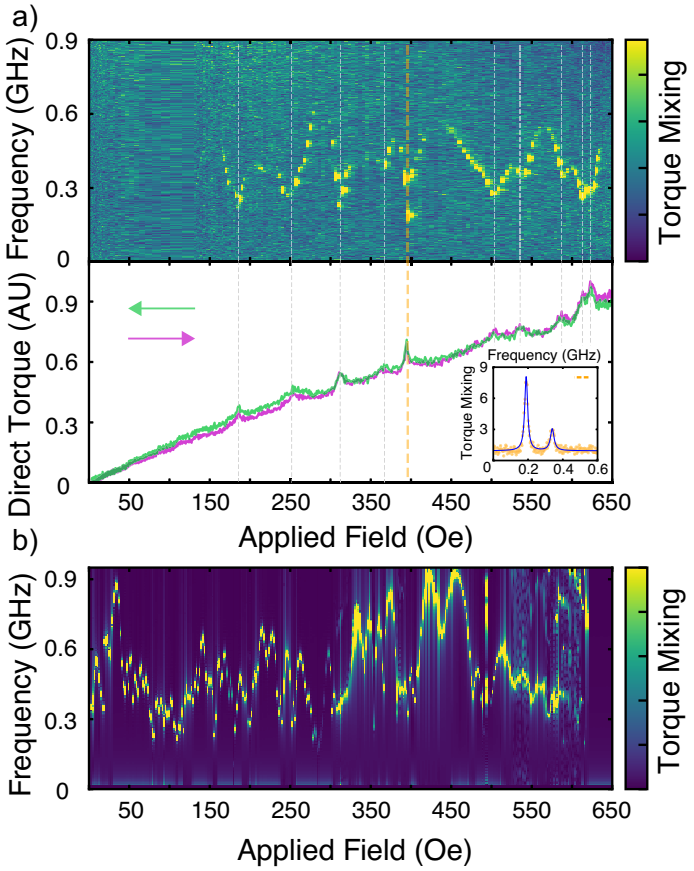

Figure 6.5: **Vortex pinning** (a) Gyrotropic resonance (taken while sweeping from low to high in-plane field) and direct torque measurements of the in-plane magnetization and susceptibility of a 1.1 μm diameter permalloy disk. The peaks in the direct torque correspond to increases in the susceptibility, $\partial m/\partial H$. Indicated by the dashed lines, these points of softer magnetization also correspond to dips in the gyrotropic mode frequency, indicating that the vortex experiences a lower restoring force to in-plane motion. Inset shows that at certain applied fields, particularly apparent when the vortex experiences a lower restoring force and gyrates at larger amplitude, multiple resonances can be observed. Since the vortex motion is being driven by the UHF fields, these resonances can be independently accessed as the drive frequencies are swept, and correspond to the weak interaction of the vortex with multiple defects. (b) Micromagnetic simulation showing qualitatively similar behavior of the gyrotropic resonance by including 40 nm polycrystalline grains with $\pm$10% variation in the saturation magnetization.

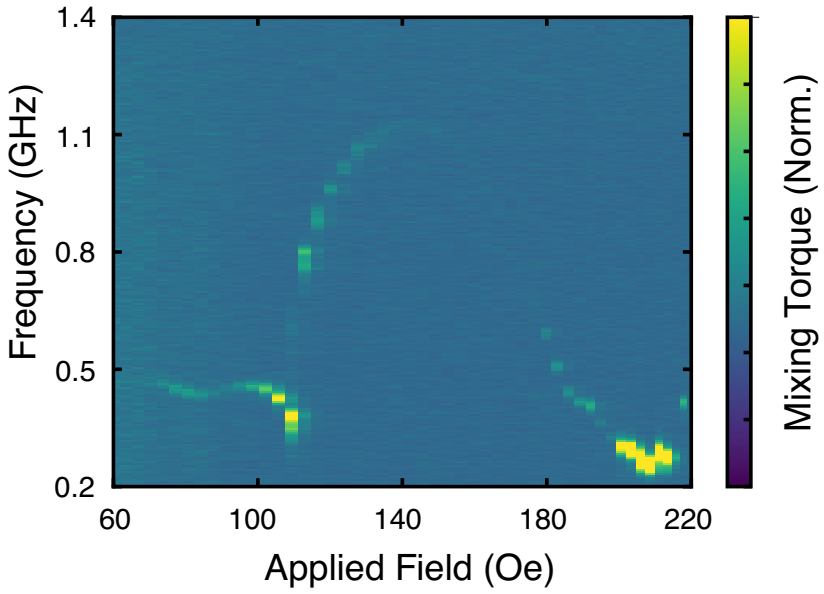

Figure 6.6: **High frequency vortex pinning** As a vortex traverses the permalloy disk it encounter defects that act as pinning sites for the vortex. Here we show a pinning site that drives the gyrotropic mode frequency above 1.1 GHz. Pinning lasts over applied fields of 7 mT, demonstrating that such high-frequency spin modes can be field-stable for other applications.

grains of ∼40 nm.

Finally, we report on the observation of a rare event observed in the 1.1 μm diameter permalloy disk device. At one particular orientation of DC magnetic field in the plane of the disk, we observed a strong pinning of the vortex that drove the gyrotropic mode up to ∼1.1 GHz. This event, shown in Fig. 6.6, pinned the vortex over a field range of approximately 70 Oe (5.6 kA/m), demonstrating the stability of such a pinned state to perturbations in the applied field. Together these observations lead us to speculate that by engineering defects, as has been done with localized focused-ion-beam milling [47], one could control the spin mode resonance frequencies for potential applications. Such as discussed above, the conversion of GHz signals to telecom wavelengths [128; 150]. Additionally, the ability to simultaneously study magnetization, susceptibility, and spin resonances together are of great utility in a lab-on-a-chip approach to nanomagnetism.

§ 6.4 Conclusion and outlook

In conclusion, by taking advantage of the sensitivity and bandwidth of cavity optomechanical detection, we are able to observe ultra-high frequency spin modes in permalloy disks through the technique of torque mixing resonance spectroscopy. Combined with direct torque measurements of the in-plane susceptibility and micromagnetic simulations, we are able to show how the gyrotropic mode of individual magnetic vortices interacts with localized defects in the permalloy. When a vortex is pinned by such defects the spin mode frequencies can jump to as high as 1.1 GHz, a phenomenon that has previously only been observed in time-resolved Kerr microscopy [155; 162; 163]. Opportunities exist for novel applications in control of these spin mode frequencies through the engineering of defects. Furthermore with the TMRS sensitivity and bandwidth presented here, it may be possible to observe non-thermal, quantum effects of vortex dynamics at low temperatures [164].

- Chapter 7 -

CONCLUSION

Somewhere, something incredible is waiting to be known.

- Carl Sagan

§ 7.1 Summary

Precision measurements are essential to our understanding of the fundamental laws and nature. In recent years, with the advancement of nanofabrication, the size of nanomechanical devices have reduced significantly in to on-chip level. Following this miniturization, came a new challenge of measuring them, where a paradigm shift of using resonant light to sensitively measure on-chip devices soon followed. Cavity optomechanics has attracted substantial attention due to its remarkable sensitivities in strains, displacements, and forces while still minaturized. In this work, I have demonstrated an exquisite torque sensitivity near the standard quantum limit by passive-cooling the mechanics in a dilution refrigerator. The experimental framework followed my Master's project, but equipped with advanced fabrication methods and optomechanically compatible dilution refrigerator. Persevering through these challenges, I have achieved a record of torque sensitivity reaching 2.9 yNm/$\sqrt{\text{Hz}}$ thermalized at 25 mK.

Novel experiments of hybrid systems followed: first, the use magnetic forces to amplify and dampen the torsional mode via a feedback-loop, and second, implementing TMRS technique to extract magnetic properties of a soft magnet. These experiments were successful due to an increased fabrication yield based on a VHF method to protect the magnetic film layer during the release step. For the permanently magnetized iron-needle project, controlling

the amplitude of the torsional motion via an external out-of-plane field made it possible to actively cool the torsional mode down to 11.6 K. We confirmed experimentally that feedback mechanism does not contribute to the torque sensitivity because the dissipation compensates the mode temperature. For the next study of permalloy-disks, a down-mixing strategy of a spin-mode allows us to track the spin resonance at high frequencies. In a special case, we observed pinning of a vortex, where the spin-mode increased to above 1.1 GHz. If vortex-pinning can be controlled by fabrication and characterization, a wavelength conversion of microwaves (GHz) to optics (THz) may be possible for quantum-information applications.

Thus far, I have demonstrated three experiments: a near-SQL torque sensitivity and hybrid systems of magnetism and torsional optomechanics. The next step would be to combine hybrid systems in a dilution refrigerator, to study vortex dynamics in a mesoscopic superconductor. A prototype has already been made with an aluminium film, a superconducting disk, deposited on a torsional resonator, and there are plans to incorporate magnetic fields in a dilution refrigerator. Optomechanical torque sensor is a *sine qua non* for nanomagnetism studies. Equipped with near-quantum-limited precision on torque, the doors are opened for other scientific advancements and applications.

§ 7.2 Outlook

Modelled after the paramagnetic Meissner effect studies on type-I superconductors, where vortices are formed due to mesoscopic confinements [27; 65], I hope to extend this experiment. With a sensitive platform of optomechanical torque magnetometry, equipped with DC bias and RF fields, I wish to see the dynamics of these vortices detected by TMRS technique. As an intermediate step, we can look into other materials, such as Nb (higher transition temperature of ~ 9.3 K), to circumvent the issues with low-duty cycle measurements and optical heating. Progress has been made for the apparatus to include bias and superconducting transmission lines to generate in-plane and out-of-plane magnetic fields to prepare for TMRS measurements. Additional information on a demagnetization stage is also included in the appendix to access $\sim \mu$K temperatures.

For room temperature experiments, other magnetic materials may be implemented: Yttrium iron garnet (YIG) has a small linewidth in electron spin resonance, better suited for microwave-to-telecom wavelength conversion; Terfenol-D has a high magneto-striction, which can be used for a sensitive field sensor; and stacks of ferro- and ferri magnets may be used for storage applications. With each application, comes with its own difficulty in deposition and fabrication, however an optomechanical technique will be able to characterize

the film qualitatively and quantitatively as long as magnetic properties, with external field, can be translated to torque. I hope my optomechanical torque magnetometer will serve as a platform for various studies in quantum information, spin-dynamics, and material science.

BIBLIOGRAPHY

[1] L. He, H. Li, and M. Li. Optomechanical measurement of photon spin angular momentum and optical torque in integrated photonic devices. *Science Advances*, 2(9):e1600485, 2016.

[2] J. E. Losby, F. Fani Sani, D. T. Grandmont, Z. Diao, M. Belov, J. A. J. Burgess, S. R. Compton, W. K. Hiebert, D. Vick, K. Mohammad, E. Salimi, G. E. Bridges, D. J. Thomson, and M. R. Freeman. Torque-mixing magnetic resonance spectroscopy. *Science*, 350(6262):798–801, 2015.

[3] A. Eyal, X. Mi, A. V. Talanov, and J. D. Reppy. Search for supersolidity in solid ^{4}He using multiple-mode torsional oscillators. *Proceedings of the National Academy of Sciences*, 113(23):E3203–E3212, 2016.

[4] G. Binnig, C. F. Quate, and Ch. Gerber. Atomic force microscope. *Physical Review Letters*, 56(9):930–933, 1986.

[5] J. Condon and J. Marcus. Fermi surface of calcium by the de Haas-van Alphen effect. *Physical Review*, 134(2A):A446–A452, 1964.

[6] C. Liu, E. Kim, B. Demple, and N. C. Seeman. A DNA-based nanomechanical device used to characterize the distortion of DNA by apo-SoxR protein. *Biochemistry*, 51(5):937–943, 2012.

[7] X. C. Zhang, E. B. Myers, J. E. Sader, and M. L. Roukes. Nanomechanical torsional resonators for frequency-shift infrared thermal sensing. *Nano Letters*, 13(4):1528–1534, 2013.

[8] A. D. O'Connell, M. Hofheinz, M. Ansmann, R. C. Bialczak, M. Lenander, E. Lucero, M. Neeley, D. Sank, H. Wang, M. Weides, J. Wenner, J. M. Martinis, and A. N. Cleland. Quantum ground state and single-phonon control of a mechanical resonator. *Nature*, 464(7289):697–703, 2010.

[9] A. N. Cleland and M. L. Roukes. Fabrication of high frequency nanometer scale mechanical resonators from bulk Si crystals. *Applied Physics Letters*, 69(18):2653–2655, 1996.

[10] Y. A. Pashkin, Y. Nakamura, and J. S. Tsai. Room-temperature Al single-electron transistor made by electron-beam lithography. *Applied Physics Letters*, 76(16):2256–2258, 2000.

[11] D. Rugar, R. Budakian, H. J. Mamin, and B. W. Chui. Single spin detection by magnetic resonance force microscopy. *Nature*, 430(6997):329–332, 2004.

[12] R. G. Knobel and A. N. Cleland. Nanometre-scale displacement sensing using a single electron transistor. *Nature*, 424(6946):291–293, 2003.

[13] A. Suhel, B. D. Hauer, T. S. Biswas, K. S. D. Beach, and J. P. Davis. Dissipation mechanisms in thermomechanically driven silicon nitride nanostrings. *Applied Physics Letters*, 100(17):173111, 2012.

[14] B. P. Abbott et al. LIGO: the laser interferometer gravitational-wave observatory. *Reports on Progress in Physics*, 72(7):076901, 2009.

[15] B. P. Abbott et al. Observation of gravitational waves from a binary black hole merger. *Physical Review Letters*, 116(6):061102, 2016.

[16] M. Borselli, T. J. Johnson, and O. Painter. Beyond the Rayleigh scattering limit in high-Q silicon microdisks: theory and experiment. *Optics Express*, 13(5):1515, 2005.

[17] M. Eichenfield, R. Camacho, J. Chan, K. J. Vahala, and O. Painter. A picogram- and nanometre-scale photonic-crystal optomechanical cavity. *Nature*, 459(7246):550–555, 2009.

[18] D. Kleckner, W. Marshall, M. J. A. de Dood, K. Nima Dinyari, B. Pors, W. T. M. Irvine, and D. Bouwmeester. High finesse opto-mechanical cavity with a movable thirty-micron-size mirror. *Physical Review Letters*, 96(17):173901, 2006.

[19] K. Jensen, K. Kim, and A. Zettl. An atomic-resolution nanomechanical mass sensor. *Nature Nanotechnology*, 3(9):533–537, 2008.

[20] Y. Liu, H. Miao, V. Aksyuk, and K. Srinivasan. Wide cantilever stiffness range cavity optomechanical sensors for atomic force microscopy. *Optics Express*, 20(16):18268, 2012.

[21] P. H. Kim, F. Fani Sani, M. R. Freeman, and J. P. Davis. Broadband optomechanical transduction of nanomagnetic spin modes. *Applied Physics Letters*, 113(8):083104, 2018.

[22] M. Wu, N. L.-Y. Wu, T. Firdous, F. Fani Sani, J. E. Losby, M. R. Freeman, and P. E. Barclay. Nanocavity optomechanical torque magnetometry and radiofrequency susceptometry. *Nature Nanotechnology*, 12(2):127–131, 2016.

[23] J. Ahn, Z. Xu, J. Bang, Y.-H. Deng, T. M. Hoang, Q. Han, R.-M. Ma, and T. Li. Optically levitated nanodumbbell torsion balance and GHz nanomechanical rotor. *Physical Review Letters*, 121(3):033603, 2018.

[24] J. D. Teufel, T. Donner, D. Li, J. W. Harlow, M. S. Allman, K. Cicak, A. J. Sirois, J. D. Whittaker, K. W. Lehnert, and R. W. Simmonds. Sideband cooling of micromechanical motion to the quantum ground state. *Nature*, 475(7356):359–363, 2011.

[25] R. A. Norte, J. P. Moura, and S. Gröblacher. Mechanical resonators for quantum optomechanics experiments at room temperature. *Physical Review Letters*, 116(14):147202, 2016.

[26] K. C. Neuman and A. Nagy. Single-molecule force spectroscopy: optical tweezers, magnetic tweezers and atomic force microscopy. *Nature Methods*, 5(6):491–505, 2008.

[27] A. K. Geim, S. V. Dubonos, J. G. S. Lok, M. Henini, and J. C. Maan. Paramagnetic meissner effect in small superconductors. *Nature*, 396(6707):144–146, 1998.

[28] A. C. Bleszynski-Jayich, W. E. Shanks, B. R. Ilic, and J. G. E. Harris. High sensitivity cantilevers for measuring persistent currents in normal metal rings. *Journal of Vacuum Science & Technology B: Microelectronics and Nanometer Structures*, 26(4):1412, 2008.

[29] J. P. Davis, D. Vick, D. C. Fortin, J. A. J. Burgess, W. K. Hiebert, and M. R. Freeman. Nanotorsional resonator torque magnetometry. *Applied Physics Letters*, 96(7):072513, 2010.

[30] H. Shokrollahi. A review of the magnetic properties, synthesis methods and applications of maghemite. *Journal of Magnetism and Magnetic Materials*, 426:74–81, 2017.

[31] J. M. D. Coey. *Magnetism and magnetic materials*. Cambridge University Press, 2010.

[32] C.-G. Stefanita. *From bulk to nano, the many sides of magnetism*. Springer Berlin Heidelberg, 2008.

[33] C.-G. Stefanita. *Magnetism*. Springer Berlin Heidelberg, 2012.

[34] E. Danieli, J. Mauler, J. Perlo, B. Blmich, and F. Casanova. Mobile sensor for high resolution NMR spectroscopy and imaging. *Journal of Magnetic Resonance*, 198(1):80–87, 2009.

[35] D. C. Jiles. Recent advances and future directions in magnetic materials. *Acta Materialia*, 51(19):5907–5939, 2003.

[36] N. Takahashi, Y. Ushigami, M. Yabumoto, Y. Suga, H. Kobayashi, T. Nakayama, and T. Nozawa. Production of very low core loss grain-oriented silicon steel. *IEEE Transactions on Magnetics*, 22(5):490–495, 1986.

[37] M. Nakano, K. Ishiyama, and K. L. Arai. Production of ultra thin grain oriented silicon steel sheets. *IEEE Transactions on Magnetics*, 31(6):3886–3888, 1995.

[38] C. A. Coulomb. Premier mémoire sure l'électricité et le magnétisme. *Histoire de l'Académie Royale des Sciences*, 88:569–577, 1785.

[39] H. Cavendish. Experiments to determine the density of the earth. *Philosophical Transactions of the Royal Society of London*, 88:469–526, 1798.

[40] S. J. Barnett. Magnetization by rotation. *Physical Review*, 6(4):239–270, 1915.

[41] A. Einstein and W. J. de Haas. Experimental proof of the existence of Ampère's molecular currents. *Royal Neth. Acad. Arts Sciences*, 18:696–711, 1915.

[42] M. N. Baibich, J. M. Broto, A. Fert, F. Nguyen Van Dau, F. Petroff, P. Etienne, G. Creuzet, A. Friederich, and J. Chazelas. Giant magnetoresistance of (001)Fe/(001)Cr magnetic superlattices. *Physical Review Letters*, 61(21):2472–2475, 1988.

[43] G. Binasch, P. Grnberg, F. Saurenbach, and W. Zinn. Enhanced magnetoresistance in layered magnetic structures with antiferromagnetic interlayer exchange. *Physical Review B*, 39(7):4828–4830, 1989.

[44] J. E. Losby and M. R. Freeman. Spin mechanics. *Physics in Canada*, 72(2):71–75, 2016.

[45] M. L. Roukes and A. N. Cleland. A nanometre-scale mechanical electrometer. *Nature*, 392(6672), 1998.

[46] J. E. Losby, Z. Diao, F. Fani Sani, D. T. Grandmont, M. Belov, J. A. J. Burgess, W. K. Hiebert, and M. R. Freeman. Nanomechanical AC susceptometry of an individual mesoscopic ferrimagnet. *Solid State Communications*, 198:3–6, 2014.

[47] J. A. J. Burgess, A. E. Fraser, F. F. Sani, D. Vick, B. D. Hauer, J. P. Davis, and M. R. Freeman. Quantitative magneto-mechanical detection and control of the Barkhausen effect. *Science*, 339(6123):1051–1054, 2013.

[48] P. H. Kim, C. Doolin, B. D. Hauer, A. J. R. MacDonald, M. R. Freeman, P. E. Barclay, and J. P. Davis. Nanoscale torsional optomechanics. *Applied Physics Letters*, 102(5):053102, 2013.

[49] S. Forstner, S. Prams, J. Knittel, E. D. van Ooijen, J. D. Swaim, G. I. Harris, A. Szorkovszky, W. P. Bowen, and H. Rubinsztein-Dunlop. Cavity optomechanical magnetometer. *Physical Review Letters*, 108(12):120801, 2012.

[50] M. Bao. *Analysis and design principles of MEMS devices*. Elsevier Science, 2005.

[51] J. J. Wortman and R. A. Evans. Young's modulus, shear modulus, and poisson's ratio in silicon and germanium. *Journal of Applied Physics*, 36(1):153, 1965.

[52] U. Marconi, A. Puglisi, L. Rondoni, and A. Vulpiani. Fluctuation-dissipation: response theory in statistical physics. *Physics Reports*, 461(4-6):111–195, 2008.

[53] A. Einstein. Über die von der molekularkinetischen theorie der wärme geforderte bewegung von in ruhenden flüssigkeiten suspendierten teilchen (english: On the movement of small particles suspended in a stationary liquid demanded by the molecular-kinetic theory of heat). *Annalen der Physik*, 322(8):549–560, 1905.

[54] J. D. Teufel, T. Donner, M. A. Castellanos-Beltran, J. W. Harlow, and K. W. Lehnert. Nanomechanical motion measured with an imprecision below that at the standard quantum limit. *Nature Nanotechnology*, 4(12):820–823, nov 2009.

[55] A. A. Clerk. Quantum-limited position detection and amplification: A linear response perspective. *Physical Review B*, 70(24):245306, 2004.

[56] J. D. Teufel, F. Lecocq, and R. W. Simmonds. Overwhelming thermomechanical motion with microwave radiation pressure shot noise. *Physical Review Letters*, 116(1):013602, 2016.

[57] M. Aspelmeyer, T. J. Kippenberg, and F. Marquardt. Cavity optomechanics. *Reviews of Modern Physics*, 86(4):1391–1452, 2014.

[58] J. Chan, T. P. M. Algere, A. H. Safavi-Naeini, J. T. Hill, A. Krause, S. Gröblacher, M. Aspelmeyer, and O. Painter. Laser cooling of a nanomechanical oscillator into its quantum ground state. *Nature*, 478(7367):89–92, 2011.

[59] R. Rivière, S. Deléglise, S. Weis, E. Gavartin, O. Arcizet, A. Schliesser, and T. J. Kippenberg. Optomechanical sideband cooling of a micromechanical oscillator close to the quantum ground state. *Physical Review A*, 83(6):063835, 2011.

[60] D. Rugar and P. Grütter. Mechanical parametric amplification and thermomechanical noise squeezing. *Physical Review Letters*, 67(6):699–702, 1991.

[61] D. W. Carr, S. Evoy, L. Sekaric, H. G. Craighead, and J. M. Parpia. Parametric amplification in a torsional microresonator. *Applied Physics Letters*, 77(10):1545–1547, 2000.

[62] W. C. Tang, M. G. Lim, and R. T. Howe. Electrostatic comb drive levitation and control method. *Journal of Microelectromechanical Systems*, 1(4):170–178, 1992.

[63] I. Žutić, J. Fabian, and S. D. Sarma. Spintronics: Fundamentals and applications. *Reviews of Modern Physics*, 76(2):323–410, 2004.

[64] V. A. Schweigert and F. M. Peeters. Phase transitions in thin mesoscopic superconducting disks. *Physical Review B*, 57(21):13817–13832, 1998.

[65] A. K. Geim, I. V. Grigorieva, S. V. Dubonos, J. G. S. Lok, J. C. Maan, A. E. Filippov, F. M. Peeters, and P. S. Deo. Mesoscopic superconductors as 'artificial atoms' made from cooper pairs. *Physica B: Condensed Matter*, 249-251:445–452, 1998.

[66] G. Alzetta, E. Arimondo, C. Ascoli, and A. Gozzini. Paramagnetic resonance experiments at low fields with angular-momentum detection. *Il Nuovo Cimento B Series 10*, 52(2):392–402, 1967.

[67] R. W. Andrews, R. W. Peterson, T. P. Purdy, K. Cicak, R. W. Simmonds, C. A. Regal, and K. W. Lehnert. Bidirectional and efficient conversion between microwave and optical light. *Nature Physics*, 10(4):321–326, 2014.

[68] P. H. Kim, B. D. Hauer, C. Doolin, F. Souris, and J. P. Davis. Approaching the standard quantum limit of mechanical torque sensing. *Nature Communications*, 7:13165, 2016.

[69] C. Doolin, B. D. Hauer, P. H. Kim, A. J. R. MacDonald, H. Ramp, and J. P. Davis. Nonlinear optomechanics in the stationary regime. *Physical Review A*, 89(5):053838, 2014.

[70] M. Wu, A. C. Hryciw, C. Healey, D. P. Lake, H. Jayakumar, M. R. Freeman, J. P. Davis, and P. E. Barclay. Dissipative and dispersive optomechanics in a nanocavity torque sensor. *Physical Review X*, 4(2):021052, 2014.

[71] K. L. Ekinci and M. L. Roukes. Nanoelectromechanical systems. *Review of Scientific Instruments*, 76(6):061101, 2005.

[72] T. J. Kippenberg, S. M. Spillane, and K. J. Vahala. Kerr-nonlinearity optical parametric oscillation in an ultrahigh-Q toroid microcavity. *Physical Review Letters*, 93(8):083904, 2004.

[73] A. H. Safavi-Naeini, J. T. Hill, S. Meenehan, J. Chan, S. Gröblacher, and O. Painter. Two-dimensional phononic-photonic band gap optomechanical crystal cavity. *Physical Review Letters*, 112(15):153603, 2014.

[74] C. Doolin, P. H. Kim, B. D. Hauer, A. J. R. MacDonald, and J. P. Davis. Multidimensional optomechanical cantilevers for high-frequency force sensing. *New Journal of Physics*, 16(3):035001, 2014.

[75] S. Forstner, E. Sheridan, J. Knittel, C. L. Humphreys, G. A. Brawley, H. Rubinsztein-Dunlop, and W. P. Bowen. Ultrasensitive optomechanical magnetometry. *Advanced Materials*, 26(36):6348–6353, 2014.

[76] R. Beth. Mechanical detection and measurement of the angular momentum of light. *Physical Review*, 50(2):115–125, 1936.

[77] K. E. Petersen. Silicon as a mechanical material. *Proceedings of the IEEE*, 70(5):420–457, 1982.

[78] M. A. Green and M. J. Keevers. Optical properties of intrinsic silicon at 300 K. *Progress in Photovoltaics: Research and Applications*, 3(3):189–192, 1995.

[79] G. Timp. *Nanotechnology*. Springer New York, 2012.

[80] M. Bruel. Separation of silicon wafers by the smart-cut method. *Materials Research Innovations*, 3(1):9–13, 1999.

[81] Nanofab. Raith_GDSII v.1.2, 2014. [Online; accessed May 2, 2019].

[82] L. Reimer. *Scanning electron microscopy*. Springer-Verlag Berlin Heidelberg, 2013.

[83] M. A. Mohammad, M. Muhammad, S. K. Dew, and M. Stepanova. Fundamentals of electron beam exposure and development. In *Nanofabrication*. Springer Vienna, 2011.

[84] H. Jansen, H. Gardeniers, M. de Boer, M. Elwenspoek, and J. Fluitman. A survey on the reactive ion etching of silicon in microtechnology. *Journal of Micromechanics and Microengineering*, 6(1):14–28, 1996.

[85] Z. Diao, J. E. Losby, J. A. J. Burgess, V. T. K. Sauer, W. K. Hiebert, and M. R. Freeman. Stiction-free fabrication of lithographic nanostructures on resist-supported nanomechanical resonators. *Journal of Vacuum Science and Technology B*, 31(5):051805, 2013.

[86] B. D. Hauer, C. Doolin, K. S. D. Beach, and J. P. Davis. A general procedure for thermomechanical calibration of nano/micro-mechanical resonators. *Annals of Physics*, 339:181–207, 2013.

[87] XChen, Chao Li, and Hon K. Tsang. Device engineering for silicon photonics. *NPG Asia Materials*, 3(1):34–40, 2011.

[88] J. D. Cohen, S. M. Meenehan, and O. Painter. Optical coupling to nanoscale optomechanical cavities for near quantum-limited motion transduction. *Optics Express*, 21(9):11227, 2013.

[89] B. D. Hauer, P. H. Kim, C. Doolin, A. J. R. MacDonald, H. Ramp, and J. P. Davis. On-chip cavity optomechanical coupling. *EPJ Techniques and Instrumentation*, 1(1):4, 2014.

[90] A. J. R. MacDonald, G. G. Popowich, B. D. Hauer, P. H. Kim, A. Fredrick, X. Rojas, P. Doolin, and J. P. Davis. Optical microscope and tapered fiber coupling apparatus for a dilution refrigerator. *Review of Scientific Instruments*, 86(1):013107, 2015.

[91] A. J. R. MacDonald, B. D. Hauer, X. Rojas, P. H. Kim, G. G. Popowich, and J. P. Davis. Optomechanics and thermometry of cryogenic silica microresonators. *Physical Review A*, 93(1):013836, 2016.

[92] H. K. Onnes. The liquefacation of helium. *Communications from the Laboratory of Physics at the University of Leiden*, 108, 1908.

[93] H. K. Onnes. The resistance of pure mercury at helium temperatures. *Communications from the Laboratory of Physics at the University of Leiden*, 120b, 1911.

[94] R. A. Fisher, E. W. Hornung, G. E. Brodale, and W. F. Giauque. Magnetothermodynamics of $Ce_2Mg_3(NO_3)_12\cdot 24H_2O$. II. The evaluation of absolute temperature and other thermodynamic properties of CMN to 0.6 m°K. *The Journal of Chemical Physics*, 58(12):5584–5604, 1973.

[95] L. Goldstein. Theory of a magnetic cooling system at very low temperatures. *Journal of Low Temperature Physics*, 17(3-4):385–401, 1974.

[96] K. Gloos, P. Smeibidl, C. Kennedy, A. Singsaas, P. Sekowski, R. M. Mueller, and F. Pobell. The Bayreuth nuclear demagnetization refrigerator. *Journal of Low Temperature Physics*, 73(1-2):101–136, 1988.

[97] F. P. Quacquarelli, J. Puebla, T. Scheler, D. Andres, C. Bödefeld, B. Sipos, C. Dal Savio, A. Bauer, C. Pfleiderer, A. Erb, and K. Karrai. Scanning probe microscopy in an ultra-low vibration closed-cycle cryostat: Skyrmion lattice detection and tuning fork implementation. *Microscopy Today*, 23(06):12–17, 2015.

[98] F. Pobell. *Matter and methods at low temperatures*. Springer Berlin Heidelberg, 2007.

[99] Z. Dokoupil, D. G. Kapadnis, K. Sreeramamurty, and K. W. Taconis. Specific heat of mixtures of 4he and 3he between 1 °k and 4 °k. *Physica*, 25(7-12):1369–1375, 1959.

[100] T. A. Alvesalo, P. M. Berglund, S. T. Islander, G. R. Pickett, and W. Zimmermann. Specific heat of liquid He^3/He^4 mixtures near the junction of the lambda and phase-separation curves. *Physical Review A*, 4(6):2354–2368, 1971.

[101] J. M. Kincaid and E. G. D. Cohen. Phase diagrams of liquid helium mixtures and metamagnets: Experiment and mean field theory. *Physics Reports*, 22(2):57–143, 1975.

[102] P. L. Kapitza. Heat transfer and superfluidity of helium II. *Physical Review*, 60(4):354–355, 1941.

[103] H. Marshak. Nuclear orientation thermometry. *Journal of Research of the National Bureau of Standards*, 88(3):175, 1983.

[104] G. Anetsberger, O. Arcizet, Q. P. Unterreithmeier, R. Rivière, A. Schliesser, E. M. Weig, J. P. Kotthaus, and T. J. Kippenberg. Near-field cavity optomechanics with nanomechanical oscillators. *Nature Physics*, 5(12):909–914, 2009.

[105] S. M. Meenehan, J. D. Cohen, G. S. MacCabe, F. Marsili, M. D. Shaw, and O. Painter. Pulsed excitation dynamics of an optomechanical crystal resonator near its quantum ground state of motion. *Physical Review X*, 5(4):041002, 2015.

[106] R. Riedinger, S. Hong, R. A. Norte, J. A. Slater, J. Shang, A. G. Krause, V. Anant, M. Aspelmeyer, and S. Gröblacher. Non-classical correlations between single photons and phonons from a mechanical oscillator. *Nature*, 530(7590):313–316, 2016.

[107] E. E. Wollman, C. U. Lei, A. J. Weinstein, J. Suh, A. Kronwald, F. Marquardt, A. A. Clerk, and K. C. Schwab. Quantum squeezing of motion in a mechanical resonator. *Science*, 349(6251):952–955, 2015.

[108] V. B. Braginsky, F. Y. Khalili, and K. S. Thorne. *Quantum measurement*. Cambridge University Press, 1995.

[109] A. A. Clerk, M. H. Devoret, S. M. Girvin, Florian Marquardt, and R. J. Schoelkopf. Introduction to quantum noise, measurement, and amplification. *Reviews of Modern Physics*, 82(2):1155–1208, apr 2010.

[110] D. J. Wilson, V. Sudhir, N. Piro, R. Schilling, A. Ghadimi, and T. J. Kippenberg. Measurement-based control of a mechanical oscillator at its thermal decoherence rate. *Nature*, 524(7565):325–329, 2015.

[111] I. Wilson-Rae, N. Nooshi, W. Zwerger, and T. J. Kippenberg. Theory of ground state cooling of a mechanical oscillator using dynamical backaction. *Physical Review Letters*, 99(9):093901, 2007.

[112] F. Marquardt, J. P. Chen, A. A. Clerk, and S. M. Girvin. Quantum theory of cavity-assisted sideband cooling of mechanical motion. *Physical Review Letters*, 99(9):093902, 2007.

[113] B. Zheng, W. Luo, F. Xu, and Y. Lu. Influence of van der Waals forces on the waveguide deformation and power limit of nanoscale waveguide devices. *Physical Review A*, 89(4):043810, 2014.

[114] S. P. Timoshenko, J. N. Goodier, and H. Norman Abramson. Theory of elasticity (3rd ed.). *Journal of Applied Mechanics*, 37(3):888, 1970.

[115] I. S. Sokolnikoff. *Mathematical theory of elasticity*. McGraw-Hill Inc., 1956.

[116] G. I. Harris, D. L. McAuslan, E. Sheridan, Y. Sachkou, C. Baker, and W. P. Bowen. Laser cooling and control of excitations in superfluid helium. *Nature Physics*, 12(8):788–793, 2016.

[117] J. P. Davis, D. Vick, J. A. J. Burgess, D. C. Fortin, P. Li, V. Sauer, W. K. Hiebert, and M. R. Freeman. Observation of magnetic supercooling of the transition to the vortex state. *New Journal of Physics*, 12(9):093033, 2010.

[118] A. K. Geim, S. V. Dubonos, J. G. S. Lok, I. V. Grigorieva, J. C. Maan, L. Theil Hansen, and P. E. Lindelof. Ballistic Hall micromagnetometry. *Applied Physics Letters*, 71(16):2379–2381, 1997.

[119] A. K. Geim, I. V. Grigorieva, and S. V. Dubonos. Collective effects in vortex movements in type-II superconductors observed by a method for the registration of individual vortices. *Physical Review B*, 46(1):324–330, 1992.

[120] P. H. Kim, B. D. Hauer, T. J. Clark, F. Fani Sani, M. R. Freeman, and J. P. Davis. Magnetic actuation and feedback cooling of a cavity optomechanical torque sensor. *Nature Communications*, 8(1):1355, 2017.

[121] G. Kurizki, P. Bertet, Y. Kubo, K. Mølmer, D. Petrosyan, P. Rabl, and J. Schmiedmayer. Quantum technologies with hybrid systems. *Proceedings of the National Academy of Sciences*, 112(13):3866–3873, 2015.

[122] S. Camerer, M. Korppi, A. Jckel, D. Hunger, T. W. Hänsch, and P. Treutlein. Realization of an optomechanical interface between ultracold atoms and a membrane. *Physical Review Letters*, 107(22):223001, 2011.

[123] P. Rath, S. Khasminskaya, C. Nebel, C. Wild, and W. H. P. Pernice. Diamond-integrated optomechanical circuits. *Nature Communications*, 4(1):1690, 2013.

[124] T. M. Hoang, Y. Ma, J. Ahn, J. Bang, F. Robicheaux, Z.-Q. Yin, and T. Li. Torsional optomechanics of a levitated nonspherical nanoparticle. *Physical Review Letters*, 117(12):123604, 2016.

[125] M. Mitchell, B. Khanaliloo, D. P. Lake, T. Masuda, J. P. Hadden, and P. E. Barclay. Single-crystal diamond low-dissipation cavity optomechanics. *Optica*, 3(9):963, 2016.

[126] M. J. Burek, J. D. Cohen, S. M. Meenehan, N. El-Sawah, C. Chia, T. Ruelle, S. Meesala, J. Rochman, H. A. Atikian, M. Markham, D. J. Twitchen, M. D. Lukin, O. Painter, and M. Lončar. Diamond optomechanical crystals. *Optica*, 3(12):1404, nov 2016.

[127] T. Li and Z.-Q. Yin. Quantum superposition, entanglement, and state teleportation of a microorganism on an electromechanical oscillator. *Science Bulletin*, 61(2):163–171, 2016.

[128] J. T. Hill, A. H. Safavi-Naeini, J. Chan, and O. Painter. Coherent optical wavelength conversion via cavity optomechanics. *Nature Communications*, 3(1):1196, 2012.

[129] D. Lachance-Quirion, Y. Tabuchi, S. Ishino, A. Noguchi, T. Ishikawa, R. Yamazaki, and Y. Nakamura. Resolving quanta of collective spin excitations in a millimeter-sized ferromagnet. *Science Advances*, 3(7):e1603150, jul 2017.

[130] B. Ilic, D. Czaplewski, H. G. Craighead, P. Neuzil, C. Campagnolo, and C. Batt. Mechanical resonant immunospecific biological detector. *Applied Physics Letters*, 77(3):450–452, 2000.

[131] N. V. Lavrik, M. J. Sepaniak, and P. G. Datskos. Cantilever transducers as a platform for chemical and biological sensors. *Review of Scientific Instruments*, 75(7):2229–2253, 2004.

[132] P. Mohanty, D. A. Harrington, K. L. Ekinci, Y. T. Yang, M. J. Murphy, and M. L. Roukes. Intrinsic dissipation in high-frequency micromechanical resonators. *Physical Review B*, 66(8):160–162, 2002.

[133] E. P. Wohlfarth. *Ferro-magnetic materials: A handbook on the properties of magnetically ordered substances*. North Holland, 1986.

[134] C. D. Graham. Temperature dependence of anisotropy and saturation magnetization in iron and iron-silicon alloys. *Journal of Applied Physics*, 31(5):S150–S151, 1960.

[135] M. Takahashi. Induced magnetic anisotropy of evaporated films formed in a magnetic field. *Journal of Applied Physics*, 33(3):1101–1106, 1962.

[136] M. Poggio, C. L. Degen, H. J. Mamin, and D. Rugar. Feedback cooling of a cantilever's fundamental mode below 5 mK. *Physical Review Letters*, 99(1):017201, 2007.

[137] A. G. Krause, T. D. Blasius, and O. Painter. Optical read out and feedback cooling of a nanostring optomechanical cavity. *arXiv*, 2015, http://arxiv.org/abs/1506.01249v1.

[138] T. Kippenberg, H. Rokhsari, T. Carmon, A. Scherer, and K. Vahala. Analysis of radiation-pressure induced mechanical oscillation of an optical microcavity. *Physical Review Letters*, 95(3):033901, 2005.

[139] D. A. Garanin and E. M. Chudnovsky. Quantum entanglement of a tunneling spin with mechanical modes of a torsional resonator. *Physical Review X*, 1(1):011005, 2011.

[140] X.-L. Qi, R. Li, J. Zang, and S.-C. Zhang. Inducing a magnetic monopole with topological surface states. *Science*, 323(5918):1184–1187, 2009.

[141] N. Nagaosa and Y. Tokura. Topological properties and dynamics of magnetic skyrmions. *Nature Nanotechnology*, 8(12):899–911, 2013.

[142] J. M. Kosterlitz and D. J. Thouless. Ordering, metastability and phase transitions in two-dimensional systems. *Journal of Physics C: Solid State Physics*, 6(7):1181–1203, 1973.

[143] O. Klein, G. de Loubens, V. V. Naletov, F. Boust, T. Guillet, H. Hurdequint, A. Leksikov, A. N. Slavin, V. S. Tiberkevich, and N. Vukadinovic. Ferromagnetic resonance force spectroscopy of individual submicron-size samples. *Physical Review B*, 78(14):144410, 2008.

[144] J. P. Park, P. Eames, D. M. Engebretson, J. Berezovsky, and P. A. Crowell. Imaging of spin dynamics in closure domain and vortex structures. *Physical Review B*, 67(2):020403(R), 2003.

[145] V. Novosad, F. Y. Fradin, P. E. Roy, K. S. Buchanan, K. Yu. Guslienko, and S. D. Bader. Magnetic vortex resonance in patterned ferromagnetic dots. *Physical Review B*, 72(2):024455, 2005.

[146] K. Perzlmaier, M. Buess, C. H. Back, V. E. Demidov, B. Hillebrands, and S. O. Demokritov. Spin-wave eigenmodes of permalloy squares with a closure domain structure. *Physical Review Letters*, 94(5):057202, feb 2005.

[147] K. Vogt, O. Sukhostavets, H. Schultheiss, B. Obry, P. Pirro, A. A. Serga, T. Sebastian, J. Gonzalez, K. Y. Guslienko, and B. Hillebrands. Optical detection of vortex spin-wave eigenmodes in microstructured ferromagnetic disks. *Physical Review B*, 84(17):174401, 2011.

[148] G. A. Riley, H. J. J. Liu, M. A. Asmat-Uceda, A. Haldar, and K. S. Buchanan. Observation of the dynamic modes of a magnetic antivortex using Brillouin light scattering. *Physical Review B*, 92(6):064423, 2015.

[149] T. Uhlig, M. Rahm, C. Dietrich, R. Höllinger, M. Heumann, D. Weiss, and J. Zweck. Shifting and pinning of a magnetic vortex core in a permalloy dot by a magnetic field. *Physical Review Letters*, 95(23):237205, 2005.

[150] J. Bochmann, A. Vainsencher, D. D. Awschalom, and A. N. Cleland. Nanomechanical coupling between microwave and optical photons. *Nature Physics*, 9(11):712–716, 2013.

[151] R. Hisatomi, A. Osada, Y. Tabuchi, T. Ishikawa, A. Noguchi, R. Yamazaki, K. Usami, and Y. Nakamura. Bidirectional conversion between microwave and light via ferromagnetic magnons. *Physical Review B*, 93(17):174427, 2016.

[152] A. Wachowiak, J. Wiebe, M. Bode, O. Pietzsch, M. Morgenstern, and R. Wiesendanger. Direct observation of internal spin structure of magnetic vortex cores. *Science*, 298(5593):577–580, 2002.

[153] C. P. Michael, M. Borselli, T. J. Johnson, C. Chrystal, and O. Painter. An optical fiber-taper probe for wafer-scale microphotonic device characterization. *Optics Express*, 15(8):4745, 2007.

[154] R. Badea and J. Berezovsky. Mapping the landscape of domain-wall pinning in ferromagnetic films using differential magneto-optical microscopy. *Physical Review Applied*, 5(6):064003, 2016.

[155] T. Y. Chen, M. J. Erickson, P. A. Crowell, and C. Leighton. Surface roughness dominated pinning mechanism of magnetic vortices in soft ferromagnetic films. *Physical Review Letters*, 109(9):097202, 2012.

[156] T. Y. Chen, A. T. Galkiewicz, and P. A. Crowell. Phase diagram of magnetic vortex dynamics. *Physical Review B*, 85(18):180406(R), 2012.

[157] R. Zarzuela, E. M. Chudnovsky, and J. Tejada. Excitation modes of vortices in submicron magnetic disks. *Physical Review B*, 87(1):014413, 2013.

[158] R. L. Compton and P. A. Crowell. Dynamics of a pinned magnetic vortex. *Physical Review Letters*, 97(13):137202, 2006.

[159] R. Badea, J. A. Frey, and J. Berezovsky. Magneto-optical imaging of vortex domain deformation in pinning sites. *Journal of Magnetism and Magnetic Materials*, 381:463–469, 2015.

[160] A. Vansteenkiste, J. Leliaert, M. Dvornik, M. Helsen, F. Garcia-Sanchez, and B. Van Waeyenberge. The design and verification of MuMax3. *AIP Advances*, 4(10):107133, 2014.

[161] B. D. Cullity and C. D. Graham. *Introduction to magnetic materials*. Addison-Wesley Pub. Co., 1972.

[162] R. L. Compton, T. Y. Chen, and P. A. Crowell. Magnetic vortex dynamics in the presence of pinning. *Physical Review B*, 81(14):144412, 2010.

[163] M. J. Rudd, P. H. Kim, C. A. Potts, C. Doolin, H. Ramp, B. D. Hauer, and J. P. Davis. Coherent magneto-optomechanical signal transduction and long-distance phase-shift keying. *arXiv*, 2019, http://arxiv.org/abs/1904.07779v1.

[164] R. Zarzuela, E. M. Chudnovsky, J. M. Hernandez, and J. Tejada. Quantum dynamics of vortices in mesoscopic magnetic disks. *Physical Review B*, 87(14):144420, 2013.

[165] G. R. Pickett. Microkelvin physics. *Reports on Progress in Physics*, 51(10):1295–1340, 1988.

[166] C. Enss and S. Hunklinger. *Low-temperature physics*. Springer-Verlag, 2005.

[167] D. S. Betts. *An introduction to millikelvin technology*. Cambridge University Press, 1989.

[168] S. W. Van Sciver. *Helium cryogenics*. Springer New York, 2012.

[169] T.C.P. Chui. SQUID-based high-resolution thermometer. *Cryogenics*, 41(5-6):407–414, 2001.

[170] T. J. Clark, V. Vadakkumbatt, F. Souris, H. Ramp, and J. P. Davis. Cryogenic microwave filter cavity with a tunability greater than 5 GHz. *Review of Scientific Instruments*, 89(11):114704, 2018.

[171] A. Vainsencher, K. J. Satzinger, G. A. Peairs, and A. N. Cleland. Bi-directional conversion between microwave and optical frequencies in a piezoelectric optomechanical device. *Applied Physics Letters*, 109(3):033107, 2016.

[172] H. Jung and H. X. Tang. Aluminum nitride as nonlinear optical material for on-chip frequency comb generation and frequency conversion. *Nanophotonics*, 5(2):263–271, jan 2016.

[173] C. Xiong, W. H. P. Pernice, X. Sun, C. Schuck, K. Y. Fong, and H. X. Tang. Aluminum nitride as a new material for chip-scale optomechanics and nonlinear optics. *New Journal of Physics*, 14(9):095014, 2012.

[174] X. Rojas and J. P. Davis. Superfluid nanomechanical resonator for quantum nanofluidics. *Physical Review B*, 91(2):024503, 2015.

[175] J. Curie and P. Curie. Phénomènes électriques des cristaux hémièdres à faces inclinées. *Journal de Physique Théorique et Appliquée*, 1(1):245–251, 1882.

[176] R. Ghodssi and P. Lin. *MEMS Materials and Processes Handbook*. Springer, 2011.

[177] S. B. Krupanidhi, N. Maffei, M. Sayer, and K. El-Assal. RF planar magnetron sputtering and characterization of ferroelectric Pb(Zr,Ti)O_3films. *Journal of Applied Physics*, 54(11):6601–6609, 1983.

[178] D. Ambika, V. Kumar, K. Tomioka, and I. Kanno. Deposition of PZT thin films with (001), (110), and (111) crystallographic orientations and their transverse piezoelectric characteristics. *Advanced Materials Letters*, 3(2):102–106, 2012.

[179] J. Lueke, A. Badr, E. Lou, and W. A. Moussa. Microfabrication and integration of a sol-gel PZT folded spring energy harvester. *Sensors*, 15(6):12218–12241, 2015.

[180] X. Rojas, B. D. Hauer, A. J. R. MacDonald, P. Saberi, Y. Yang, and J. P. Davis. Ultrasonic interferometer for first-sound measurements of confined liquid ^{4}He. *Physical Review B*, 89(17):174508, 2014.

[181] K. R. Atkins. Third and fourth sound in liquid helium II. *Physical Review*, 113(4):962–965, 1959.

[182] B. Mednikarov, G. Spasov, and Tz. Babeva. Aluminum nitride layers prepared by DC/RF magnetron sputtering. *Journal of Optoelectronics and Advanced Materials*, 7(3):1421–1427, 2005.

- Appendix A -

ADIABATIC NUCLEAR DEMAGNETIZATION COOLING

In this universe, there's only one absolute... everything freezes!

- Mr. Freeze, DC comics

The technique of adiabatic nuclear demagnetization is well-established, where cold nuclei are able to absorb heat from the surrounding system [165]. Nuclear demagnetization refrigerators are the only method, at present, to cool nanostructured samples beyond the dilution refrigerator stage ($T < 1$ mK). It heavily relies on the initial conditions of temperature and magnetic field, where double-stage demagnetization stage and high magnetic fields (6∼9 T) were engineered previously. Here, I will highlight some progress for our own adaptation of nuclear demagnetization stage and optomechanics.

§ A.1 Cooling Mechanism

Adiabatic demagnetization cooling is based on the magnetic-field dependence of the spin entropy [167]. An example is shown for a paramagnetic salt in Fig. A.1, where the cooling occurs from paths A to C [166]. Initially, the stage is cooled by a dilution refrigerator (point A), where all the spins are oriented randomly. When magnetic field is applied (path B), partial alignment of the spins is achieved depending on the strength of the field. Isolating the temperature via a heat switch, the cooling occurs along path C, as the magnetic field is removed adiabatically. The cycle repeats by altering the heat switch and magnetic fields. Hence, the initial condition of pre-cooling and magnetic field are important to reach sub-mK temperatures. Note that vibration isolation is highly important to avoid any quenching of superconducting magnets. For our system, there are two stages and can be used in series for extended cooling [96] or running two separate experiments depending on the application.

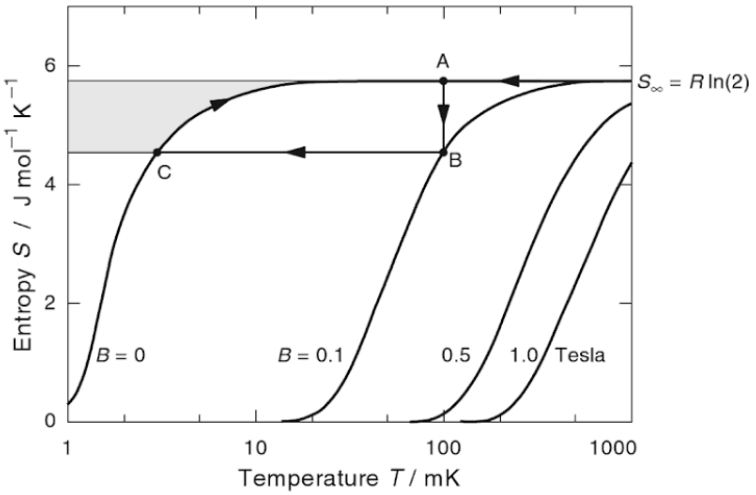

Figure A.1: **Entropy of a salt** Entropy of a paramagnetic salt as a function of temperature for various magnetic fields. The cooling cycle starts in A, a pre-cooled configuration, and a isothermal magnetization occurs in B direction. A heat switch is turned off for thermal isolation and the magnetic field is removed to lower the temperature. This principle applies to nuclear spins as well (Taken from Ref. [166]).

§ A.2 Heat switch

Material	T_c (K)	$\mu_0 H_c$ (mT)	Contact Method
Indium	3.4	27.6	Solder
Lead (Pb)	7.2	80.3	Solder
Cadmium (Cd)	0.52	3.0	Solder
Zinc (Zn)	0.9	5.3	Solder with Cd or In
Aluminum (Al)	1.2	9.9	Clamping or melt

Table A.1: A list of materials for superconducting heat-switches [168]. The base temperature of the dilution refrigerator needs to be well under the transition temperature of these materials, and the superconducting state can be manipulated by quenching through applied magnetic fields ($\mu_0 H_c$ is the critical field). These are all suitable materials, but lead and cadmium may be discouraged due to toxicity and aluminium cannot be soldered.

An important criteria for a successful adiabatic demagnetization stage is the functionality of heat switch to isolate thermal contact. The best strategy is to use superconducting heat switches since a complete thermal isolation can altered by switching between a superconducting state and a normal state. Keeping the base temperature below the superconducting transition temperature, magnetic field is applied to quench or to keep the superconducting

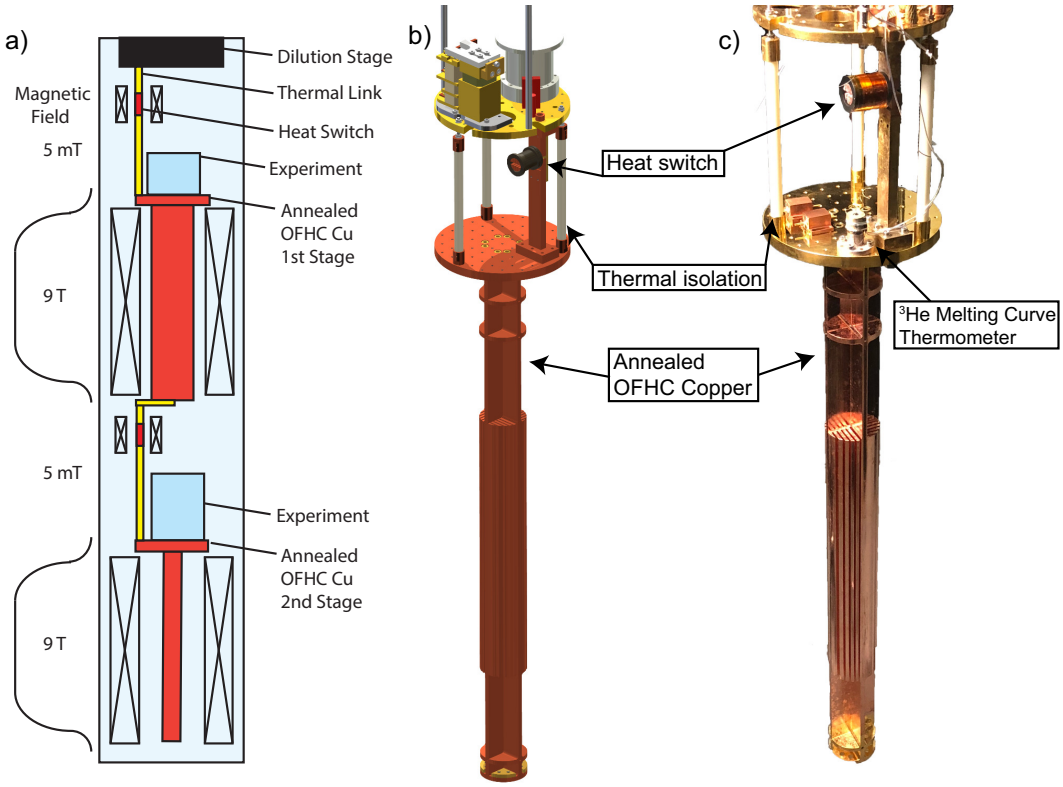

Figure A.2: **Nuclear demagnetization stage** (a) A schematic of the demagnatization stage. Starting from the top, the dilution stage is connected to the oxygen-free high thermal conductivity (OFHC) Cu stage by a superconducting heat switch. The annealed OFHC copper provides the cooling power under a strong magnetic field (9 T magnet). There is a second identical stage isolated by another heat switch for an additional second experiment. (b) A design layout of the demagnetization stage with a photograph of the current progress in (c).

state. Table A.1 shows a list of materials suitable for a heat switch material. Depending on magnetic strength in the heat-switch region, a proper material can be chosen. In our application, we have used soldered indium wires as heat switches. An example of our current progress is shown in Fig. A.2c.

§ A.3 Magnetic field

The high-field magnets are made out of superconducting NbTi coils with $T_c = 9.2$ K. The magnet is immersed in liquid ^{4}He, where the magnetic fields are stable to 9 T. The refrigerator has two sets of high and low field regions (see Fig. A.2a). The low field regions are created by using a equal and opposite Helmholtz coils to cancel the magnetic fields, where the experiments will be placed in the zero field region. Rather than having two independent experiments, the demag stage can run serially so that even lower temperature can be reached by the lower initial condition.

§ A.4 Melting curve thermometer

Recall that at mK temperatures, nuclear orientation thermometer and ruthenium oxide thermometer were used. Finding a thermometer below 1 mK can be quite challenging. Fortunately, there is a primary thermometer that can access temperatures below 1 mK using a melting curve of ^{3}He [166]. There are other device-based candidates: A superconducting quantum interference device (SQUID) that measures sensitive field changes as a function of temperature [169], and an optomechanical cavity that relates the mechanical mode to its environment temperautre [91].

§ A.5 Stage

The quality of the Cu stage is highly important in adiabatic cooling, where annealing is necessary to increase the purity (enlarged grain size). Followed by electroplating gold, to reduce thermal resistance, the experimental stage can be anchored securely to the OFHC stage. Unfortunately, the endoscope will not work in this apparatus, so the sample will have to be coupled prior to the cool down. Rather than the silicon-based telecom wavelength optomechanics, silicon nitride or diamond device may work better to attain less optical heating and more thermal conduction. Alternatively, microwave cavity coupled to torsional resonators seem promising at these temperatures [170].

- Appendix B -

ALUMINIUM NITRIDE

Viva la Vida

- Coldplay

Majority of my work was based on the use of single-crystal silicon. Aluminium nitride (AlN) is another interesting ceramic material that possesses great opto-electro-mechanical properties – utilized for recent frequency conversion applications [171; 172]. As one of my application goal is to convert GHz to THz frequencies using optomechanically detected magnetic spin-modes of Py, an alternative approach of AlN hybrid systems seem interesting to engineer MEMS, hoping to develop better actuators and sensors [173; 150]. AlN has an additional benefit of larger thermal conductivity that is suitable for low temperature experiments where the first breakthrough of quantum mechanics and mechanical oscillator was based on AlN devices [8]. The recipe for AlN deposition comes from the follow-up experiment of Ref. [174] to use piezoelectric transducers as a probe confinement effects of superfluid properties. The same deposition recipe can be used for oxide grown silicon wafers. Since I was heavily involved in the AlN project, a detailed discussion of AlN films will be included along with the recipe for deposition.

§ B.1 Background

Piezein is a Greek word meaning *to press* or *to squeeze*. As the name suggests, piezoelectric materials produce electricity with applied compressive stress - which was first discovered by Jacques and Pierre Curie in 1880s [175]. Recent developments in highly efficient piezoelectric ceramics has attracted a great deal of interest in areas ranging from real-world applications to fundamental tests of quantum phenomena. For instance, a highly sensitive piezoelectric

aluminum nitride (AlN) device coupled to a superconducting qubit in a dilution refrigerator measured superposition states of a mesoscopic mechanical resonator [8].

§ B.2 Principle of piezoelectricity

	AlN	PZT	$LiNO_3$	GaAs
Piezoelectric coefficient, d_{33} (pC/N)	3.4 ∼ 6.5	90 ∼ 150	6 ∼ 30	3.4 ∼ 25
Young's Modulus, E (GPa)	260 ∼ 380	60 ∼ 80	180 ∼ 200	80 ∼ 95
Thermal Conductivity, k (W/m·K)	285	1.8	4	45

Table B.1: Three material properties — piezoelectric coefficient (d_{33}), Young's modulus, and thermal conductivity — of AlN, PZT, $LiNO_3$, and GaAs, extracted from Ref. [176].

Piezoelectric materials typically have a complex non-symmmetrical unit cell, contributing to a net charge when compressed, stretched, or sheared. Due to the asymmetry, a piezoelectric charge constant is a tensor, where we will only consider induced polarization along the applied stress (d_{33}). Table B.1 shows some properties of the popular piezoelectric materials with large piezoelectric coefficients. Although lead zirconate titanate (PZT) seem superior by the piezoelectric coefficient, it is toxic and often difficult to deposit and pattern [177]-[179]. The piezoelectric effect is also reversible: stress is induced by an applied voltage and *vice versa*, where the sensors can also be an actuator at the same time. With this technology, the first sound of superfluid ^{4}He was measured in a microfluidic cavity using PZT [180]. Current progress is made to study fourth sound measurements [181] using smaller cavities. An AlN film is, by-far, forgiving in lithography techniques and etchants due to a simpler chemical composition.

§ B.3 Preparation

Since a three-layer heterostructure is desired for suspended structures similar to SOI. A silicon wafer is first cleaned thoroughly by piranha solution and an oxide layer is grown using plasma-enhanced chemical vapour deposition (PECVD). The PECVD deposition was not very uniform on a wafer-scale, but locally they are flat on a chip-size (5 mm × 10 mm). Using the "new oxide" recipe in PECVD, total of 2000 s was processed to deposit 3 μm of a sacrificial layer. Note that the quality of the oxide film may be different from each run, depending on the cleanliness of the deposition chamber, and requires a test for BOE etch-rate afterwards.

§ B.4 Deposition

Layer	Power (DC/RF)	Pulse : Freq.	Pressure	Gas (N_2/Ar)	Dep. time
AlN	300 W (RF)	0.5 μs : 150 kHz	2 mTorr	15 / 45 sccm	17m:15s

Table B.2: RF sputtering parameters used for AlN deposition of 270 nm. Recall that two separate identical RF power sources and targets were used to enhance the deposition rate.

AlN films are sputtered with radio frequency (RF) magnetron system (Doug) at Nanofab. A standard DC power source with N_2 gas will cause nitrification, or poisoning, on the Al target surface [182]. For insulator sputtering, a RF source is used and results in a slower deposition rate. Here I used two Al targets to compensate the deposition rate (14.5 nm/min) with two connected RF power sources on each target. The main challenge of AlN deposition is the presence of oxygen (O_2) inside the chamber, which results in AlON grains embedded in AlN film. A quick way to minimize this problem is to pump the chamber overnight to achieve a clean vacuum prior to deposition. A typical base temperature reached after twelve hours of cryo-pumping reads 1.1 $\times 10^{-7}$ Torr from a Bayard-Alpert ion gauge. Baking the chamber to 150°C during the pumpdown is also a solution but there is a risk of heating a nearby cryopump without proper shielding. I could also add a getter material, titanium for example, to assist in removing oxygen in the chamber. Two Al targets with 45 sccm Ar gas were used to initiate the plasma at 8 mTorr, after which 15 sccm of N_2 gas was introduced. The pressure was finally adjusted to 2 mTorr and conditioned for 3 minutes while the shutters were closed. The deposition rate of AlN for this recipe was 14.5 nm/min with the two targets. The parameters used for RF sputtering is summarized in table B.2.

Orientation	2θ (degree)	Amplitude (Counts)	FWHM (degree)
(100)	33.30	495	0.66
(002)	36.10	760	0.52
(101)	38.08	2284	0.66
(102)	49.93	528	0.76
(110)	59.48	341	0.73

Table B.3: Gaussian fit parameters from the XRD data in Fig. B.2 showing the 2θ, amplitude, and the FWHM of the AlN film.

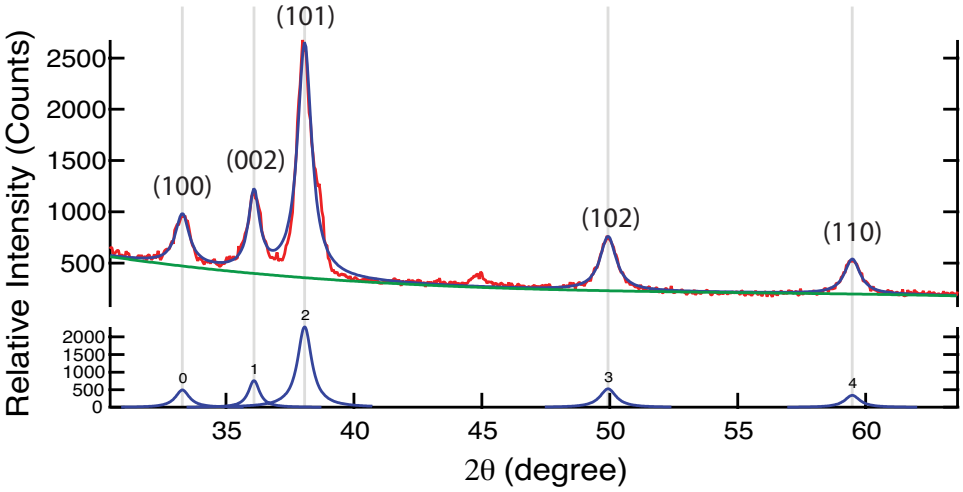

Figure B.1: **X-ray diffraction data of AlN** The XRD data, obtained from the ACSES lab, shows the overall orientation (101) of the polycrystalline AlN film on borofloat. Blue lines are the Gaussian fits where the parameters are listed in table B.3

§ B.5 Characterization

The AlN layer has been characterized in three categories: thickness, adhesion, and its crystal orientation. The tools used for measuring film thickness were alpha-step and filmmetrics dielectric thickness mapping system at the Nanofab cleanroom. Both the stylus profilometry and the reflection measurement gave consistent results of $\sim$ (270 $\pm$20 nm). The AlN film also passed an adhesion test, where the film stayed intact after sticking and unsticking a strong adhesive tape — suggesting a strong bond of AlN to a glass substrate. Lastly, the orientation of AlN was tested in the Alberta centre for surface engineering and sciences (ACSES, now part of Nanofab) using a X-ray diffraction technique. An AlN-borofloat test piece was used here to avoid contributions from the substrate. According to Fig. B.2, the overall orientation of the poly-crystalline AlN film was determined to be (101), which had the largest amplitude. Each peak was fit with Gaussian profile to obtain FWHM as seen in Fig. B.2 and tabulated in table B.3. The rather large widths indicates that inhomogeneous strain was present on the sample during the deposition possibly due to the pressure variations during the deposition.

Process	O_2 cleaning	AlN etch
Forward ICP power (W)	2000	1000
RF power (W)	100	100
DC Bias (V)	450	474
Pressure (mTorr)	7	10
Cl_2 flow rate (sccm)	—	15
BCl_3 flow rate (sccm)	—	25
O_2 flow rate (sccm)	100	—
Substrate temperature (°C)	20	50
Processing time (min:sec)	20:00	05:00

Table B.4: A table showing the RIE parameters to etch AlN film. Followed by a typical O_2 plasma clean, $\sim$ 5 minutes were processed to etch $\sim$330 nm AlN. Unfortunately, the etch mask is not resistive for the typical ZEP (etch resistivity $\sim$0.7) thickness used in my project. In the future, the etch-recipe needs to be modified, the e-beam resist needs to be thicker, or the AlN film needs to be thinner.

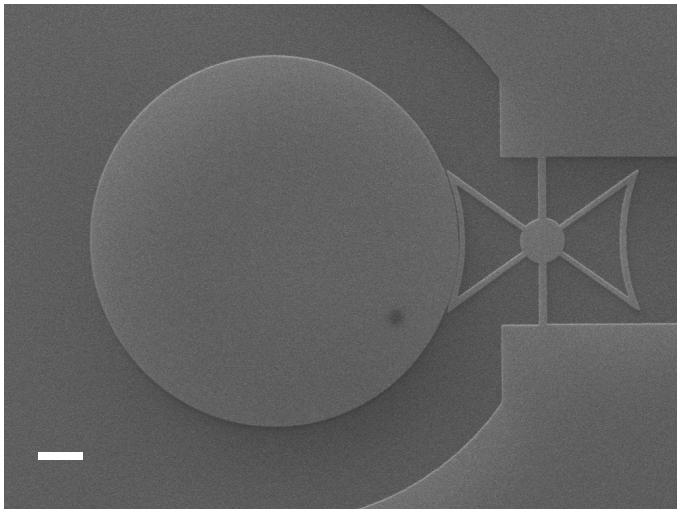

Figure B.2: **AlN optomechanical device** A SEM image showing a partially etched AlN device, where 42 seconds were processed to observe the etch profile without etching through the e-beam resist. The scale bar is 1 μm and the black dot on the microdisk is an artifact from SEM imaging.

§ B.6 Aluminium nitride etch

For microfluidic cavities, an optical lithography is typically used for AlN patterning. A commercial aluminum etchant, consisting of 80% phosphoric acid, 5% nitric acid, 5% acetic acid and 10% water, is a popular choice. An AZ400K developer were also used to etch AlN films. On the other hand, delicate optomechanical structures require a full EBL process and an anisotropic dry-etch method for patterning. The EBL method follows the same process as mentioned previously, except that Cl_2 and BCl_3 gas chemistries were used for ICP-RIE. A detailed etch recipe is shown in table. B.4, but the etch resistivity was poor for ZEP520a ($\sim$0.7). Processing for only 42 seconds, the preliminary result is shown in Fig. B.2, where more optimization is required for the recipe. A thicker resist or a thinner AlN film would also work. This path of AlN optomechanics halted since 2015.

§ B.7 Summary

In summary, I have started developing a recipe for AlN deposition, which stemmed from a project to insert piezoelectric actuators and transducers inside the microfluidic cavity. As an extension of this effort to optomechanical devices, I was able to pattern some features on a AlN-on-insulator devices. Although this project halted, it may be worth exploring for piezoelectric applications and studies.